



ScuDo
Scuola di Dottorato ~ Doctoral School
WHAT YOU ARE, TAKES YOU FAR



Doctoral Dissertation
Doctoral Program in Aerospace Engineering (32th cycle)

Optimization Approaches Under Uncertainty for Hybrid Rocket Engines

Filippo Masseni

* * * * *

Supervisors

Prof. Dario Giuseppe Pastrone, Supervisor
Prof. Lorenzo Casalino, Co-supervisor

Politecnico di Torino

This thesis is licensed under a Creative Commons License, Attribution - Noncommercial-NoDerivative Works 4.0 International: see www.creativecommons.org. The text may be reproduced for non-commercial purposes, provided that credit is given to the original author.

I hereby declare that, the contents and organisation of this dissertation constitute my own original work and does not compromise in any way the rights of third parties, including those relating to the security of personal data.

Filippo Masseni

Abstract

Hybrid rocket engines are a promising propulsion system, albeit being not as well developed as other chemical rocket systems at the date. Wide thrust range and fine control features (including shut-down and re-ignition capabilities) make the hybrids suitable for many applications, including small launchers, space propulsion systems and upper stages, which have been considered in the present work as test case.

Hybrid rocket engines are safer than solid rocket motors and cheaper than liquid rocket engines, having, at the same time, a low environmental impact. In general, a hybrid powered stage can easily be employed in place of conventional solutions, granting larger payload mass and lower overall cost. On the other hand, the actual use of hybrid propulsion systems is still limited by a number of issues, including low regression rates, combustion instability and intrinsic uncertainty in the hybrid combustion process.

The author developed a robust-based optimization procedure, which consists of a sensitivity analysis method, used to identify the most relevant source of uncertainty in the numerical model, and several design of experiments techniques, employed to evaluate system performance in the presence of uncertainty and grant robustness in the design. The optimization of a hybrid powered upper stage, suitable as a replacement for the actual Vega launcher upper stages, was considered as a test case. Different feed systems were also taken into account and compared.

Results showed that robustness in the design is achievable, despite the presence of uncertainty, when the proposed procedure is employed for the optimization of the hybrid rocket engine, also granting a relevant payload gain with respect to the current launcher configuration.

Abstract

Gli endoreattori a propellenti ibridi costituiscono un sistema propulsivo promettente, pur non essendo, ad oggi, stati sviluppati al pari degli altri sistemi di propulsione chimici a razzo. L'ampia gamma di spinta e le precise possibilità di controllo (incluse le capacità di spegnimento e di riaccensione) rendono gli ibridi adatti per molte applicazioni, tra cui piccoli lanciatori, sistemi di propulsione spaziali e stadi superiori, i quali sono stati considerati nel presente lavoro come caso di studio.

Gli endoreattori a propellenti ibridi sono più sicuri degli endoreattori a propellenti solidi e più economici degli endoreattori a propellenti liquidi, avendo, allo stesso tempo, un basso impatto ambientale. In generale, uno stadio ibrido può facilmente essere utilizzato al posto delle soluzioni convenzionali, garantendo un carico utile maggiore e un minor costo complessivo. D'altra parte, l'utilizzo pratico dei sistemi di propulsione ibridi è tutt'ora limitato da numerose questioni irrisolte, tra cui il basso rateo di regressione, l'instabilità della combustione e le incertezze intrinseche nel processo di combustione ibrido.

L'autore ha sviluppato una procedura di ottimizzazione robusta costituita da un metodo per l'analisi di sensitività, usato per identificare le principali fonti di incertezza presenti nel modello numerico, e svariate tecniche di design degli esperimenti, impiegate per valutare le prestazioni del sistema in presenza di incertezza e garantire la robustezza nel design. Come caso di studio è stata presa in considerazione l'ottimizzazione di uno stadio superiore ibrido, adatto a sostituire gli stadi superiori dell'attuale lanciatore Vega. Diversi sistemi di alimentazione sono stati valutati e messi a confronto.

I risultati ottenuti dimostrano che la robustezza nel design può essere ottenuta, nonostante la presenza di incertezza, utilizzando la procedura proposta per l'ottimizzazione del motore ibrido a razzo, garantendo altresì un consistente guadagno in termini di carico utile rispetto all'attuale configurazione del lanciatore.

Acknowledgements

Computational resources were provided by HPC@POLITO, a project of Academic Computing within the Department of Control and Computer Engineering at the Politecnico di Torino (<http://www.hpc.polito.it>).

Contents

List of Tables	VI
List of Figures	VIII
1 Introduction	1
1.1 Research Topic and Scope	1
1.2 Thesis Structure	2
2 Hybrid Rocket Engine Development: an Open Topic	5
2.1 Introduction	5
2.2 Historical Background	6
2.3 Fundamentals	9
2.4 Potential Applications	15
2.5 The Need for Robustness	17
3 Uncertainty and Robust Design	21
3.1 Introduction	21
3.2 Classification and Management	23
3.3 Quality and Robustness	24
3.4 Robust Design Method	28
3.5 Conclusions	32
4 Robust-based Optimization	35
4.1 Sensitivity analysis and screening	35
4.2 Design of Experiments	40
4.3 Optimization	45
5 Real World Application: Hybrid Powered Upper Stage	51
5.1 Case Study	51
5.2 Hybrid Rocket Engine Model	53
5.3 Ascent Trajectory	59
5.4 Robust-based Optimization	61
5.4.1 Sensitivity Analysis and Parameters Screening	61

5.4.2	Design of Experiments	65
5.5	Numerical Results	68
5.6	Conclusions	76
6	Real World Application: Electrical Turbo Pump Upper Stage	81
6.1	Mathematical Model	82
6.1.1	Feed System	82
6.1.2	Mass Budget and Ascent Trajectory	84
6.2	Robust-based Optimization	86
6.3	Numerical Results	87
6.4	Conclusions	91
7	Conclusions	95
	Nomenclature	99

List of Tables

2.1	Direct HRE propellants combination and performance ($p_c = 34.5$ bar, $p_e = 10.1$ bar).	10
2.2	Values of the regression rate coefficient a and exponent n consistent with \dot{y} in m/s and G_O in kg/(m ² s).	14
3.1	L_8 orthogonal array.	30
3.2	L_9 orthogonal array.	30
3.3	L_{18} orthogonal array.	31
4.1	$E_j^{(i)}$, μ_j^* and σ_j for the numerical example.	38
4.2	Box-Behnken design for $k = 6$.	43
4.3	Taguchi's designs.	44
5.1	Z9 and AVUM main features.	53
5.2	Boundaries of the elements of \mathbf{b} .	62
5.3	Nominal and off nominal values of the elements of \mathbf{X} .	62
5.4	SA settings and computational cost.	63
5.5	Sensitivity analysis outputs: μ_j^* and σ_j .	64
5.6	F_{12} array.	68
5.7	Taguchi's L_{18} array.	68
5.8	Box-Behnken's array.	69
5.9	PSO settings.	70
5.10	Computational cost comparison.	70
5.11	DET, F_{12} , L_{18} and B_{48} results.	71
5.12	Mass budget comparison (in nominal conditions).	71
5.13	Mass budget comparison: normalized ratios (in nominal conditions).	71
5.14	Results of the cross evaluation of the optimal solutions.	73
5.15	Scattering of F_{12} robust solution.	75
5.16	Scattering of L_{18} robust solution.	75
5.17	Scattering of B_{48} robust solution.	75
6.1	Electric properties.	85
6.2	Boundaries of the elements of \mathbf{b} .	86
6.3	L_9 orthogonal array.	86
6.4	Robust optimal design parameters.	87
6.5	Robust optimal design performance.	88

6.6	Mass budget comparison: payload, propellants and total engine dry masses.	88
6.7	Mass budget comparison: engine components and electrical systems masses.	88
6.8	Mass budget comparison: normalized ratios.	89
7.1	General mass budget comparison for robust solutions. VLV stands for the current Vega launcher performance.	96

List of Figures

2.1	HREs timeline.	7
2.2	SpaceShipOne vehicle landing after its first flight into space	8
2.3	Peregrin static test. Credits: NASA Ames Research Center.	9
2.4	Direct HRE schematic and combustion process.	11
2.5	Regression rate regions.	12
2.6	Droplets entrainment mechanism.	14
2.7	HREs pros and cons.	15
3.1	Uncertainty-based design domains.	21
3.2	Robustness vs. reliability	22
3.3	Parameter uncertainties management approaches: interval bounds, membership functions and PDFs	23
3.4	Classical concept of quality: the step function. $m \pm \Delta_0$ are engineering specifications, m is the target performance, $L(y)$ is the quality loss function and A_0 is the cost linked to system failure.	24
3.5	Quadratic loss function.	25
3.6	Quadratic loss function comparison.	26
3.7	Quality loss distribution with $\mu \neq m$ and $\sigma^2 \neq 0$	27
3.8	Block diagram of a system or a product/process.	28
3.9	Graphical representation of the ANOM (2 levels and 8 control factors have been considered).	32
4.1	SA methods classification.	36
4.2	Graphical representation of Morris indices.	37
4.3	Graphical representation of Morris indices for the numerical example.	39
4.4	Graphical representation of Morris trajectories in the input domain. Dot markers represent $F_j^{(i)}$ evaluation. Blue, red and green lines are the first, second and third trajectory, respectively. The black dot marker is the starting point $a = 3$, $b = 3$ and $c = 3$ of the trajectories. The order of OAT parameters variations and variation directions are both randomly chosen.	39
4.5	Graphical representation of a Latin square design ($k = 3$, $L = 3$, $N_{ME} = 9$): green dots are the tests to be performed and the black dot corresponds to the all-nominal condition.	41

4.6	Graphical representation of a full factorial design ($k = 3, L = 3, N_{ME} = 27$): green dots are the tests to be performed. One can notice that the point corresponding to all-nominal condition is a test point too.	41
4.7	Graphical representation of fractional factorial designs (on the left $k = 3, L = 2, p = 1, N_{ME} = 4$ and on the right $k = 3, L = 3, p = 1, N_{ME} = 9$): green dots are the tests to be performed and the black dot corresponds to the all-nominal condition. One can notice that the 3^{3-1} design is equal to Latin square design with $k = L = 3$	42
4.8	Graphical representation of a central composite design ($k = 3, L = 2, N_{ME} = 15$): green dots are the tests to be performed due to the original 2^3 full factorial design, the red dots are the $2k$ additional star points and the blue dot is the +1 additional central point corresponding to the all-nominal condition.	43
4.9	Graphical representation of a Box-Behnken design for $k = 3$ ($N_{ME} = 13$): green dots are the tests to be performed. One can notice that the prescribed tests are at the middle points of the edges of the design space with the addition of the central point corresponding to the all-nominal condition.	43
4.10	DOE technique comparison: N_{ME} vs. k	45
4.11	PSO algorithm visual explanation. At each iteration, the updated velocity of each particle is a linear combination of three components: particle current velocity (grey bold arrow), particle pull toward the position of the best solution it found out until that iteration (light blue bold arrow) and particle pull toward the position of the best solution the swarm found out (red bold arrow). The relative magnitude of these three components is a function of both the learning factor of the algorithm and of randomly generated quantities.	47
5.1	Vega Launch Vehicle and staging: P80, Z23, Z9 and AVUM.	52
5.2	Grain geometry (not to scale). The injection of the oxidizer is axial, causing the majority of the combustion to occur inside the grain port. Grain lateral ends are affected by the combustion too, albeit having a far smaller regression rate.	54
5.3	Mass budget scheme. Arrows represent the functional relationships between design parameters (green boxes) and masses. m_i and $m_{fairing}$ are assigned (see Sec.5.3). The scheme is approximately scaled to the mass budget of robust solutions presented in Sec.5.5.	59
5.4	Mixture ratio α vs. time.	72
5.5	Specific impulse I_{SP} vs. time.	72
5.6	Longitudinal acceleration vs. time: first burn.	72
5.7	Longitudinal acceleration vs. time: second burn.	72
5.8	Thrust F vs. time.	73

5.9	Fuel grain regression rate \dot{y} vs. time.	73
5.10	Scheme of the employed robust-based optimization procedure. Green boxes are the input of the optimization problem, light blue boxes contain SA outputs, orange boxes present the main sub-models and tools used and the blue box reports optimization outputs. The dotted link on the right represents the feedback due to PSO algorithm which adjusts the design parameters aiming at the maximization of the merit function.	76
6.1	Pump discharge pressure p_d vs. time.	89
6.2	Oxidizer mass flow \dot{m}_O vs. time.	89
6.3	Mixture ratio α vs. time.	90
6.4	Specific impulse I_{SP} vs. time.	90
6.5	Thrust F vs. time.	90
6.6	Fuel grain regression rate \dot{y} vs. time.	90
6.7	Longitudinal acceleration vs. time: first burn.	91
6.8	Longitudinal acceleration vs. time: second burn.	91
6.9	Scheme of the employed robust-based optimization procedure. Green boxes are the input of the optimization problem, orange boxes present the main sub-models and tools used and the blue box reports optimization outputs. The dotted link on the right represents the feedback due to PSO algorithm which adjusts the design parameters aiming at the maximization of the merit function. A backward link connects mass budget and trajectory optimization boxes, underlining that the actual battery mass, and thus the payload mass, have to be verified "a posteriori".	92

Chapter 1

Introduction

1.1 Research Topic and Scope

Hybrid rocket engines are chemical rockets which employ propellants stored in different physical states, usually a liquid oxidizer and a solid fuel. They have many appealing features, such as high performance, fine thrust control, high safety and low environmental impact. In hybrid rocket engines only the flow of the liquid propellant can be controlled, coupling thrust level and mixture ratio. This peculiar control feature requires the development of a proper multidisciplinary design and optimization approach, including a mission specific and coupled optimization of both hybrid engine and vehicle trajectory.

In addition, the presence of uncertainty in the design could cause severe deviations from nominal engine performance, seriously jeopardizing mission accomplishment. A robust-based optimization approach is mandatory in order to reduce system sensitivity, granting the fulfillment of mission goals despite the presence of uncertainty. Unfortunately, robust-based optimization results to be a really demanding task, even when only few uncertain parameters are taken into account in the mathematical model. Therefore, proper tools have to be developed, firstly to identify the most critical source of uncertainty in the system and then to manage it in an effective way, granting robustness in the design at an affordable computational cost.

In this Doctoral Thesis, the author will present a novel approach to the optimization under uncertainty of hybrid rocket engines, providing to the reader theoretical fundamentals, numerical applications and their most significant results. In order to help the reader, the following Section will summarize the core structure of the present manuscript.

1.2 Thesis Structure

This Doctoral Thesis consists of seven Chapters. In the present Chapter the author summarized the most important information about his research area and, more specifically, the core topic and scope of his manuscript. Basic concepts, such as hybrid propulsion and robust design, that could be helpful from the beginning for the reader, were here introduced too.

The second Chapter, [Hybrid Rocket Engine Development: an Open Topic](#), is dedicated to provide the required background about hybrid propulsion issues and potential to the reader. In the introduction to Chapter 2, the author will describe the working principle of hybrid rocket engines and their fascinating features. In the second Section, the most important milestones of the development of hybrid propulsion systems will be gathered in a brief historical perspective, from the first attempts in the early '30s to the current test and flight programs. A special focus will be given by the author to attained performance and design choices, in order to underline how past failures have influenced present successes. The third Section will present the most common engines configurations and propellants, dwelling on direct hybrids and paraffin-based fuels. In the fourth Section, pros and cons of hybrid propulsion will be listed, with respect to heritage ones, supporting the reader in the subsequent description of the potential applications of hybrids that can be found in the literature at the date. The fifth, and last, Section of this Chapter will highlight the need for an innovative design and optimization procedure when uncertainty is considered in hybrid propulsion systems.

The third Chapter, [Uncertainty and Robust Design](#), is divided into five Sections. In the Introduction, the basic distinction between uncertainty-based design problems will be pointed out, introducing robust-based and reliability-based approaches. In the second Section, the author will provide few important definitions concerning uncertainty, that will be used in the following of the manuscript. The third Section will introduce additional concepts developed by Dr. Taguchi in the '60s, such as quality loss and noise, which form the basis of robust-based approaches. The fourth Section will be devoted to Taguchi's Robust Design Method. Problems parameters are split into control and noise ones and robustness is defined as the insensitivity of system performance to uncertain parameters variations. Orthogonal arrays and specific quality loss functions are employed to determine the optimal design, i.e. the optimal values of control parameters. In the fifth Section the author will discuss how Taguchi's work could be applied to hybrid rocket engines problems and which design and optimization tools were required.

The fourth Chapter, [Robust-based Optimization](#), summarizes the theoretical fundamentals of the robust-based optimization approach developed in the Thesis. In the first Section, sensitivity analysis and parameters screening methods will be discussed. The author opts for the Morris Method in this work, thus a more detailed description will be given and a simple numerical example will be provided. The

second Section will be dedicated to design of the experiments techniques. Several designs will be presented and compared. In the present work, fractional factorial design, Taguchi’s design and Box-Behnken design will be employed. In the third Section, the author will report the most important features of the direct optimization method used in this work, namely a particle swarm optimization algorithm, which mimics the social behavior of flocks of birds and schools of fish looking for food.

The fifth Chapter, [Real World Application: Hybrid Powered Upper Stage](#), is devoted to present a numerical application of the robust-based procedure depicted in Chapter 4. A hybrid rocket upper stage will be considered to replace the third and fourth stages of the current Vega launcher. An hybrid powered upper stage represents an intriguing alternative to the liquid powered one that is currently under development for the new Vega-E launcher. In the first Section, the author will describe actual Vega configuration and, in particular, third and fourth stages configuration and performance. The second Section will be dedicated to a detailed description of the hybrid rocket engine mathematical model. In Chapter 5, a gas pressurized feed system will be considered in the engine design and operation. The third Section will introduce the most important features of the indirect trajectory optimization procedure employed, which is based on the optimal control theory. The fourth Section will be dedicated to the robust-based procedure. First, the results of the sensitivity analysis and parameters screening will be presented and then the selection of the proper design of experiments techniques will be discussed. The fifth Section will report the numerical results of the optimization of the hybrid rocket engine. In the end, the sixth and last Section will present the author’s conclusions for the test case considered in this Chapter.

The sixth Chapter, [Real World Application: Electrical Turbo Pump Upper Stage](#), will concern the robust-based optimization of a hybrid powered upper stage, similar to the one presented in Chapter 5, which employs an electric pump feed system in place of a gas pressurized one. In the first Section the differences in feed system operation, mass budget and ascent trajectory will be pointed out by the author. The second Section will briefly report the optimization setup and the uncertainty model employed. In the third Section, numerical results of the optimization procedure will be presented. In the fourth and last Section, the author will make his own conclusions about the use of electric feed systems in place of heritage ones.

In the end, the seventh and last Chapter of this Thesis will be devoted to the author’s overall conclusions and final thoughts about the work here presented and its possible future developments.

Chapter 2

Hybrid Rocket Engine Development: an Open Topic

2.1 Introduction

Nowadays, chemical propulsion systems could be classified into three main categories: liquid rocket engines (LREs), solid rocket motors (SRMs) and hybrid rocket engines (HREs). Liquid and solid architecture employs oxidizer and fuel in the same phase (both liquid and both solid, respectively). Hybrid engines, on the other hand, take advantage of two different phases for oxidizer and fuel. In direct HREs, the oxidizer is stored in liquid or gaseous state inside tanks whereas the fuel is located in a solid grain inside the combustion chamber. The fuel grain is typically a hollow cylinder with a single circular port, but more complex geometries are not uncommon. Combustion process in hybrid engines is really distinctive. Oxidizer injection into the port generates a boundary layer where combustion takes place, after ignition. Solid fuel is gasified by the heat transfer from the flame zone to the grain surface and, at the same time, the gasified fuel feeds the combustion. Gasified fuel blowing alters the boundary layer and blocks the heat transfer.

Combustion mechanism and propellants state allow for some benefits over other chemical rockets architectures: higher specific and density specific impulse than SRMs and LREs respectively, higher safety level due to the physical separation of propellants until ignition, higher reliability due to simpler feeding system and good throttling, shutdown and re-ignition capabilities. Moreover, HREs are environmentally friendlier than SRMs and LREs employing semi-cryogenic or storable propellants, being at the same time cheaper, which are features gaining more and more importance in the last decades. On the other hand, HREs have some drawbacks too: lower specific and density specific impulse than cryogenic LREs and SRMs respectively, low fuel regression rate, mixture ratio shifting, mixing inefficiencies and slower response to throttling than typical LREs.

Nevertheless, the positive aspects of HREs actual use are really promising and

thus a great number of research programs are focusing on hybrid development worldwide.

2.2 Historical Background

The time-line of HREs development starts in the '30s, when Korolev and Tikhonravov's GIRD-09 reached an altitude of 1500 m on 17 August 1933. The engine burned for 15 s, producing a thrust of 500 N employing gelled gasoline and LOX as propellants. In 1937 Andrussov, Lutz and Noeggerath tested a bigger engine in Germany, capable of 10 kN of thrust, using coal as fuel and gaseous nitrous oxide as oxidizer. Their attempt failed, highlighting, despite themselves, that carbon was not able to grant the necessary burning rate. Shortly after, between 1938 and 1939, Oberth developed a Liquid OXYgen (LOX)/Graphite hybrid engine, sadly coming to conclusions similar to Andrussov, Lutz and Noeggerath ones. Later, since 1947, the Pacific Rocket Society built a bunch of experimental hybrids, called XDF-#, employing LOX and wood-based (Douglas fir) fuels.[15] First tests resulted in nozzles melted and test bench destroyed. Finally, in 1951, the XDF-23 successfully managed to reach an altitude of 30000 ft thanks to an aluminum alloy nozzle and a LOX/rubber-based fuel propellants combination. Burning tests suggested that chamber pressure was proportional to oxidizer mass flow in hybrids, instead to flame surface as in solid motors, avoiding explosions risk due to fuel grain degradation.[2]

Between '40s and the early '60s exotic configurations were investigated, such as solid-fuel air-breathing ramjet at the Jet Propulsion Laboratory and reverse hybrid rocket (solid oxidizer and liquid fuel) at the John Hopkins University, but without success due to poor performance and burning difficulties. On the other hand, General Electric company (GE) successfully developed an hypergolic hybrid engine, employing Hydrogen Peroxide and Polyethylene, improving the performance of the original peroxide mono propellant system.[22] In the mid-'60s NASA promoted many research programs aiming at the development of high-energy space engines. In the context of HRE, Lithium was blended with Hydroxyl-Terminated PolyButadiene (HTPB) to burn with a mixture of Fluorine and Oxygen, called FLOX. This propellant combination took advantage of the extremely energetic reactions between Hydrogen and Lithium with Fluorine, alongside the conventional Carbon and Oxygen one. The system showed nice throttling and cold restart capabilities, granting at the same time high performance (specific impulse ≈ 380 s).[3] A different engine concept, called tri-brid, was also developed. A classical bi-propellant engine (e.g. oxygen/hydrogen) employed Beryllium as energetic additive, attaining the extremely high specific impulse (450 – 530 s) and burning temperature (≈ 5000 K). This concept was later abandoned due to Beryllium toxicity.

In parallel, the United States Air Force (USAF) supported drones flight programs, aiming at the building of high altitude/high velocity target drones. First the

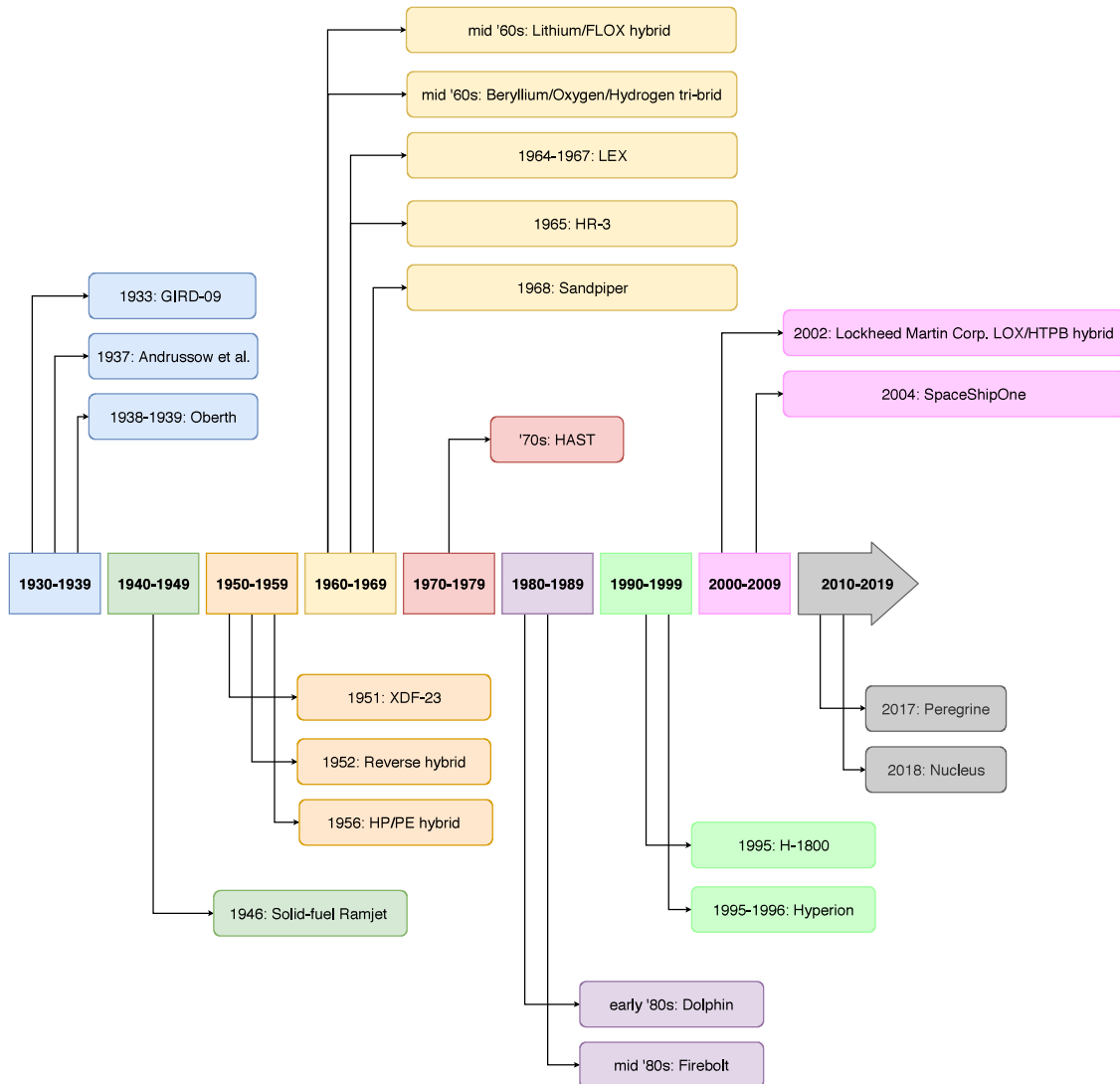


Figure 2.1: HREs timeline.

Sandpiper was developed, employing nitrogen oxides mixture (1/4 of Nitric Oxide and 3/4 of Nitrogen Tetroxide) and PolyMethylMethacrylate (PMMA)/Magnesium as propellants. In 1968, the Sandpiper exhibited high throttle-ability and Mach 4 speed at 100000 ft of altitude, during a flight of more than 5 minutes. Later, in the context of the High Altitude Super-sonic Target (HAST) program, bigger hybrids were built using slightly different propellants combination, increasing throttling capability. It is noteworthy that, unlike the Sandpiper, HAST was recoverable. HAST was further improved giving origin, in the mid '80s, to the Firebolt.

At the same time, in Europe, research programs focused on hypergolic propellants, based on liquid nitric acid and solid amine fuels. French Lithergol EXperimental (LEX) series between 1964 and 1967 performed eight successful launches, achieving an altitude greater than 100 km, breaking all existing records at that time. In 1965, the Swedes of Volvo Flygmotor carried out two successful flight tests of the HR-3 hybrid vehicle, using Tagaform (PolyButadiene (PB) with an aromatic amine) as fuel. Later in the '70s, larger scale systems were planned employing an improved fuel called Sagaform A, but scheduled flight tests never took place.

In the early '80s the Starstruck company built and launched an hybrid sounding rocket called Dolphin, capable of more than 11 kN of thrust. Later, between 1985 and 1995, the AMERICAN ROcket Company (AMROC) further developed Starstruck project creating the H-1800 engine. LOX/HTPB were used as propellants, achieving more than 100 kN of thrust.

Between 1996 and 1997, four launches of the Hyperion Sounding Rocket took place in the United States. For the first time self pressurized Nitrous Oxide was used, alongside with HTPB as fuel. A vacuum specific impulse of 205 s and an altitude greater than 30 km were achieved.[2] Later, in 2002, the Lockheed Martin Corporation built the greatest sounding rocket to date, employing LOX and HTPB. The attained altitude exceeded 70 km and the rocket had an initial thrust of 267 kN.



Figure 2.2: SpaceShipOne vehicle landing after its first flight into space

In 1996, the New Spirit of St. Louis organization announced the X Prize contest: safely transport three people to 100 km and back, twice within two weeks. Between 1996 and 2004 the prize grew reaching \$10 millions and involving teams from all over the world. In 2004, Burt Rutan and Paul Allen's hybrid-powered SpaceShipOne vehicle achieved 112 km, winning the contest. Nitrous oxide and HTPB were used as propellants in the hybrid rocket engine, generating 88 kN of thrust.

Between 2010 and 2018, in the context of the ESA’s Future Launchers Preparatory Programme, the hybrid powered Nucleus launcher was developed. In 2018 the launcher reached 115 km of altitude, successfully deploying six small payloads in its first flight test. HP/HTPB were used by Nucleus as propellants, achieving 40 kN of vacuum thrust. Future developments focus on increasing thrust level up to 75 – 100 kN by means of clustered hybrid engines and improved turbo pump feeding systems.



Figure 2.3: Peregrine static test. Credits: NASA Ames Research Center.

In the early 2000s Stanford researchers discovered a new class of paraffin-based fuel able to burn faster than conventional fuels. Experimental tests started from lab-scale hybrid rocket engine and culminated in 2017 with the full scale Peregrine hybrid rocket engine static test. Peregrine rocket was the result of a joint effort of NASA’s Ames Research Center, Stanford University, Space Propulsion Group and NASA’s Jet Propulsion Laboratory.

2.3 Fundamentals

As mentioned before, in HRE oxidizer and fuel are physically separated and stored in different phases. However, this condition is achievable in several, and sometimes weird, ways. The best-researched hybrid engine configuration, called classical or direct HRE, employs solid fuel and liquid oxidizer.

Direct HRE popularity is mainly due to the wide choice of solid fuels, such as hydrocarbons and metals, and liquid oxidizers, such as Oxygen, FLOX, HP and various Nitrogen compounds. Table 2.1 reports a non-exhaustive list of direct HRE

Table 2.1: Direct HRE propellants combination and performance ($p_c = 34.5$ bar, $p_e = 10.1$ bar).

Oxidizer	Fuel	α_{opt}	I_{SP}	c^*
-	-	-	s	m/s
FLOX	Li/LiH/HTPB	2.8	326	2118
FLOX	HTPB	3.3	314	2042
FLOX	HTPB/Al(60%)	2.5	312	2006
LOX	NH3(s)/Be(26%)	0.47	307	1967
LOX	CH4(s)/Be(36%)	1.3	306	1918
LOX	CH4(s)	3	291	1871
LOX	Paraffin	2.5	281	1804
LOX	HTPB	1.9	280	1820
LOX	PE	2.5	279	1791
LOX	Pentane(s)	2.7	279	1789
LOX	HTPB/Al(40%)	1.1	274	1757
N2O4	HTPB/Al(40%)	1.7	261	1679
LOX	PMMA	1.5	259	1661
N2O4	Paraffin	4	259	1667
N2O4	HTPB	3.5	258	1663
N2O	HTPB/Al(40%)	3.5	252	1637
LOX	Carbon	1.9	249	1599
N2O	Paraffin	8	248	1606
N2O	HTPB	7.1	247	1604
RFNA	HTPB	4.3	247	1591
N2O	PE	8	247	1600
GOX	Cellulose(C6H10O5)	1	247	1572
N2O	Carbon	6.3	236	1522
Air	Carbon	11.3	184	1224

propellants, sorted from the highest specific impulse I_{SP} to the lowest one; α_{opt} indicates the oxidizer-to-fuel mixture ratio required for the maximum I_{SP} and c^* the characteristic velocity.[2]

An alternative configuration is the reverse hybrid, mostly developed in the ‘50s, which uses liquid fuel and solid oxidizer. Solid oxidizers are really hard to manufacture because inert fillers or small quantities of fuels are required in the process. The former reduce propellants performance, whereas the latter make the mixture hazardous. A third configuration is the so called “tri-brid” that employs a bi-propellant combustion core, e.g. Oxygen/Hydrogen, with the addition of a third component, such as Aluminum or Beryllium compounds. The tri-brid exhibits extremely high specific impulse and combustion temperature. The last configurations

are the solid-fuel ramjet and the ducted rocket. The first uses ram air as oxidizer and a solid fuel, avoiding the feeding system required by more conventional liquid-fuel ramjet. The latter, on the other hand, burns the exhausted gases, produced by the combustion of a fuel rich solid grain, with ram air to obtain stoichiometric condition and optimal performance. Reverse hybrid, tri-brid, solid-fuel ramjet and ducted rocket will not be detailed in this Section.

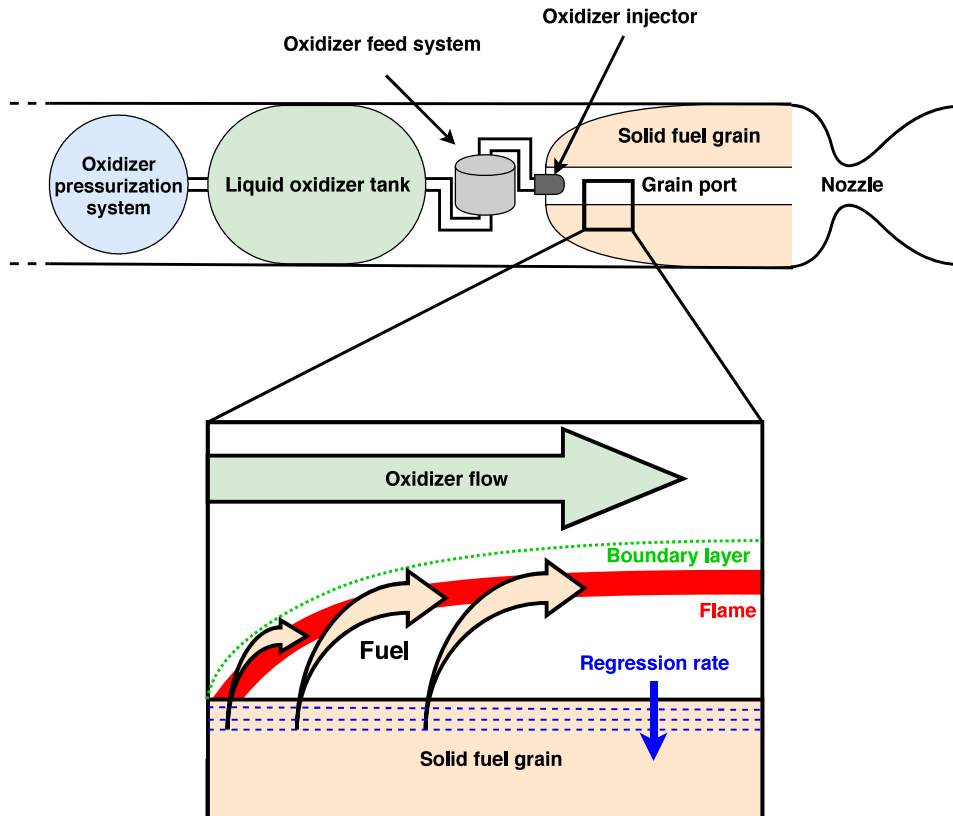


Figure 2.4: Direct HRE schematic and combustion process.

A simple schematic of a direct HRE is presented in Fig. 2.4. Typically, the solid fuel grain is cylindrical and the oxidizer is injected longitudinally from the engine head end into a single circular port. Due to such geometry, the combustion process is quite peculiar in direct HRE: oxidizer flow generates a boundary layer, where, after engine ignition, a diffusion flame takes place. The heat due to combustion gasifies the fuel, which in turn feeds the flame blowing from the surface. The blowing modifies the boundary layer, blocking the heat transferred to the solid fuel surface in a feed-back mechanism. Fuel regression rate \dot{y} determines the amount of gasified fuel that reaches the flame zone and its typical behavior is reported in Fig. 2.5 as a function of the total mass flux G that flows through the grain port. One can distinguish three different regions:[19, 20, 21]

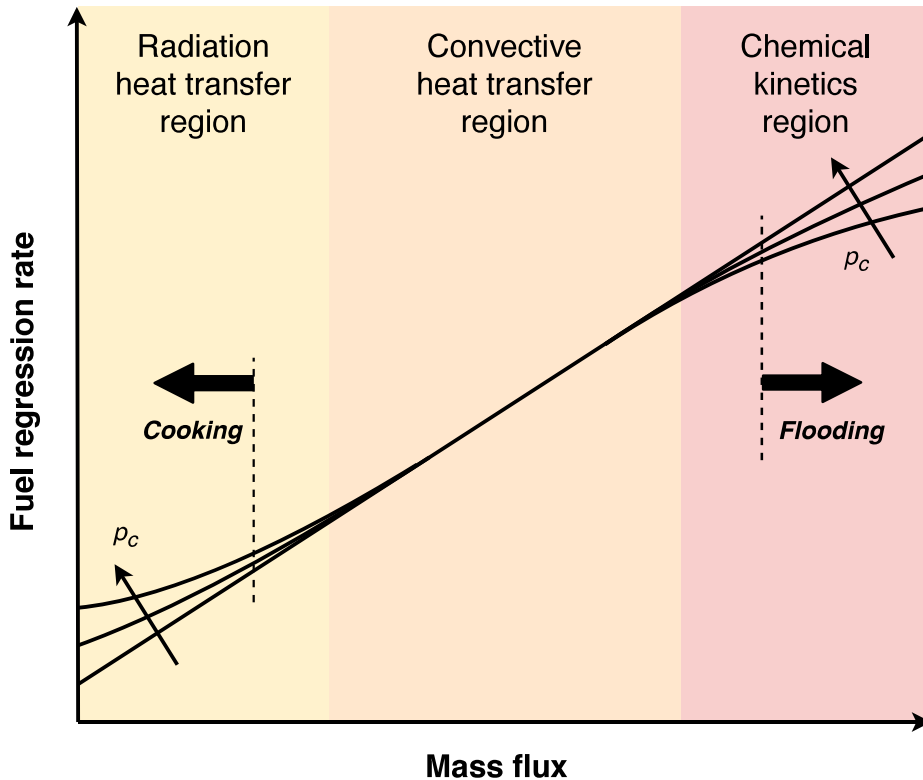


Figure 2.5: Regression rate regions.

1. Radiation heat transfer region (in yellow in Fig. 2.5), in which the convective heat transfer is reduced due to the low values of mass flux G and, on the other hand, radiation heat transfer from gases increases. The resulting regression rate \dot{y} depends on the partial pressure of the emitting compounds and on port diameter. In this region, a lower limit of the mass flux exists. As G decreases, the fuel residence time in the thermal layer increases and the solid fuel may be cooked or melt underneath its surface before being gasified. This operative condition may occur at the end of an HRE burn, when a gas pressurized feed system is used;
2. Convective heat transfer region (in orange in Fig. 2.5), in which diffusion phenomena dominate and the regression rate \dot{y} depends only on the magnitude of the mass flux G . Regression rate behavior in this region will be detailed in the following paragraphs;
3. Chemical kinetics region (in red in in Fig. 2.5), in which the combustion process is mainly controlled by chemical kinetics, whereas diffusion plays a minor role, resulting in a pressure dependent regression rate \dot{y} . [23] In this region, an upper limit of the mass flux, called the flooding limit, exists. As

G grows, the flame may be extinguished due to too small Damköhler numbers (i.e. the ratio between reaction and transport phenomena rates) and/or too fuel-lean conditions.

In the mid-'60s Marxman et al. developed the present theory about regression rate modeling. A heat flux balance is applied to a portion of the surface of the fuel grain as presented in Eq.(2.1), where q is the total heat flux entering into the fuel grain, ρ_F indicates the fuel density and $\Delta H_{v,eff}$ is the amount of thermal energy required to change the solid fuel into gas per unit mass.

$$q = \dot{y}\rho_F\Delta H_{v,eff} \quad (2.1)$$

Heat transfer is mainly convective, i.e. depends on the local mass flux G . Assuming a turbulent layer and negligible radiation, they suggested the semi-empirical relation[1] for the regression rate given in Eq.(2.2), where B is the ratio between main stream thermal energy, relative to the grain surface, ΔH_{fw} and $\Delta H_{v,eff}$ and x is the position along the grain longitudinal axis.

$$\dot{y}\rho_F \propto B^{0.32}G^{0.8}x^{-0.2}, \quad 0 < B < 100 \quad (2.2)$$

One can notice that the effect of boundary layer growth on heat transfer is taken into account by the small negative exponent of x in Eq.(2.2), resulting in slightly decreasing regression rate as x grows. On the other hand, total mass flux G increases with x because of the addition of gasified fuel. Hence, an axial position of minimum regression rate exists, but usually differences are sufficiently small that regression rate can be assumed constant along grain axis.

$$\dot{y} = aG_O^n = a\left(\frac{\dot{m}_O}{A_p}\right)^n \quad (2.3)$$

Therefore, oxidizer mass flow G_O is widely used in regression rate semi-empirical correlation, in place of the total mass flux G , as presented in Eq.(2.3), where \dot{m}_O is the oxidizer mass flow rate through grain port area A_p . Coefficient a and exponent n are obtained by experimental data and strongly depends on G_O value, propellants combination, engine dimensions, grain, injectors and flow features. The relation reported by Eq.(2.3) fits well regression rate behavior in the intermediate range of G_O , when turbulent heat transfer is dominant. Table 2.2 summarizes reference values of a and n for the most used HRE propellants.[6]

In the early 2000's, a new class of high regression rate fuels were studied by Karabeyoglu et al. at Stanford University. [17] These fuels are able to produce a really thin liquid layer on the surface of the solid fuel during engine burn.

Liquid layer instability, due to the oxidizer flow along the grain port, causes the entrainment of droplets into the gas stream from fuel surface (see Fig. 2.6). The entrainment mechanism is able to increase by far fuel mass transfer rate into the

Table 2.2: Values of the regression rate coefficient a and exponent n consistent with \dot{y} in m/s and G_O in kg/(m²s).

Oxidizer	Fuel	a m ²ⁿ⁺¹ s ⁿ⁻¹ kg ⁻ⁿ	n
-	-	-	-
HP	PE	$7.00 \cdot 10^{-6}$	0.800
HP(90%)	HTPB	$2.47 \cdot 10^{-5}$	0.666
LOX	HTPB	$9.29 \cdot 10^{-6}$	0.852
LOX	Wax	$9.10 \cdot 10^{-5}$	0.690

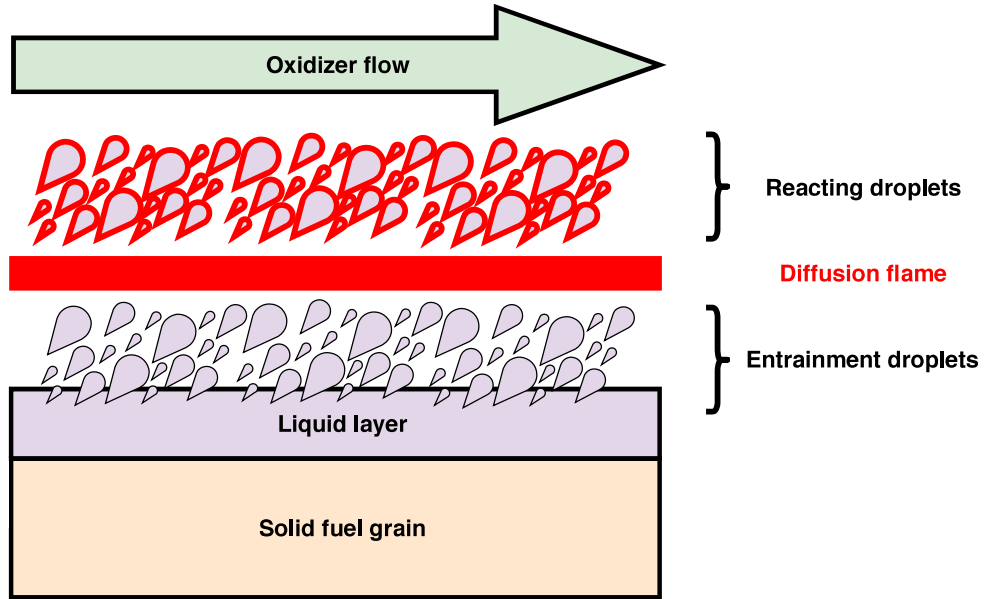


Figure 2.6: Droplets entrainment mechanism.

flame zone. Moreover, droplets are not subject to the heat transfer blocking effect due to the gas blowing from fuel surface, as previously described for conventional fuels, granting much higher (from 3 to 4 times) overall fuel regression rate, i.e. better HRE performance.

The mass transfer due to entrainment results to depend inversely on the liquid layer viscosity and surface tension. Normal-alkane hydrocarbons, with carbon numbers higher than 14, are suitable fuels, being in solid state in standard condition and exhibiting the required characteristics at the condition typical of HRE operation. Examples of these fuels are the paraffin and polyethylene waxes, whose typical values of regression rate coefficient and exponent are reported in the last row of Tab. 2.2.

The unique combustion process and architecture of HREs lead to a bunch of intriguing characteristics, both positive and negative. In Fig. 2.7 main pros and

cons of HREs use are presented. In the subsequent Sec. 2.4, potential HREs applications will be discussed.

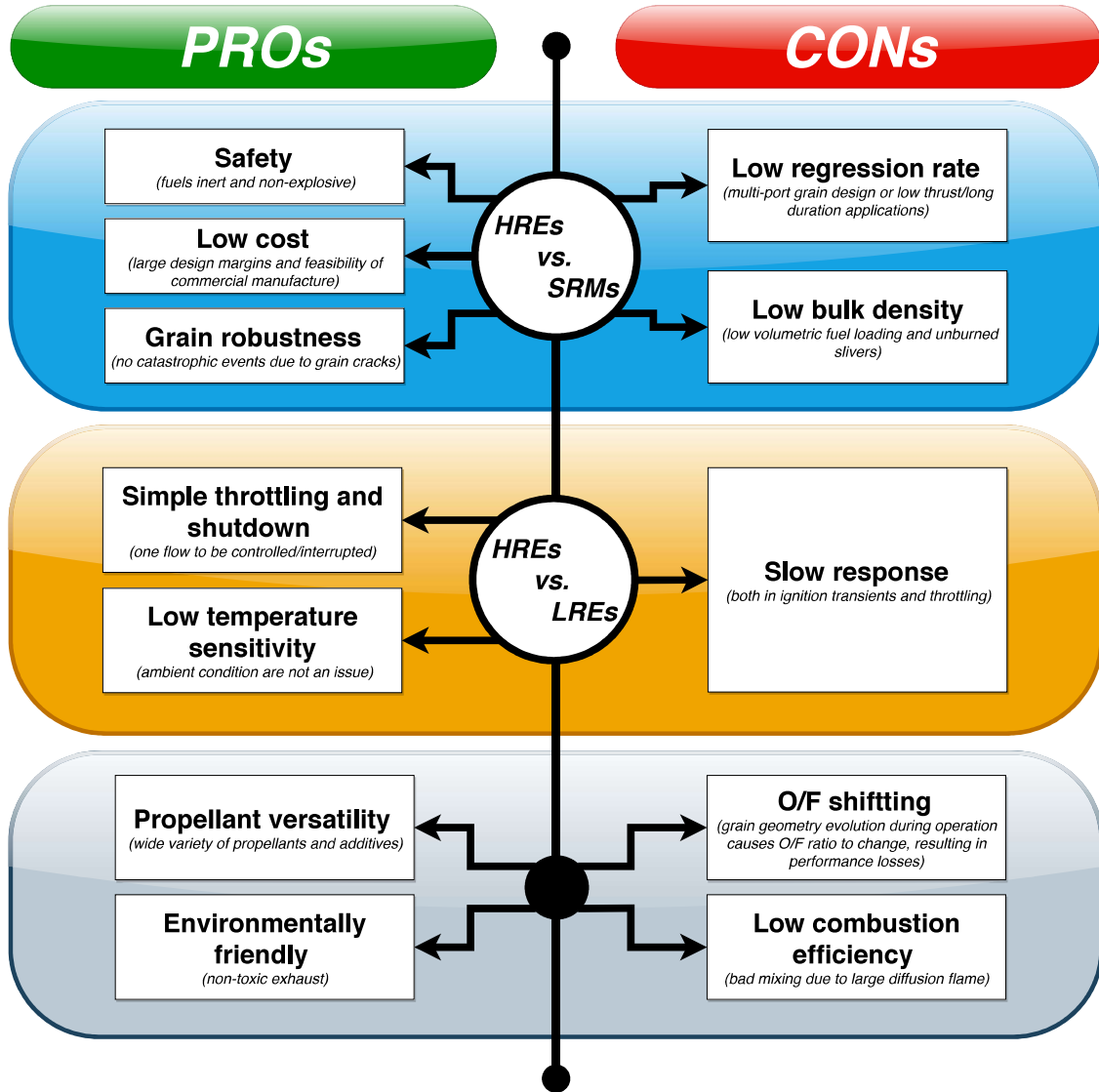


Figure 2.7: HREs pros and cons.

2.4 Potential Applications

HREs are suitable for every application in which conventional chemical rockets are actually employed. However, the hybrid architecture is superior in certain application, due to propellant versatility, performance range and thrust flexibility (throttling and shutdown).

The most extensive uses of hybrids are definitely the sounding rockets, due to their low cost, safety of engine manufacturing, transport and operation and the wide choice of propellants combinations. One possible application of a sounding rocket is the building of a micro-gravity platform. In [12] a coupled optimization of mission and engine has been carried out. A simple gas-pressurized feed system has been used and the performance of several propellants have been evaluated: HP/PE showed better performance than LOX/HTPB, whereas nitrous oxide/HTPB remained competitive due to simplicity and low cost. Accelerators for hyper-sonic testing are other possible applications of an hybrid powered sounding rocket. In [14] single stage and two stages rockets performance have been compared. Results showed that hybrids are a suitable propulsion system for hyper-sonic testing and single stage rockets are preferable, unless the payload fraction is really small and/or large final velocity is required.

HREs are capable of both high thrust levels, mandatory for velocity increments in space, and throttling/shutting-down/restarting, required to perform coast arcs, multiple burns missions and precise orbit insertion. These features makes HREs an attractive solution for space engines and launcher upper stages. This kind of application has been deeply analyzed at the Politecnico di Torino since 2005.[10, 11, 13, 6, 24, 5, 4, 8]. Different feeding systems, such as blowdown, partially regulated and electrically driven turbopump, and propellants, e.g. HP/PE, LOX/HTPB, LOX/Wax and N₂O/Wax, have been considered. Deterministic and robust-based design and optimization have been carried out. Results showed that target missions can be fulfilled at the cost of small payload reduction, due to the presence of uncertainties in the design, still granting nice performance improvement with respect to conventional engines.

Low cost, safety and simplicity make the hybrids an ideal propulsion system in the context of small satellites and CubeSats, whose research interests and business opportunities are in constant growth since early 2000's. A stand-alone interplanetary mission has been considered and hybrids resulted able to outperform liquid mono-propellant propulsion systems, in terms of delivered payload.[16] On the other hand, the current offer of launchers does not meet the demand for this kind of low weight payload missions. Hybrids are, one more time, definitely suitable in these applications because they are cheap, safe and eco-friendly while still providing high performance and thrust flexibility. Deterministic and subsequently robust optimization of an hybrid powered launcher has been performed at the Politecnico di Torino.[7, 4] Clusters of the same hybrid engine have been employed in each of the three stages of the launcher aiming at cost minimization alongside a simple gas pressurized feeding system. LOX/Wax have been used as propellants and an airborne launch has been considered. Results showed that optimal designs can grant both satisfactory performance and mission robustness.

Low temperature sensitivity, high specific impulse and re-ignition capability are fascinating hybrids features for a potential Mars Ascent Vehicle (MAV) as part of

a Mars sample return mission. Viable designs of hybrid MAVs have been presented in [6] and [18]. HREs resulted to outperform conventional propulsion systems in the context of a Mars mission, albeit lower in technology readiness level.

2.5 The Need for Robustness

In the previous Sections, the author described the numerous appealing features of hybrid propulsion systems and the wide variety of their potential applications. However, the actual use of hybrid technology is still limited to date, with respect to heritage chemical rockets architectures. In HREs, performance and mission are linked inextricably one another, due to their unique combustion process resulting in mixture ratio shifting and thrust variation during engine burn. Conceptual design, essential for a successful and affordable development of hybrids, has to be a multidisciplinary process, in which uncertainties in design parameters and operating conditions are taken into account to predict and manage the subsequent variability in the attained performance.

Concerning HREs, it is well known that uncertainty in the regression rate evaluation are extremely critical due to their strong effect on burning process. In [9] optimal designs for a hybrid powered upper stage have been selected by means of a 2-layer procedure involving indirect trajectory optimization and direct engine optimization. Several pairs of values for regression rate correlation coefficient a and exponent n have been used in the optimization procedure, obtaining slightly different optimized engine configurations. Then, off-design performance of these optimized designs have been evaluated varying regression rate parameters, in order to quantify the deviation from nominal performance. Optimized design for nominal regression rate parameters showed really poor off-design performance, making the mission unfeasible when regression rate was greater than the values employed for the design. On the other hand, optimized design for regression rate greater than nominal resulted in better off-design performance, albeit attained off-design altitude variation remained significant.

These results have been obtained by means of a preliminary and not rigorous approach to uncertainty. In [24] the topic of the design approaches under uncertainty for HREs has been further developed: uncertainty has been taken into account inside the optimization procedure, instead of being checked "a posteriori" as done before. Optimized design, this time, proved to grant the achievement of mission goals, despite the uncertainty in the regression rate behavior. These concepts go under the name of "robust design". However, even this robust-based approach is based on "a priori" assumptions on the sources of uncertainty, e.g. only in the regression rate value.

In this thesis, the main focus is the overcoming of these limitations and the development of an even more rigorous approach to robust-based design for HREs.

Thus, the author will provide a summary of the basic concept of uncertainty and robust design in the subsequent Chapter 3.

References

- [1] D Altman and R Humble. “Hybrid rocket propulsion systems”. In: *Space propulsion analysis and design* (1995), pp. 365–370.
- [2] David Altman and Allen Holzman. “Overview and history of hybrid rocket propulsion”. In: *Progress in Astronautics and Aeronautics* 218 (2007), p. 1.
- [3] William H Avery. *Fluid-solid propulsion unit and method of producing gaseous propellant*. US Patent 3,136,119. 1964.
- [4] L Casalino, F Masseni, and D Pastrone. “Robust Design Approaches for Hybrid Rocket Upper Stage”. In: *Journal of Aerospace Engineering* 32.6 (2019), p. 04019087.
- [5] L Casalino, F Masseni, and D Pastrone. “Uncertainty Analysis and Robust Design for a Hybrid Rocket Upper Stage”. In: *Journal of Spacecraft and Rockets* (2019), pp. 1–8.
- [6] Lorenzo Casalino, Francesca Letizia, and Dario Pastrone. “Optimization of hybrid upper-stage motor with coupled evolutionary/indirect procedure”. In: *Journal of Propulsion and Power* 30.5 (2014), pp. 1390–1398.
- [7] Lorenzo Casalino, Filippo Masseni, and Dario Pastrone. “Optimization of Hybrid Rocket Engines for Small Satellite Launchers”. In: *2018 Joint Propulsion Conference*. 2018, p. 4926.
- [8] Lorenzo Casalino, Filippo Masseni, and Dario Pastrone. “Viability of an Electrically Driven Pump-Fed Hybrid Rocket for Small Launcher Upper Stages”. In: *Aerospace* 6.3 (2019), p. 36.
- [9] Lorenzo Casalino and Dario Pastrone. “A straightforward approach for robust design of hybrid rocket engine upper stage”. In: *51st AIAA/SAE/ASEE Joint Propulsion Conference*. 2015, p. 4202.
- [10] Lorenzo Casalino and Dario Pastrone. “Optimal design and control of hybrid rockets for access to space”. In: *41st AIAA/ASME/SAE/ASEE Joint Propulsion Conference & Exhibit*. 2005, p. 3547.
- [11] Lorenzo Casalino and Dario Pastrone. “Optimal design of hybrid rocket motors for launchers upper stages”. In: *Journal of Propulsion and Power* 26.3 (2010), pp. 421–427.
- [12] Lorenzo Casalino and Dario Pastrone. “Optimal design of hybrid rocket motors for microgravity platform”. In: *Journal of Propulsion and Power* 24.3 (2008), pp. 491–498.

REFERENCES

- [13] Lorenzo Casalino and Dario Pastrone. “Optimization of a hybrid rocket upper stage with electric pump feed system”. In: *46th AIAA/ASME/SAE/ASEE Joint Propulsion Conference & Exhibit*. 2010, p. 6954.
- [14] Lorenzo Casalino and Dario Pastrone. “Optimization of hybrid sounding rockets for hypersonic testing”. In: *Journal of Propulsion and Power* 28.2 (2012), pp. 405–411.
- [15] John W Herrick. *Rocket encyclopedia: illustrated*. Aero Publishers, 1959, p. 320.
- [16] Elizabeth Jens et al. “Design of a Hybrid CubeSat Orbit Insertion Motor”. In: *52nd AIAA/SAE/ASEE Joint Propulsion Conference*. 2016, p. 4961.
- [17] MA Karabeyoglu, D Altman, and Brian J Cantwell. “Combustion of liquefying hybrid propellants: Part 1, general theory”. In: *Journal of Propulsion and Power* 18.3 (2002), pp. 610–620.
- [18] Ashley C Karp et al. “A Hybrid Mars Ascent Vehicle Concept for Low Temperature Storage and Operation”. In: *52nd AIAA/SAE/ASEE Joint Propulsion Conference*. 2016, p. 4962.
- [19] G Marxman and M Gilbert. “Turbulent boundary layer combustion in the hybrid rocket”. In: *Symposium (International) on Combustion*. Vol. 9. 1. Elsevier. 1963, pp. 371–383.
- [20] GA Marxman, CE Wooldridge, and RJ Muzzy. “Fundamentals of hybrid boundary-layer combustion”. In: *Progress in Astronautics and Rocketry*. Vol. 15. Elsevier, 1964, pp. 485–522.
- [21] Gerald A Marxman. “Combustion in the turbulent boundary layer on a vaporizing surface”. In: *Symposium (International) on Combustion*. Vol. 10. 1. Elsevier. 1965, pp. 1337–1349.
- [22] George E Moore. “A Solid-Liquid Rocket Propellant System”. In: *Journal of Jet Propulsion* 26.11 (1956), pp. 965–968.
- [23] R Muzzy. “Applied hybrid combustion theory”. In: *8th Joint Propulsion Specialist Conference*. 1972, p. 1143.
- [24] Dario Pastrone and Lorenzo Casalino. “Optimal Robust Design of Hybrid Rocket Engines”. In: *Space Engineering*. Springer, 2016, pp. 269–285.

Chapter 3

Uncertainty and Robust Design

3.1 Introduction

The term uncertainty-based design is usually used to describe design problems whose formulation is non-deterministic, i.e. some crucial components of the design problem (e.g. statement, experimental data or computational solutions) are regarded as non-deterministic.[5] Uncertainty-based design problems can be distinguished in robust-based and reliability-based design and optimization problem. Robust-based design is such that resulting system performance are relatively insensitive to fluctuation in the non-deterministic components of the problem, whereas reliability-based design is such that failure probability is lower than an acceptable threshold, despite the presence of non-deterministic components in the problem formulation.

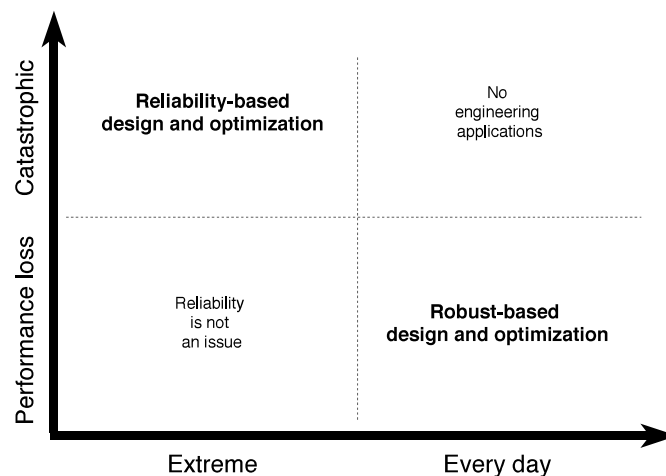


Figure 3.1: Uncertainty-based design domains.

A better understanding of uncertainty-based design domains can be achieved by

means of Fig. 3.1.[2] On the x-axis is reported the frequency of an event, whereas the y-axis presents its relative impact. If everyday (i.e. certain) fluctuations result in catastrophic events, no applications are viable from an engineering point of view (top right corner in Fig. 3.1). Instead, the design should be able to tolerate such fluctuation, i.e. be robust, anyway granting good performance (bottom right corner). On the other hand, if extreme events could lead to catastrophic effects on the system, the design should grant that such events are very unlikely, i.e. be reliable (top left corner). In the end, if system performance losses are due to extreme events, uncertainty in the design is not an issue (bottom left corner).

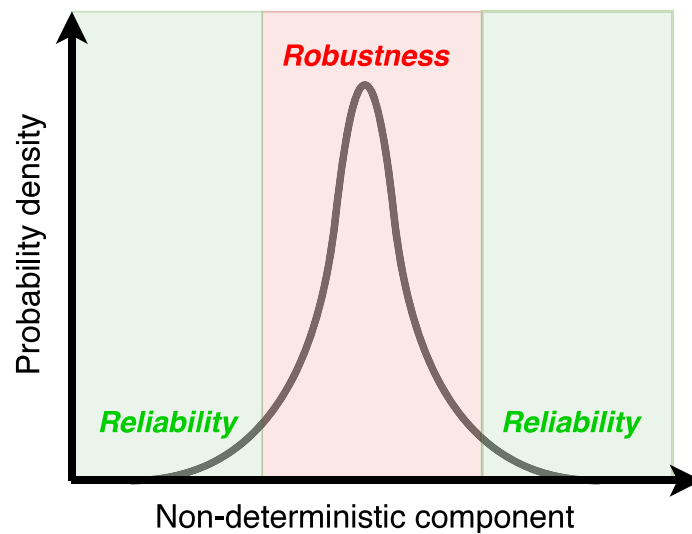


Figure 3.2: Robustness vs. reliability

The dualism of robust-based and reliability-based design can also be explained looking at the Probability Density Function (PDF) of a non-deterministic component of the problem, reported in Fig. 3.2. Basically, robust-based design deals with events concerning the fluctuation around the mean value of the PDF, whereas reliability-based design events in its tails. Traditional design procedures, which involve factor of safety and knockdown factors, fail in uncertainty-based design, because no robustness or reliability measures are provided by the design process. Moreover, traditional design procedures lack of the proper tools for uncertainty characterization and management.

3.2 Classification and Management

In uncertainty-based design uncertainties are classified as computational or experimental ones. Computational uncertainties can further be distinguished in parameter uncertainties and model form uncertainties. The former are those uncertainties related to the inputs or the intrinsic parameters that define a computational process, whereas the latter are associated with model validity, i.e. the actual adherence of the mathematical model to the physical reality of the problem. The terminology model uncertainty can be also used to indicate uncertainties in the model due to both parameters and model form uncertainties. An alternative classification, proposed by Oberkampf et al. [3], is based on the differences in the approaches used to manage and characterize uncertainty. Three classes are defined:

- variability as *the inherent variation associated with the physical system or the environment under consideration*;
- uncertainty as *a potential deficiency in any phase or activity of modeling and simulation that is due to lack of knowledge*;
- error as *a recognizable deficiency in any phase or activity of modeling and simulation that is not due to lack of knowledge*. It should be noted that either acknowledged error or unacknowledged error exist.

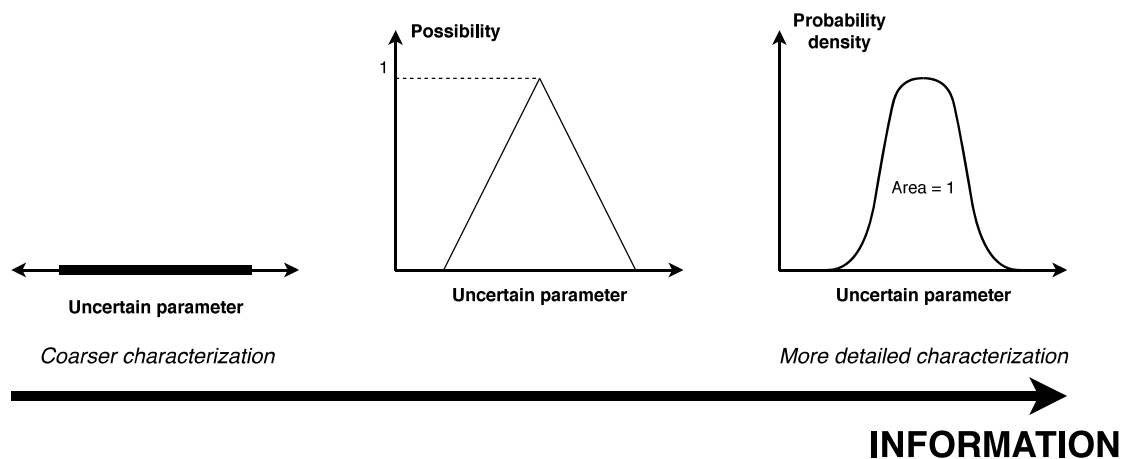


Figure 3.3: Parameter uncertainties management approaches: interval bounds, membership functions and PDFs

Concerning numerical models, three are the main approaches to parameter uncertainties management, as presented in Fig. 3.3: interval bounds, membership functions and PDFs. Interval bound is the simpler and coarser one, requiring only the lower and the upper bound of the uncertain parameter. On the other

hand, PDFs are the most precise approach, but need more information about the uncertain parameter, which are not always available. Membership functions are somewhere between interval bounds and PDFs and are widely used in fuzzy logic. The characterization of model form uncertainties, on the contrary, is not as well developed. Systematic approaches are available for discretization error only (e.g. mesh refinement), that unfortunately is only a part of the uncertainty in numerical model outputs.

3.3 Quality and Robustness

After World War II, Japan was going to stand out in the international market improving the quality of its productive system. Dr. Genichi Taguchi took the challenge and between the 50's and the early 60's developed the basis of robust design. The first concept that has to be introduced is quality. Taguchi defines the quality of a product, a process or a service in terms of “the total loss to society due to functional variation and harmful side effects”[4]. Thus the quality is in inverse relation to performance deviation from nominal ones and quality improvement requires deviation reduction. The second key concept introduced by Taguchi is that variations in system performance have to be reduced without eliminating their causes, because it can be either impossible or too costly, through a proper optimization process that makes the performance insensitive to the source of the variations. Taguchi calls this process parameter design.

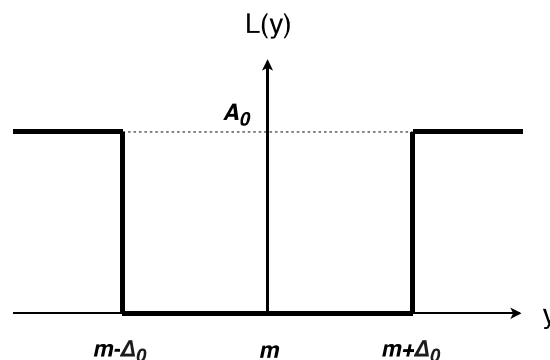


Figure 3.4: Classical concept of quality: the step function. $m \pm \Delta_0$ are engineering specifications, m is the target performance, $L(y)$ is the quality loss function and A_0 is the cost linked to system failure.

Engineering specification are invariably defined by means of tolerances: a system that meets tolerances is good whereas a system that does not is bad. Taguchi's concept of quality requires a different approach because systems could present quality losses, despite meeting tolerances, having not exactly the target performance.

Formally, the quality loss is described by a step function (see Fig. 3.4), when traditional engineering approaches are used.

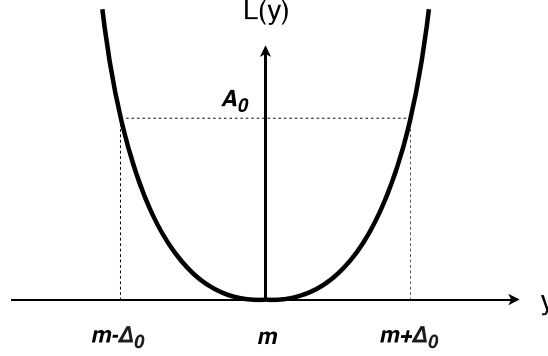


Figure 3.5: Quadratic loss function.

Taguchi’s approach, on the other hand, makes use of a quadratic loss function defined by means of Eq.(3.1) and plotted in Fig. 3.5, where m is the target performance, y is the actual performance, $L(y)$ is the associated quality loss and $k = \text{constant}$ is here called quality loss coefficient.

$$L(y) = k(y - m)^2 \quad (3.1)$$

The quadratic loss function is such that $L(y = m) = 0$ and $L(y)$ increase is limited near the condition $y = m$ and grows faster the farther away from there. The value of k defines the rate of increasing and can be defined by means of Eq.(3.2), where A_0 is the cost related to system failure and $m \pm \Delta_0$ are the functional limits for y , i.e. the values of y such that the system will incur in a failure half the time.

$$k = \frac{A_0}{\Delta_0^2} \quad (3.2)$$

Hence, the quadratic loss function can be rewritten substituting Eq.(3.2) in Eq.(3.1), giving:

$$L(y) = \frac{A_0}{\Delta_0^2}(y - m)^2 \quad (3.3)$$

This formulation of the loss function is well suited when m is a finite value and the loss is symmetric with respect to the target performance, i.e. both lower than nominal and higher than nominal performance affect equally negatively on system quality. This quality characteristics was called “nominal-the-best” by Taguchi. Other quality loss functions have to be defined accordingly to system characteristics:

- “smaller-the-better”, target performance $m = 0$ and $y \geq 0$, resulting in the quality loss function reported in Eq.(3.4);

$$L(y) = ky^2 \quad (3.4)$$

- “larger-the-better”, target performance $m = +\infty$ and $y \geq 0$, resulting in the quality loss function reported in Eq.(3.5). In this case $k = A_0\Delta_0^2$ obtained analogously to what done for the “nominal-the-best” loss function;

$$L(y) = k \left(\frac{1}{y^2} \right) \quad (3.5)$$

- asymmetric loss function, analogous to “nominal-the-best” function but two different values of k are employed for positive and negative off-nominal performance, as reported in Eq.(3.6). This loss function have to be used when quality deviations in a direction are far worst than in the other one.

$$L(y) = \begin{cases} k_1(y - m)^2 & \text{if } y > m \\ k_2(y - m)^2 & \text{if } y \leq m \end{cases} \quad (3.6)$$

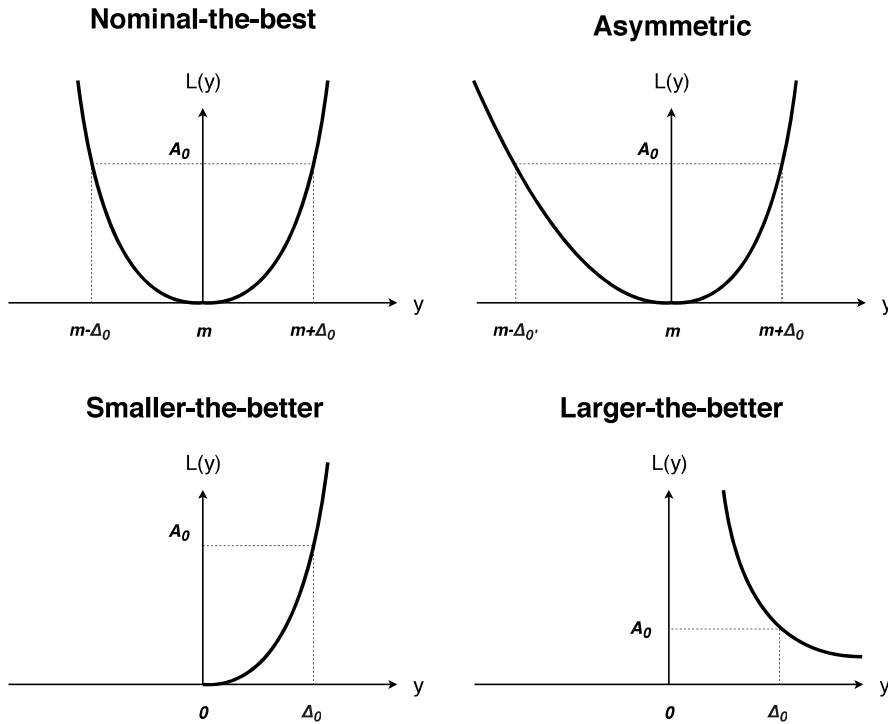


Figure 3.6: Quadratic loss function comparison.

System performance, measured by the quality loss functions previously defined, are prone to variation due to many causes in actual operation. These causes are called noise factors in the context of Taguchi’s method. Concerning a certain system, noise factors can be distinguished in external (due to environment and work

load, e.g. temperature, humidity, vibrations, human error, etc), unit-to-unit variation (due to the manufacturing process, formally identical products could show slightly different characteristics) and deterioration (due to wear and ageing). Manufacturing process itself is affected by noise factors, categorized in external to the process (e.g. variation in the raw material and manufacturing environmental condition), process non-uniformity (e.g. differences due to item position in a simultaneous process) and process drift (wearing of tools and machines could cause quality deviation throughout production).

Quality (i.e. performance) varies from a system to an other, despite being formally identical, or throughout time because of noise factors. Hence an average quality loss Q can be defined, considering for example a nominal-the-best loss characteristic and a group of n systems, being m the target performance:

$$Q = \frac{1}{n} \sum_{i=1}^n L(y_i) = \frac{k}{n} \sum_{i=1}^n (y_i - m)^2 = k \left[(\mu - m)^2 + \frac{n-1}{n} \sigma^2 \right] \quad (3.7)$$

$$\mu = \frac{1}{n} \sum_{i=1}^n y_i \quad (3.8)$$

$$\sigma^2 = \frac{1}{n-1} \sum_{i=1}^n (y_i - \mu)^2 \quad (3.9)$$

where quality loss is expressed by means of Eq.(3.1). The mean μ and the variance σ^2 of y are introduced in Eq.(3.7) and defined in Eq.(3.8) and (3.9). If the number n is large, the term $\frac{n-1}{n} \approx 1$ and thus the average quality loss Q can be rewritten as:

$$Q = k[(\mu - m)^2 + \sigma^2] \quad (3.10)$$

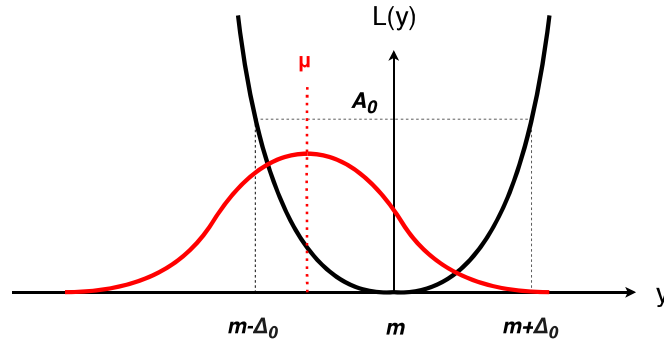


Figure 3.7: Quality loss distribution with $\mu \neq m$ and $\sigma^2 \neq 0$.

Looking at Eq.(3.10), one can notice that the average quality loss Q has two contributions, the first is due to the deviation of μ from the target performance m and the latter depends on the deviation of y around μ . A graphical representation of the quality loss distribution is provided by Fig.3.7. The easier quality

improvement strategy is to reduce the gap between μ and m , whereas dealing with variance is often harder and expensive: system that exhibits performance outside $m \pm \Delta^*$, with $\Delta^* < \Delta_0$ can be discarded or the source of variation can be found out and eliminated. In both cases quality will increase but the relative costs may be impractical. A third way consists in the use of the Robust Design Method (RDM), making the system less sensitive to noise factors and achieving better quality in a cheaper and more effective way.

3.4 Robust Design Method

In Fig. 3.8 the basic block diagram employed in RDM is reported: the response \mathbf{y} of a system or a product/process (i.e. its output or quality characteristic) is influenced by many factors (also called parameters in this context) that are usually classified as signal factors \mathbf{M} , noise factors \mathbf{x} and control factors \mathbf{z} .

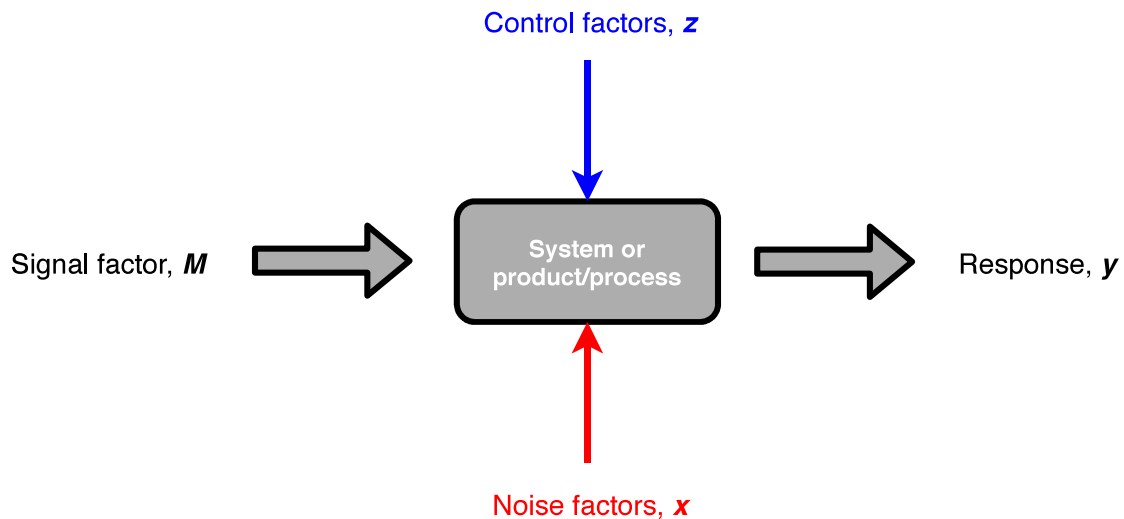


Figure 3.8: Block diagram of a system or a product/process.

Signal factors \mathbf{M} express user's will in terms of response magnitude, e.g. the throttle position in a motorcycle. Noise factors \mathbf{x} are parameters whose values cannot be set by the designer, are hard (or too costly) to control during operation and usually differ among formally identical units. The response \mathbf{y} deviates from the target specified by \mathbf{M} due to noise factors \mathbf{x} . On the other hand, the designer is free to choose the values of the control factors \mathbf{z} . Control factors that affect system cost, beyond its response, are called tolerance factors. Both noise and control factors are discretized in levels in RDM.

RDM assumes that system response is a non-linear function of noise and control factors. Under nominal noise condition, i.e. when all noise levels are at their

nominal values, many combination of the control factors can lead to the same response value. However, these designs can result in really different quality losses when noise factors are at their off-nominal values, due to the non-linearities. RDM aims at finding out the combination of control factors that gives the smallest quality characteristic variation around its target value.

$$\mathbf{y} = f(\mathbf{x}, \mathbf{z}) \quad (3.11)$$

One can consider, as an example, the simple relation presented in Eq.(3.11), where $\mathbf{x} = [x_1, \dots, x_n]$ and $\mathbf{z} = [z_1, \dots, z_m]$ express, respectively, noise and control factors in a vectorial form. Response deviation $\Delta\mathbf{y}$ due to noise factors variations $\Delta\mathbf{x}_i$ from nominal conditions can be written by means of Eq.(3.12).

$$\Delta\mathbf{y} = \sum_{i=1}^n \left(\frac{\partial f}{\partial x_i} \Delta x_i \right) \quad (3.12)$$

Moreover, if noise factors deviations $\Delta\mathbf{x}_i$ are not correlated, the variance of the response σ_y^2 can be written as a function of the individual noise factor variances $\sigma_{x_i}^2$, as reported in Eq.(3.13). The terms $\left(\frac{\partial f}{\partial x_i}\right)^2$ are called sensitivity coefficients in RDM and are functions of \mathbf{x} too. A robust design (product, process or system) is such that its sensitivity coefficients are the smallest.

$$\sigma_y^2 = \sum_{i=1}^n \left[\left(\frac{\partial f}{\partial x_i} \right)^2 \sigma_{x_i}^2 \right] \quad (3.13)$$

RDM employs orthogonal arrays to perform experiments and obtain robustness in the design efficiently. A proper discretization of the design space is made by means of a certain number of finite levels for the control factors, e.g. “lower than nominal”, “nominal” and “higher than nominal”, when three levels are employed. Noise factors are discretized in levels too, but, in general, the number of noise levels and control levels can be different.

Two orthogonal arrays, called inner and outer, are used to specify levels combination respectively for control and noise factors. For each combination of control factors (i.e. for each row of the inner array) a bunch of tests is performed, varying noise factors values accordingly to the outer array. Thus, being p and q the number of row of the inner and outer array, the total number of tests required by RDM is $p \cdot q$. All the tests are often listed in the form of a third array, called crossed array in the RDM.

Examples of orthogonal arrays are reported in Tab. 3.1-3.3, where factors are represented by the capital letters. L_8 is a 2-levels array suitable to deal with up to seven factors, whereas L_9 is a 3-levels array able to manage up to four factors. L_{18} orthogonal array has 2 levels for one factor (A) and 3 levels for the other seven factors (from B to H).

Table 3.1: L_8 orthogonal array.

Test #	A	B	C	D	E	F	G
1	1	1	1	1	1	1	1
2	1	1	1	2	2	2	2
3	1	2	2	1	1	2	2
4	1	2	2	2	2	1	1
5	2	1	2	1	2	1	2
6	2	1	2	2	1	2	1
7	2	2	1	1	2	2	1
8	2	2	1	2	1	1	2

Table 3.2: L_9 orthogonal array.

Test #	A	B	C	D
1	1	1	1	1
2	1	2	2	2
3	1	3	3	3
4	2	1	2	3
5	2	2	3	1
6	2	3	1	2
7	3	1	3	2
8	3	2	1	3
9	3	3	2	1

Once all tests have been performed, the designer is able to estimate control factors effects. RDM defines a “signal-to-noise (S/N) ratio” η_i through Eq.(3.14), where G_i is the mean of a certain quality loss function or generic performance to be minimized for the i -th tests prescribed by the employed inner array (i.e. the mean output of the set of tests performed with constant control factors and variable noise factors).

$$\eta_i = -10 \log_{10} (G_i) \quad (3.14)$$

The overall mean value m of η_i for the tests can be computed by means of Eq.(3.15), where n_{in} denotes the number of tests prescribed by the inner array employed. Analogously, the effect of a factor level (i.e. the average deviation that it can cause from the overall mean) is calculated as the difference between the mean of the η_i in which that factor assumes that level and the overall mean m . Considering, for example, an L_8 array reported in Tab.3.1 as inner array, one can notice that the factor D is at its level 2 in the second, fourth, sixth and eighth test,

Table 3.3: L_{18} orthogonal array.

Test #	A	B	C	D	E	F	G	H
1	1	1	1	1	1	1	1	1
2	1	1	2	2	2	2	2	2
3	1	1	3	3	3	3	3	3
4	1	2	1	1	2	2	3	3
5	1	2	2	2	3	3	1	1
6	1	2	3	3	1	1	2	2
7	1	3	1	2	1	3	2	3
8	1	3	2	3	2	1	3	1
9	1	3	3	1	3	2	1	2
10	2	1	1	3	3	2	2	1
11	2	1	2	1	1	3	3	2
12	2	1	3	2	2	1	1	3
13	2	2	1	2	3	1	3	2
14	2	2	2	3	1	2	1	3
15	2	2	3	1	2	3	2	1
16	2	3	1	3	2	3	1	2
17	2	3	2	1	3	1	2	3
18	2	3	3	2	1	2	3	1

thus the mean has to be calculated from the corresponding four values η_2 , η_4 , η_6 and η_8 . Thus, the mean m_{D_2} can be computed as reported in Eq.(3.16) and the main effect is then $m_{D_2} - m$. The same can be done for all the other effects.

$$m = \sum_{i=1}^{n_{in}} \eta_i \quad (3.15)$$

$$m_{D_2} = \frac{1}{4} (\eta_2 + \eta_4 + \eta_6 + \eta_8) \quad (3.16)$$

Once factors effects have been estimated, a procedure, called ANalysis Of Means (ANOM) in the RDM, is performed. A graphical representation of the ANOM is given in Fig. 3.9. The optimum level for each factor is the one which results in the highest S/N ratio. Thus, in the example presented in Fig.3.9, the optimum factors levels are A_2 , B_1 , C_1 , D_2 , E_1 , F_2 and G_1 . The optimal combination of levels may not correspond to any of the rows of the inner array used in the RDM.

Moreover, S/N ratios are able to provide information about the relative magnitude of the factors effects on the system performance thanks to variance decomposition. In RDM this phase is called ANalysis Of VAriance (ANOVA). The outputs

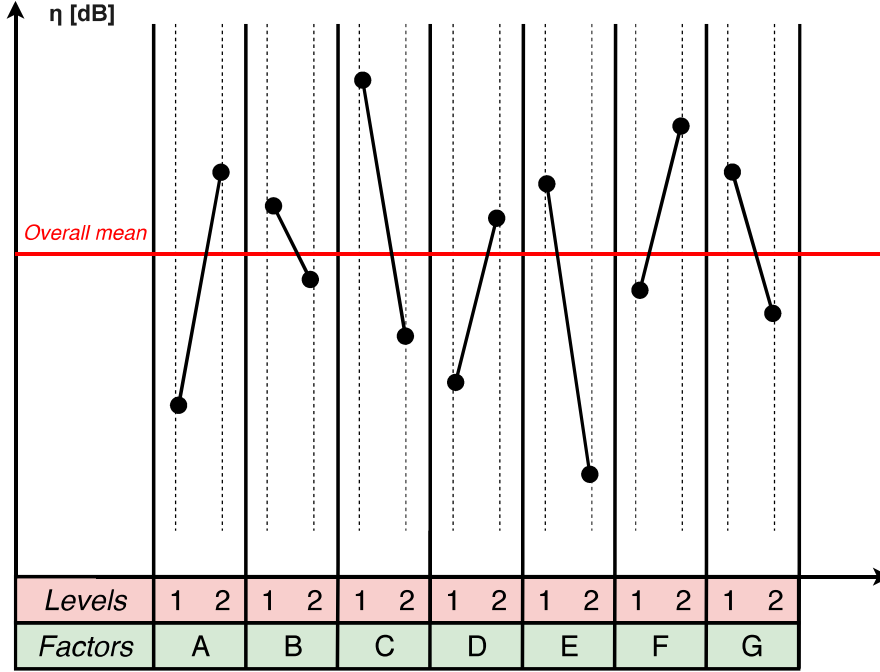


Figure 3.9: Graphical representation of the ANOM (2 levels and 8 control factors have been considered).

of the ANOVA are the sum of squares due to a certain factor k :

$$SS_k = \sum_{i=1}^L [n_k (m_{k_i} - m)^2] \quad (3.17)$$

where n_k is the number of experimental tests in which the factor k assumes the i -th level. The higher is the value of SS_k , the greater is the portion of the total variation of η due to a variation in the factor k .

3.5 Conclusions

Orthogonal arrays, ANOM and ANOVA constituted the basis of robust optimization approaches developed by the author first in his Master Degree Thesis and then in [1]. Taguchi's RDM proved to be suitable as a local search procedure or an enhancement of evolutionary algorithms. However, results underlined that the use of the RDM as a stand alone global optimization procedure leads to poor performance.

In the present work, the tools of RDM have not been employed as design by Taguchi himself, but the basic concepts behind RDM are still valid: the distinction between control and noise factor, the basic concept of robustness as the insensitivity

of system performance to uncertain parameters variation, the duality of system mean performance and its variance and the importance of the relative contributions of factor to overall system variability.

Hence, the core tools required by a robust-based optimization procedure are basically three:

1. a method to identify noise factors among the set of problem parameters;
2. an approach able to consider both mean problem response and variance due to uncertainty within optimization merit function;
3. an efficient global optimization algorithm which leads the whole procedure.

In the following Chapter, the author will introduce his robust-based optimization procedure, which consists of sensitivity analysis and parameters screening method (4.1), design of experiments techniques (4.2) and particle swarm optimization algorithm (4.3).

References

- [1] L Casalino, F Masseni, and D Pastrone. “Robust Design Approaches for Hybrid Rocket Upper Stage”. In: *Journal of Aerospace Engineering* 32.6 (2019), p. 04019087.
- [2] Luc Huyse and R Michael Lewis. *Aerodynamic shape optimization of two-dimensional airfoils under uncertain conditions*. Institute for Computer Applications in Science and Engineering, NASA Langley, 2001.
- [3] William L Oberkampf et al. “Variability, uncertainty, and error in computational simulation”. In: *ASME-PUBLICATIONS-HTD* 357 (1998), pp. 259–272.
- [4] Madhan Shridhar Phadke. *Quality engineering using robust design*. Prentice Hall PTR, 1995.
- [5] Thomas A Zang et al. “Needs and opportunities for uncertainty-based multidisciplinary design methods for aerospace vehicles”. In: (2002).

Chapter 4

Robust-based Optimization

4.1 Sensitivity analysis and screening

Sensitivity analysis (SA) methods are crucial in the definition of a robust-based numerical model. In general, complex and/or multi-disciplinary models can be characterized by an extremely high number of parameters, which can probably include some uncertain parameters. Insight about how uncertainties in numerical models inputs could affect their outputs is mandatory when robustness in the design have to be obtained. Local SA methods focus on outputs deviations, due to modest perturbations of model inputs parameters around their reference or nominal values, by partial derivative estimation around a given design point. This approach fails when strong non-linearity are involved in the numerical model. In fact, a small fluctuation of a certain input parameter can have a negligible or decisive impact on model outputs, depending on the point in the design space around which that fluctuation takes place. On the other hand, global SA methods allow for the quantification of outputs deviations, due to inputs perturbations, regardless of the design point. Thus, global SA methods are helpful to recognize the most influential input parameters, whose uncertainties can not be neglected, and non influential ones, that can be regarded as constants, making easier the building process of a numerical model. Moreover, in robust-based approaches, a proper selection of uncertain parameters is strongly advisable to avoid unnecessary model complexity.

Main SA methods are shown in Fig.4.1.[8] In the present work, a single model evaluation requires a significant amount of time (roughly few seconds) and, on the other hand, the numerical model is characterized by non-linearity and domain discontinuity (details about mathematical model will be given in Chapter 5). Hence, Morris method has been chosen by the author to perform SA and parameters screening because requires the lowest number of model evaluations, among the group of approaches well suited for highly complex numerical model.

Morris method, also known as the Elementary Effects method, aims at dividing model input parameters into three groups: parameters with negligible, linear and

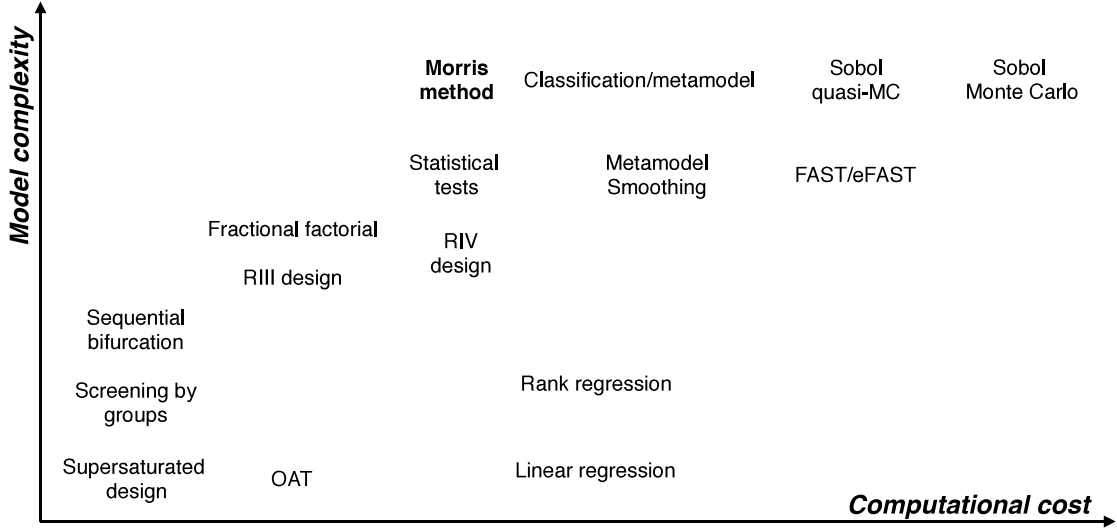


Figure 4.1: SA methods classification.

additive or non-linear effects on model outputs.[10] Input parameters are discretized in m finite levels and then model evaluation are performed to compute incremental ratios, called Elementary Effects (EE), in which input parameters are varied One at A Time (OAT), while keeping the others fixed. Starting input point, order and direction of the parameters variations are random. Being N_{inp} the number of input parameters, $N_{inp} + 1$ model evaluation are required to compute N_{inp} elementary effect. This set of EE forms a so called Morris trajectory. Trajectories computation is repeated typically $10 \leq r \leq 50$ times.[2] Thus, the overall number of model evaluation required by Morris method is equal to $r(N_{inp} + 1)$.

$$E_j^{(i)} = \frac{F_i(\mathbf{X}^{(i)} + \Delta \mathbf{e}_j) - F_i(\mathbf{X}^{(i)})}{\Delta} \quad (4.1)$$

Formally, the EE of the j -th input parameter at the i -th repetition is computed as reported in Eq.(4.1), where F denotes the generic numerical model output, \mathbf{X} the input parameters vector, Δ is the relative input parameter variation and \mathbf{e}_j is a vector of the canonical base (i.e. all its elements are zeros, but the j -th that is equal to one). Two sensitivity measures, also known as Morris indices, are then computed: the mean of the absolute values μ_j^* of $E_j^{(i)}$ and its standard deviation σ_j (Eq.(4.2) and (4.3)). If a variation in the j -th input parameter value has negligible effects on model outputs, its μ_j^* will be small, and vice-versa. On the other hand, σ_j expresses the non-linearity in the model outputs due to the j -th parameter: small values of σ_j characterize input parameters whose effect is the same all over the input space, suggesting a linear relationship between that input and model outputs. Instead, large values of σ_j highlight that the effect of the j -th parameter

depends on the starting point in the input space.

$$\mu_j^* = \frac{1}{r} \sum_{i=1}^r |E_j^{(i)}| \quad (4.2)$$

$$\sigma_j = \sqrt{\frac{1}{r} \sum_{i=1}^r \left(E_j^{(i)} - \frac{1}{r} \sum_{i=1}^r E_j^{(i)} \right)^2} \quad (4.3)$$

Usually, a graphical representation of Morris indices is employed to perform input parameters screening. Parameters s.t. $\mu_j^* \gg 0$ and $\sigma_j \gg 0$ (top right in Fig.4.2) are the most significant ones, in SA, because their influence on model output is consistent and variable among the input space. This behavior can not be neglected when the numerical model is defined and its management is even thorny when robust-based design is considered. On the other hand, parameters s.t. $\mu_j^* \approx 0$ and $\sigma_j \approx 0$ (bottom left in Fig.4.2) are not an issue in the definition of the numerical model, they can simply be treated as constant since their influence on model output is minor or null. Parameters s.t. $\mu_j^* \approx 0$ but $\sigma_j \gg 0$ (top left in Fig.4.2) are characterized by little or negligible influence on model outputs but exhibit interactions with other parameters or non-linearity. In the end, parameters s.t. $\mu_j^* \gg 0$ but $\sigma_j \approx 0$ (bottom right in Fig.4.2) show remarkable linear influences on model outputs but a lack of interactions with other input parameters.

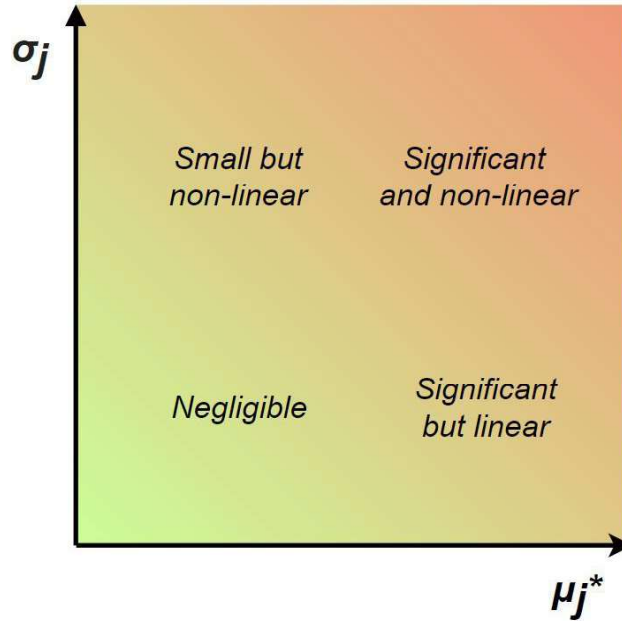


Figure 4.2: Graphical representation of Morris indices.

In the following, a simple numerical example of the employment of Morris method in a SA and screening is presented. Three input parameters (i.e. $N_{inp} = 3$),

discretized in 3 levels each (i.e. $m = 3$), are considered to perform a better representation of Morris trajectories in a 3-dimensional input space. Only one random starting input point and three repetition (i.e. $r = 3$) are employed, for simplicity. The numerical model has only one output that is $F(a, b, c) = ab - c$. All input parameters have the same levels, whose values are 1, 3 and 5. Looking at the formal expression of $F()$ one could suppose that a and b will show large and non-linear influences, whereas the impact of c will be smaller and linear.

The first trajectory starts from the point (3,3,3), thus $F_1^{(1)} = 3 \cdot 3 - 3 = 6$. The second point of the trajectory is (3,3,1), that is a negative variation of the third parameter, thus $F_2^{(1)} = 3 \cdot 3 - 1 = 8$. The third point is (3,5,1), that is a positive variation of the second parameter, thus $F_3^{(1)} = 3 \cdot 5 - 1 = 14$. The fourth point is (1,5,1), that is a negative variation of the first parameter, thus $F_4^{(1)} = 1 \cdot 5 - 1 = 4$. Elementary effects are computed by means of Eq.(4.1), where one always has $\Delta = 2$, giving $E_1^{(1)} = -5$, $E_2^{(1)} = 3$ and $E_3^{(1)} = 1$. The second trajectory starts again from the point (3,3,3), thus $F_1^{(2)} = F_1^{(1)} = 6$, but the order and direction of parameters variation are different, because they are both randomly chosen: $F_2^{(2)} = 3 \cdot 5 - 3 = 12$, $F_3^{(2)} = 3 \cdot 5 - 5 = 10$ and $F_4^{(2)} = 1 \cdot 5 - 5 = 0$. The corresponding EE are: $E_1^{(2)} = -5$, $E_2^{(2)} = 3$ and $E_3^{(2)} = -1$. Analogously stands for the third trajectory: $F_1^{(3)} = F_1^{(1)} = 6$, $F_2^{(3)} = 5 \cdot 3 - 3 = 12$, $F_3^{(3)} = 5 \cdot 3 - 1 = 14$, $F_4^{(3)} = 5 \cdot 1 - 1 = 4$, leading to $E_1^{(3)} = 3$, $E_2^{(3)} = -5$ and $E_3^{(3)} = 1$.

$E_j^{(i)}$ are reported in Tab. 4.1 alongside with the corresponding values of μ_j^* and σ_j . A graphical representation of Morris indices for the considered numerical example is given in Fig. 4.3 and trajectories are plotted in Fig. 4.4. One can observe that a and b exhibits a similar, strong and non-linear influences on $F()$, whereas the influence of c on the example output is far more limited. This is an useful example to understand how Morris method works, but clearly actual SA requires a greater number of random starting point and an higher number of repetition (at least ten).

Table 4.1: $E_j^{(i)}$, μ_j^* and σ_j for the numerical example.

	T1	T2	T3	μ_j^*	σ_j
$E_1^{(i)}$	-5	-5	3	4.33	3.77
$E_2^{(i)}$	3	3	-5	3.67	3.77
$E_3^{(i)}$	1	-1	1	1.00	0.94

In robust-based optimization models, SA and screening are matchless tools. Robust approaches distinguish parameters, involved in a numerical model, in design and input parameters. The former can be freely adjusted by the designer to obtain the required performance, whereas the latter could be affected by uncertainty. SA allows for the identification of the most significant uncertainty sources, that are the most influential input parameters. At the same time, the less influential parameters

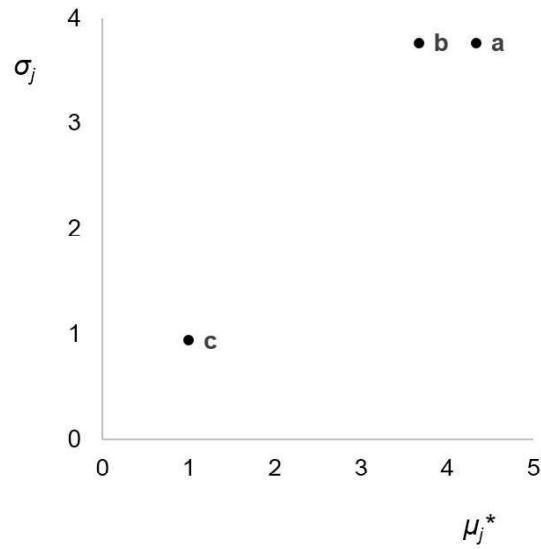


Figure 4.3: Graphical representation of Morris indices for the numerical example.

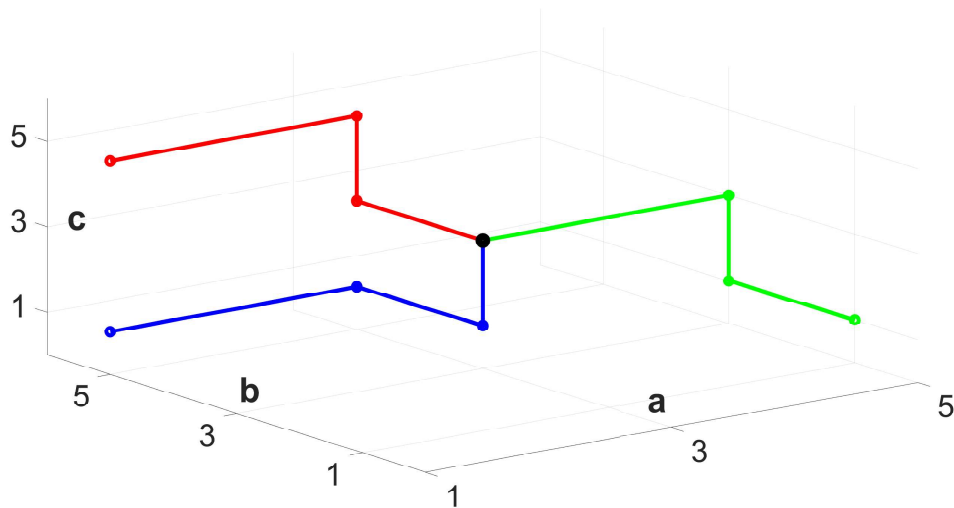


Figure 4.4: Graphical representation of Morris trajectories in the input domain. Dot markers represent $F_j^{(i)}$ evaluation. Blue, red and green lines are the first, second and third trajectory, respectively. The black dot marker is the starting point $a = 3$, $b = 3$ and $c = 3$ of the trajectories. The order of OAT parameters variations and variation directions are both randomly chosen.

can be considered as constant in the robust-based model.

Since design parameters are not input ones in robust-based design and optimization, the starting points for Morris trajectories are randomly chosen inside

design domain instead of inside input domain. Then, OAT variations of input parameters are performed aiming at exploring the input domain of the problem and obtain SA results. Clearly, some form of acceptance criterion, for example on the attained performance, must be applied to the starting points for the SA. In this way, one can avoid useless and counter-productive analysis of unfeasible part of the design domain or testing design condition resulting in poor performance. The author will apply Morris method to perform SA and screening of the considered HRE design and optimization in Sec.5.4.1. Concerning HRE optimization, for example, the effects of a certain input variation around a design point corresponding to a launcher unable to lift-off, not only are not relevant, but are also a waste of model evaluations, when the optimal design of the same launcher have to be found out.

Once uncertain parameters have been selected among input parameters, by means of SA and screening, proper techniques to evaluate their actual effects on model outputs have to be employed. Thus, in the following Sec. 4.2 approaches for uncertainty management will be detailed.

4.2 Design of Experiments

An experiment can be defined as a set of tests in which model outputs are evaluated modifying input parameters aiming at finding out the relationships between input variations and model response. Design Of Experiments (DOE) is the set of techniques and methods developed to guide the choice of the experiments to be performed in the most efficient and effective way. Three are the basic principles involved: replication, randomization and blocking. Replication implies the repetition of the experiments, aiming at the evaluation of mean values and the relative deviations. Randomization avoids relationships between previous and current test or current and subsequent one. Blocking is employed to isolate a bias effect, preventing main ones suppression, by means of groups of similar experiments. Main DOE techniques, that are usually employed in the literature[6], are the following:

- Randomized Complete Block Design (RCBD), that focus on the evaluation of the influence of one parameter, called here primary, design or control factor. The other parameters are called nuisance factors or disturbance factors. Primary and nuisance factors can be discretized in a different number of levels L_i and the number of model evaluation required by the DOE is then $N_{ME}(L_i) = \prod_{i=1}^k L_i$, where k is the number of factors. One can notice that the growth of N_{ME} results to be strongly dependent on the number of factors k ;
- Latin square design, that shares the core idea with RCBD, requires far less model evaluations but strict conditions to be applied: $k = 3$ (one primary and two nuisance factors) and $L_i = L$ for $i = 1,2,3$, resulting in $N_{ME} = L^2$.

Actually the number of factors k can be greater than three, but different names are employed such as Graeco-Latin square and Hyper-Graeco-Latin squares;

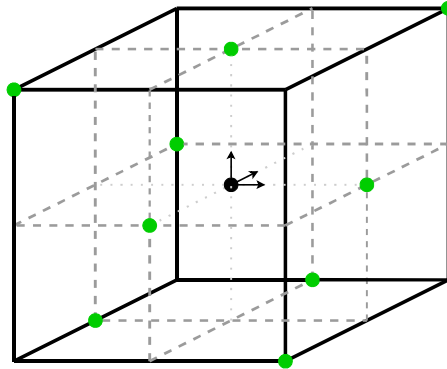


Figure 4.5: Graphical representation of a Latin square design ($k = 3$, $L = 3$, $N_{ME} = 9$): green dots are the tests to be performed and the black dot corresponds to the all-nominal condition.

- Full factorial design, that requires the evaluation of every possible combination of the factor values, which are no longer split between primary and nuisance ones. Thus, $N_{ME} = L^k$. Levels are usually two (high and low, +1 and -1, etc.) or three (high, nominal and low, +1, 0 and -1, etc.). Full factorial design is able to evaluate main effects and interactions of factors totally, but the required number of model evaluation N_{ME} grows exponentially with both k and L ;

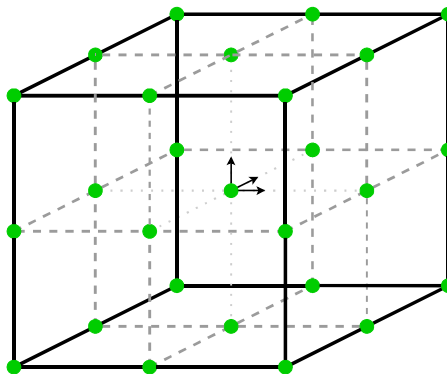


Figure 4.6: Graphical representation of a full factorial design ($k = 3$, $L = 3$, $N_{ME} = 27$): green dots are the tests to be performed. One can notice that the point corresponding to all-nominal condition is a test point too.

- Fractional factorial design, that is essentially a subset of a full factorial design, requiring less model evaluation, albeit information about mean effects and interactions of factor are more limited. Considering $L = 2$, fractional factorial design can be one-half ($p = 1$), one-quarter ($p = 2$), etc. of the full factorial design. In general, the number of model evaluation can be written as $N_{ME} = L^{k-p}$;

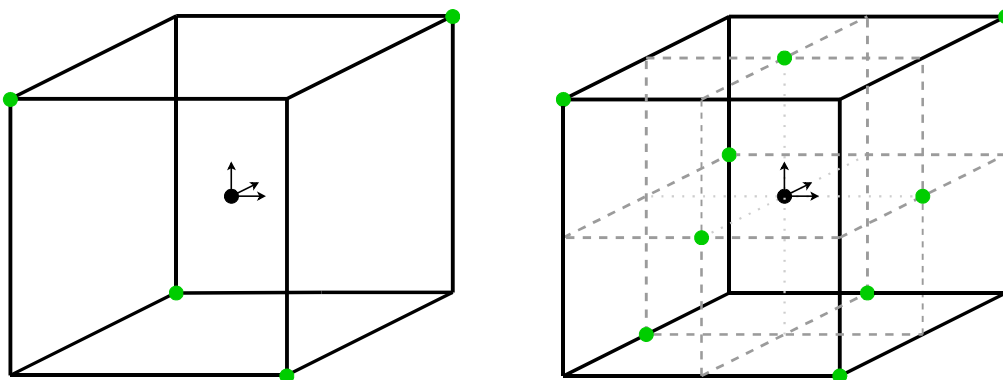


Figure 4.7: Graphical representation of fractional factorial designs (on the left $k = 3$, $L = 2$, $p = 1$, $N_{ME} = 4$ and on the right $k = 3$, $L = 3$, $p = 1$, $N_{ME} = 8$): green dots are the tests to be performed and the black dot corresponds to the all-nominal condition. One can notice that the 3^{3-1} design is equal to Latin square design with $k = L = 3$.

- Central composite design, that is a 2^k full factorial design with the addition of the central point (all factors set to their nominal values) and $2k$ star points (all factors but one set to their nominal values). Thus, $N_{ME} = 2^k + 2k + 1$ for the central composite;
- Box-Behnken design, that can be regarded as incomplete 3^k factorial designs and were developed to reduce the number of model evaluation required as k grows. Unfortunately, there are not general rules to build a Box-Behnken design, but the authors provided many designs in [1] for $3 \leq k \leq 7$, $9 \leq k \leq 12$ and $k = 16$. An example of Box-Behnken design is presented in Tab. 4.2 for $k = 6$ by means of an useful concise notation: table rows represent factorial blocks (in the present case 2^3 ones), the symbol \pm identifies the parameters involved in the factorial design, whereas the symbol 0 stands for the parameters that are fixed to their nominal level. For example, the first row represents all the $2^3 = 8$ possible combinations that can be obtained through a factorial design involving the first, second and fourth parameters, whereas the third, fifth and sixth are kept constant to their nominal value. Thus the total number of tests is equal to $6 \cdot 8 + 1 = 49$, due to the last row in which all parameters assume their nominal values;

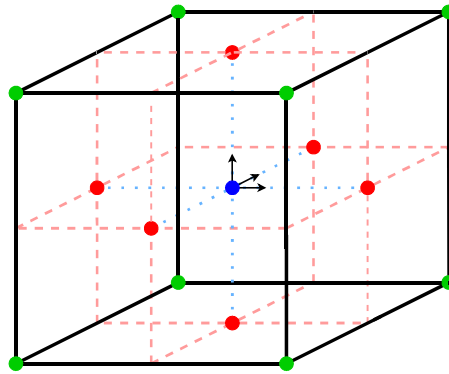


Figure 4.8: Graphical representation of a central composite design ($k = 3$, $L = 2$, $N_{ME} = 15$): green dots are the tests to be performed due to the original 2^3 full factorial design, the red dots are the $2k$ additional star points and the blue dot is the +1 additional central point corresponding to the all-nominal condition.

Table 4.2: Box-Behnken design for $k = 6$.

\pm	\pm	0	\pm	0	0
0	\pm	\pm	0	\pm	0
0	0	\pm	\pm	0	\pm
\pm	0	0	\pm	\pm	0
0	\pm	0	0	\pm	\pm
\pm	0	\pm	0	0	\pm
0	0	0	0	0	0

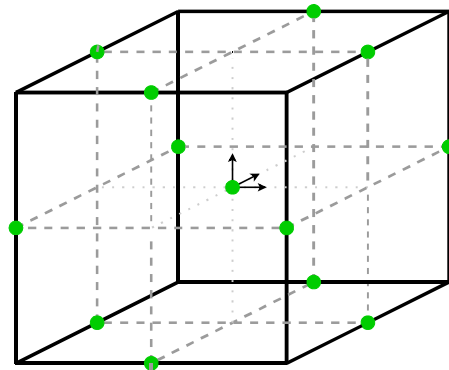


Figure 4.9: Graphical representation of a Box-Behnken design for $k = 3$ ($N_{ME} = 13$): green dots are the tests to be performed. One can notice that the prescribed tests are at the middle points of the edges of the design space with the addition of the central point corresponding to the all-nominal condition.

- Plackett-Burman design, that are two levels design requiring really few model evaluations and are able to study the influences of $k = N - 1$ factors, albeit mean effects and interactions could be confounded;
- Taguchi's method, that has been developed by Genichi Taguchi to improve the quality of Japanese products. The core idea of Taguchi's approach is to find out the best combination of control factors to minimize the variation in the output due to uncontrollable, here called noise, factors. Details about Taguchi's so called robust parameter design problem are given in Sec. 3.3. The number of model evaluations N_{ME} required by Taguchi's approach depends on the number k_{in} of controllable and k_{out} of uncontrollable factors. Proper designs are reported in [12] and Table 4.3 presents a short summary of the arrays prescribed by Taguchi's method for $2 \leq k \leq 23$ and $L = 2,3$;

Table 4.3: Taguchi's designs.

Number of parameters, k	2-levels	3-levels
2,3	L4	L9
4	L8	L9
5-7	L8	L18
8	L12	L18
9-11	L12	L27
12,13	L16	L27
14,15	L16	L36
15-23	L32	L36

- Space filling techniques, whose core idea is to fill uniformly the input space. The number of model evaluations is chosen by the designer and the discretization in levels is not required. The main application of these techniques is the building of response surfaces. Most common filling techniques are random filling, Halton, Faure and Sobol sequences and Latin Hypercube sampling;
- Optimal design, that is an iterative and really costly method aiming at the identification of the set of samples that minimize a certain function, for example the normalized average of the response variables. Optimal design is well suited and commonly used for the building of response surfaces.

In Fig.4.11 the number of model evaluations N_{ME} required by various DOE techniques is reported as a function of the number of parameters k . One can observe that, even when k is low, the number of model evaluations prescribed by full factorial, $p = 1$ fractional factorial and central composite design is remarkably high. On the other hand, Taguchi's method and Box-Behnken design are able to

grant $N_{ME} \leq 50$ for $k \leq 7$. Plackett-Burman design exhibits the smallest and almost constant number of model evaluations as k grows, also when $k \geq 7$.

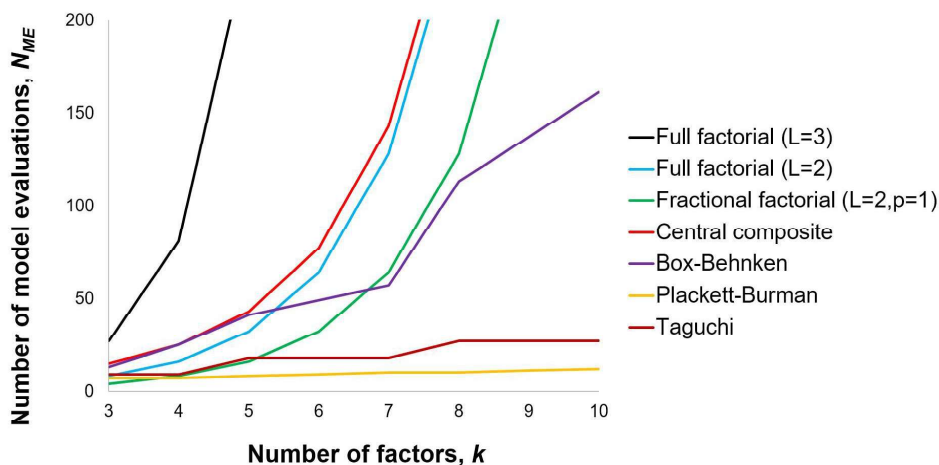


Figure 4.10: DOE technique comparison: N_{ME} vs. k .

In the present work, the robust-based optimization of an HRE is considered. Details about the test case, the mathematical model and the optimization methods will be detailed in Chapter 5. The number of uncertain parameters involved in the engine and trajectory model results to be equal to six and a single merit function evaluation requires few seconds to be performed. Thus the number of model evaluation required is the main driver in the choice of the proper DOE technique: Taguchi’s method and Box-Behnken design are both well fitted to deal with $k = 6$ parameters in robust design and optimization, whereas Plackett-Burman design fails in the quantification of mean effects of input variations on model outputs, and have to be discarded. Also a highly fractional factorial design could be employed, albeit to be competitive with Taguchi and Box-Behnken approaches, the number of model evaluation can results too low to effectively grant robustness in the design.

4.3 Optimization

The basic concept of an optimization problem can be expressed as the problem involving the research of the best solution, namely the one that minimizes or maximizes a specific merit function, among all feasible ones, given a certain set of constraints. Problem variables, in general, can be discrete or continuous and constraints can be inequalities or equalities ones. Optimization methods can be split into direct methods, indirect methods and evolutionary algorithms.

Direct methods start from a tentative solution, evaluate local gradients of merit function and constraints and then adjust the solution aiming at merit function

improvement and constraints fulfillment. Direct methods are able to deal with complex problems and constraints sets, but their computational cost is high, optimized solutions might depend on the initial guess and tend to get stuck in local optimal points. Indirect methods are well suited for continuous optimization problems described by a system of differential equations. The optimization strategy is to evaluate conditions for optimality, defining a boundary value problem, and then minimize errors on boundary conditions adjusting iteratively the solution. Indirect methods are really accurate and faster than direct methods, but can struggle against complex problems and, like direct methods, the optimized solution might be suboptimal and guess dependent. Evolutionary algorithms (EAs) are population based and excel when the number of variables is limited. A starting population of different solutions, usually randomly generated, evolves through recombination of older ones, improving the merit function. EAs do not require initial solutions and perform truly global optimization, albeit complex constraints management might be an issue. Moreover, no proof exists that the optimized solution is the actual global optimal solution, since EAs are heuristics.

In the present work, the robust design of an HRE is considered, involving coupled optimization of the propulsion system and the ascent trajectory. Trajectory is optimized by means of an indirect procedure developed at the Politecnico di Torino in the early 90's, that has been widely and successfully applied in many research activities.[4, 5] Details about the procedure will be given in Sec. 5.3. Indirect trajectory optimization can be regarded as the inner layer of a two layers optimization procedure. The outer layer concerns propulsion system optimization and once engine design parameters are given the trajectory is optimized and the merit function is computed. Here, propulsion system design is defined by means of six parameters, as will be presented in Sec. 5.4. Thus, an evolutionary algorithm is employed to work as the outer layer in the two-layers optimization procedure, since it is very well suited to deal with the few optimization variables involved in propulsion system optimization.

Several EAs have been developed at the Politecnico di Torino over the years by the research group which the author belongs.[11, 3] In the present work, the author chooses to make use of particle swarm optimization (PSO) algorithm, because, in previous optimization works on similar topic, it managed to find out really good solutions in an affordable computational time. PSO has been developed for the first time in the early 90's by Eberhart and Kennedy, mimicking the social behavior of bird flocking or fish schooling:[9, 7] a swarm, looking for food, will follow its own member that is the nearest to it, until all the swarm will reach the food.

In PSO algorithm, the members of the swarm are particles that fly through the design space and the distance from the food is the merit function of the optimization that have to be minimized to reach the optimal solutions. Positions and velocities of the particles are updated iteration by iteration while they follow the optimum one. Each particle tends to maintain its velocity, but it is subject to two pulls, toward its

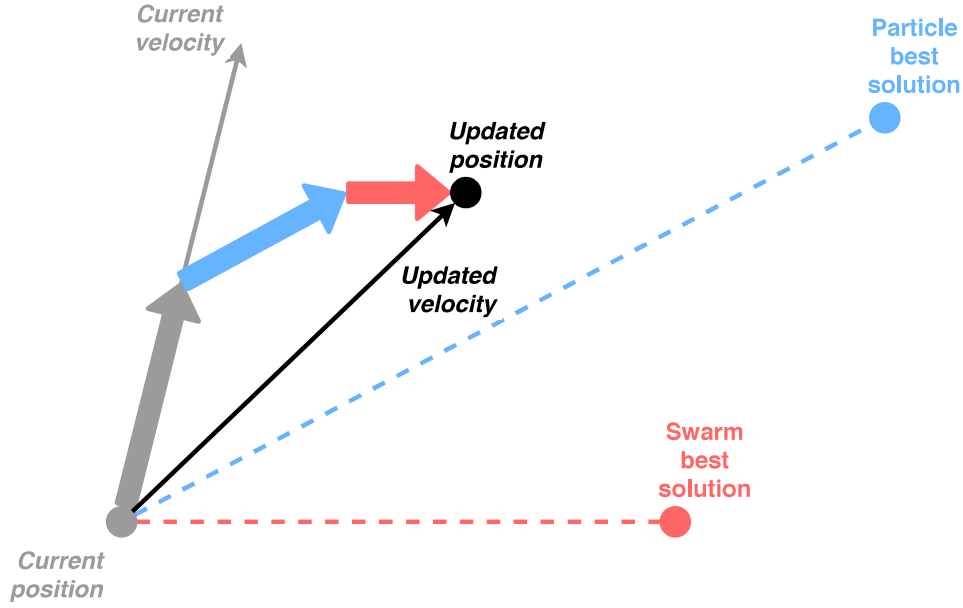


Figure 4.11: PSO algorithm visual explanation. At each iteration, the updated velocity of each particle is a linear combination of three components: particle current velocity (grey bold arrow), particle pull toward the position of the best solution it found out until that iteration (light blue bold arrow) and particle pull toward the position of the best solution the swarm found out (red bold arrow). The relative magnitude of these three components is a function of both the learning factor of the algorithm and of randomly generated quantities.

best individual solution found out until the previous iteration (here called cognitive acceleration) and toward the best solution found out by the entire population (here called social acceleration). Particle velocity and position are updated by means of Eq.(4.4) and (4.5), where v_i and v_{i+1} are particle velocities at the i -th and $i + 1$ -th iterations, X_i and X_{i+1} are particle positions (i.e. variables values) at the i -th and $i + 1$ -th iterations, $X_{Prt,best}$ is the current position of particle best solution and $X_{S,best}$ is the current position of the swarm best solution. $RAND_1$ and $RAND_2$ are random numbers in $[0,1]$ interval, whereas C_1 and C_2 are the learning factors of the algorithm whose role is to mediate particles trends toward their best solution vs. swarm best one, usually one has $C_1 = C_2 = 2$. In the present PSO algorithm the Trelea II strategy has been adopted, thus $\phi = \phi(C_1, C_2)$.^[13] Particle maximum velocity is limited by a fixed value to grant both exploration and exploitation of the whole design space.

$$v_{i+1} = \phi \cdot v_i + C_1 \cdot RAND_1 \cdot (X_{Prt,best} - X_i) + C_2 \cdot RAND_2 \cdot (X_{S,best} - X_i) \quad (4.4)$$

$$X_{i+1} = X_i + v_{i+1} \quad (4.5)$$

PSO algorithm implementation is simpler than others EAs because no operators,

such as crossover or mutation ones, have to be employed. Particles have memory of previous solutions, that is beneficial to algorithm performance. PSO information sharing mechanism is also peculiar, since the position of $X_{S,best}$ only is shared among all particles in a one-way communication. Usually, PSO algorithm uses the reaching of a maximum number of iterations or a minimum error requirements as stopping criterion.

In this Chapter, the main features of the robust-based optimization procedure have been presented and described from a theoretical point of view by the author, also providing some simple numerical examples. On the other hand, Chapter 5 and Chapter 6 will present real world applications, in the context of the optimization problem of hybrid propulsion systems, of the developed robust-based procedure.

References

- [1] George EP Box and Donald W Behnken. “Some new three level designs for the study of quantitative variables”. In: *Technometrics* 2.4 (1960), pp. 455–475.
- [2] Francesca Campolongo, Jessica Cariboni, and Andrea Saltelli. “An effective screening design for sensitivity analysis of large models”. In: *Environmental modelling & software* 22.10 (2007), pp. 1509–1518.
- [3] L Casalino, F Masseni, and D Pastrone. “Robust Design Approaches for Hybrid Rocket Upper Stage”. In: *Journal of Aerospace Engineering* 32.6 (2019), p. 04019087.
- [4] Lorenzo Casalino, Guido Colasurdo, and Dario Pastrone. “Optimal low-thrust escape trajectories using gravity assist”. In: *Journal of Guidance, Control, and Dynamics* 22.5 (1999), pp. 637–642.
- [5] Lorenzo Casalino and Dario Pastrone. “Optimal design and control of hybrid rockets for access to space”. In: *41st AIAA/ASME/SAE/ASEE Joint Propulsion Conference & Exhibit*. 2005, p. 3547.
- [6] Marco Cavazzuti. “Design of experiments”. In: *Optimization methods*. Springer, 2013, pp. 13–42.
- [7] Russell Eberhart and James Kennedy. “A new optimizer using particle swarm theory”. In: *MHS’95. Proceedings of the Sixth International Symposium on Micro Machine and Human Science*. Ieee. 1995, pp. 39–43.
- [8] Bertrand Iooss and Paul Lematre. “A review on global sensitivity analysis methods”. In: *Uncertainty management in simulation-optimization of complex systems*. Springer, 2015, pp. 101–122.

REFERENCES

- [9] J Kennedy and R Eberhart. “Particle swarm optimization”. In: *Proceedings of ICNN'95-International Conference on Neural Networks*. Vol. 4. IEEE, pp. 1942–1948.
- [10] Max D Morris. “Factorial sampling plans for preliminary computational experiments”. In: *Technometrics* 33.2 (1991), pp. 161–174.
- [11] Matteo Rosa Sentinella and Lorenzo Casalino. “Hybrid evolutionary algorithm for the optimization of interplanetary trajectories”. In: *Journal of Spacecraft and Rockets* 46.2 (2009), pp. 365–372.
- [12] Genichi Taguchi. *Robust engineering*. Vol. 224.
- [13] Ioan Cristian Trelea. “The particle swarm optimization algorithm: convergence analysis and parameter selection”. In: *Information processing letters* 85.6 (2003), pp. 317–325.

Chapter 5

Real World Application: Hybrid Powered Upper Stage

The Vega program arises in the early 1990s aiming at extending Ariane family through the development of a small launcher, based on the available solid booster know-how. Present Vega launch vehicle has four stages. First, second and third stage employs solid propellants whereas the fourth stage is liquid-powered because precise throttling and re-ignition capabilities are mandatory to perform orbital maneuvers. Typical Vega missions concern payload insertion into Sun-synchronous orbits, polar circular orbits and generic inclination orbits.[1]

Nowadays, the future replacement for the Vega launcher, namely the Vega-E, is at its early design phases and will be put into operation starting in 2024. A newly developed LRE, called M10, will employ LOX and liquid methane as propellants and will be used as the upper stage in an innovative three-stage architecture. The M10 engine is the results of an European joint venture of industries, led by Italy, from Belgium, Czech republic, Switzerland, France, Austria and Romania. The engine will have high throttling capabilities, allowing for multiple satellites/multiple orbits missions at an affordable cost.[2]

In the present work, an alternative to M10 engine will be presented: a hybrid rocket engine suitable for the replacement of Vega launcher third and fourth stage. In section 5.1 actual Vega configuration will be summarized. Then, details about engine model, ascent trajectory optimization and robust model will be presented respectively in Section 5.2, 5.3 and 5.4. In the end, Sections 5.5 and 5.6 will report numerical results and conclusions about the considered HRE application.

5.1 Case Study

Vega Launch Vehicle (VLV) current configuration is composed by three SRM powered stages, called P80, Zerfiro 23 (Z23) and Zerfiro 9 (Z9) with the addition of a

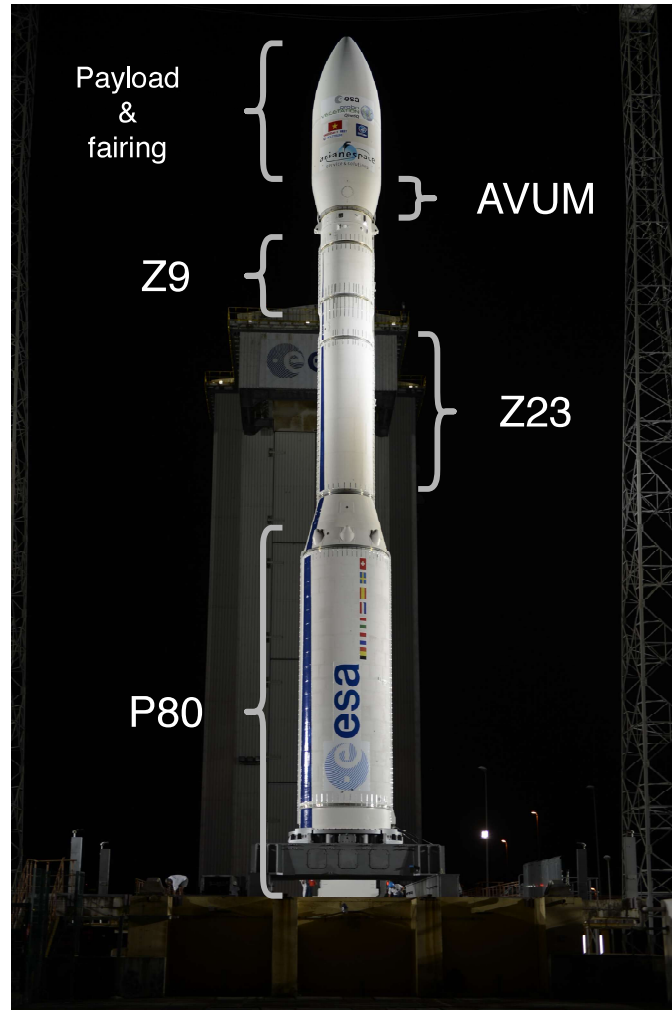


Figure 5.1: Vega Launch Vehicle and staging: P80, Z23, Z9 and AVUM.

small LRE powered Attitude Vernier Upper Module (AVUM). The whole launcher height is 30 m and the maximum diameter is 3 m. First and second stage designs and operations are not considered in the present work, whereas a single HRE powered stage is proposed for the replacement of both Z9 and AVUM stages, since hybrid architecture can grant both high performance and fine thrust control. Z9 and AVUM main features are reported in Tab. 5.1.[1]

Actual Vega upper stages total mass is given by the sum of Z9 gross mass, AVUM gross mass, payload mass and fairing mass, and is equal to 15235 kg. In this Thesis a slightly different initial mass (14522 kg) has been considered in the robust design of the hybrid upper stage, based on previous launcher specifications and used in optimization works of the whole 3-stage launcher, to grant consistency and coherence with older in-house results.[8] Engine design and trajectory are optimized

Table 5.1: Z9 and AVUM main features.

		Z9	AVUM
Diameter	m	1.90	2.18
Height	m	4.12	2.04
Gross mass	kg	12000	1265
Engine dry mass	kg	1433	688
Propellants mass	kg	10567	577
Propellants	-	HTPB 1912	NTO/UDMH
Vacuum thrust	kN	317	2.45
Vacuum specific impulse	s	295.9	314.6
Burn time	s	119.6	612.5

aiming at the maximization of the payload mass inserted in an assigned orbit. In the present work, payload delivery into a 700 km circular polar orbit is considered by the author as reference mission taking into account a launch from the Guiana Space Center. The current VLV payload for such a mission is equal to 1430 kg including payload adapter. Mass normalized ratios for the current Z9 and AVUM stages combined, performing the considered mission, are $\frac{m_u}{m_i} = 0.094$, $\frac{m_P}{m_i} = 0.731$ and $\frac{m_P}{m_P+m_{dry}} = 0.840$. In the following Sections, first engine and trajectory optimization procedures will be described, then robust-based approaches will be explained and, in the end, HRE optimal designs will be presented.

5.2 Hybrid Rocket Engine Model

The choice of propellants combination is crucial in the development of any rocket propulsion system because it has a major impact on engine overall performance and thus on mission accomplishment. In the present application Liquid OXYgen (LOX) and a paraffin-based wax are considered, respectively, as oxidizer and fuel. This propellant combination showed a peculiar combustion mechanism during experimental testing. An unstable liquid melting layer is generated at solid fuel surface, due to combustion heat transfer, causing the entrainment of liquified fuel droplets into outer gas stream. The entrainment causes a significant rise in mass transfer rate of the fuel into actual flame zone and therefore an increase in overall fuel regression rate.[7] Higher regression rate of paraffin-based wax is noteworthy because allows for a single circular port grain design. The use of classical fuels would require a more complex multi-port grain to avoid excessive grain and stage length-to-diameter ratio.[21, 22]

Circular port geometry is determined by three design parameters: grain outer radius R_g , web thickness w and grain length L_b , as reported in Fig.5.2. The initial

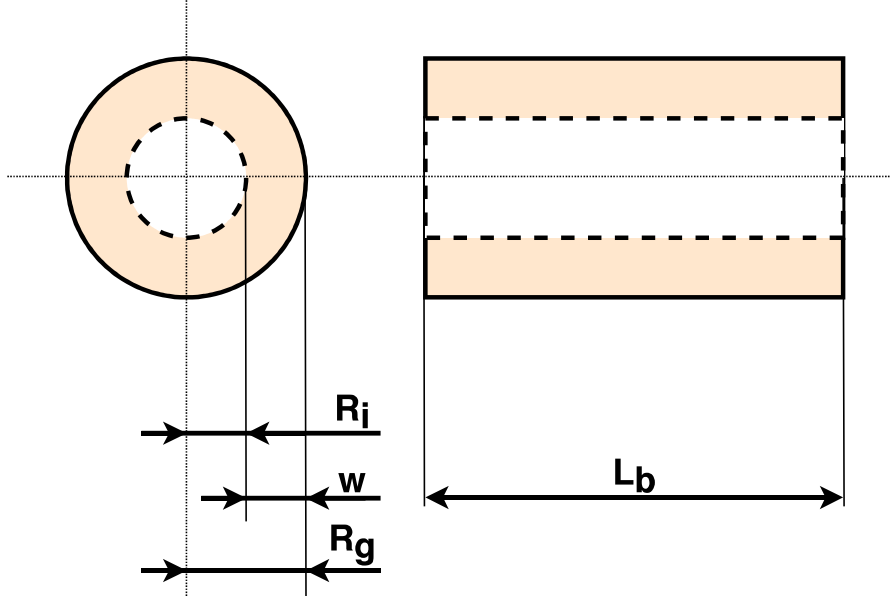


Figure 5.2: Grain geometry (not to scale). The injection of the oxidizer is axial, causing the majority of the combustion to occur inside the grain port. Grain lateral ends are affected by the combustion too, albeit having a far smaller regression rate.

grain inner radius is $R_i = R_g - w$ and thus initial port area is $(A_p)_i = \pi R_i^2$. The evolution of port area and burning perimeter, during engine operation, is described by means of Eq.(5.1), Eq.(5.2) and Eq.(5.3), where y refers to the burning distance.

$$A_p = \pi (R_i + y)^2 \quad (5.1)$$

$$P = 2\pi (R_i + y) \quad (5.2)$$

$$0 \leq y \leq w \quad (5.3)$$

Pressure losses inside the combustion chamber are taken into account by means of an approximate relation: chamber head-end pressure p_1 is written as a function of nozzle-stagnation pressure p_c using Eq.(5.4), where A_{th} is the nozzle throat area.[4]

$$p_1 = \left[1 + 0.2 \left(\frac{A_{th}}{A_p} \right)^2 \right] p_c \quad (5.4)$$

According to Marxman et al.'s theory about fuel regression rate in HRE, two opposing effects are present: total mass flux increases with axial position due to additional fuel gasification and, at the same time, the negative dependence of regression rate on axial position reduces its value.[19] Thus, fuel regression rate \dot{y} is assumed to be uniform along the grain port axis. Then \dot{y} is determined by oxidizer mass flow rate \dot{m}_O and port area A_p employing the semi-empirical correlation reported in Eq.(5.5). Nominal values for regression rate coefficient and exponent are

respectively $a = 9.1 \cdot 10^{-5} \text{ m}^{2n+1} \text{ s}^{n-1} \text{ kg}^{-n}$ and $n = 0.69$, when the International System of Units is used.[18]

$$\dot{y} = a (\dot{m}_O/A_p)^n \quad (5.5)$$

Cryogenic LOX is stored inside a tank in liquid state. During engine burn, oxidizer flow rate \dot{m}_O is maintained by the pressure difference between oxidizer tank pressure p_t and chamber head-end pressure p_1 . Assuming incompressible turbulent flow, \dot{m}_O can be computed by means of Eq.(5.6) where Z indicates the hydraulic resistance in the oxidizer flow path, from tank to combustion chamber. Hydraulic resistance is assumed to be a constant throughout engine burn and it is calculated to have $\frac{p_t}{p_c} = 2.5$ at HRE ignition, in nominal conditions.

$$\dot{m}_O = \sqrt{(p_t - p_1)/Z} \quad (5.6)$$

Fuel mass flow \dot{m}_F is given by the product of fuel density ρ_F , regression rate \dot{y} and burning area $A_b = L_b P$ as reported in Eq.(5.7). The contribution of lateral end to combustion $\left(\frac{A_{le}}{A_b}\right)_{\%}$ is here neglected and will be checked a posteriori by means of Eq.(5.8). Equation(5.9) shows the relation between mixture ratio $\alpha = \dot{m}_O/\dot{m}_F$ and grain geometry. A_p^n/A_b is usually a function of time during HRE burn. Thus, the mixture ratio changes even if \dot{m}_O is kept constant. This mechanism is a distinctive feature of hybrids and it is known as mixture-ratio shifting.

$$\dot{m}_F = \rho_F \dot{y} A_b = \rho_F \dot{y} L_b P \quad (5.7)$$

$$\left(\frac{A_{le}}{A_b}\right)_{\%} = \frac{(R_i + R_g)w}{2R_i L_b} \cdot 100 \quad (5.8)$$

$$\alpha = \frac{\dot{m}_O}{\dot{m}_F} \propto \dot{m}_O^{1-n} A_p^n / A_b \quad (5.9)$$

Total propellants mass flow $\dot{m}_P = \dot{m}_O + \dot{m}_F$, chamber pressure p_c and nozzle throat area A_{th} are put in relation by means of the characteristic velocity c^* , assuming an isentropic expansion in the nozzle, as shown in Eq.(5.10). In general, propellants performance are function of mixture ratio α and chamber pressure p_c . Actual pressure range of variation is wide during engine burn, but its effect on propellants performance is far smaller than mixture ratio one. Thus, $p_c = 10^6 \text{ Pa} = \text{constant}$ is used and propellants performance are evaluated varying only the mixture ratio α .

$$p_c = \frac{(\dot{m}_O + \dot{m}_F)c^*}{A_{th}} \quad (5.10)$$

Frozen equilibrium expansion is adopted: chemical composition of exhausted gas is fixed throughout nozzle expansion and equal to combustion chamber one. The underestimation of actual rocket performance, due to the assumed frozen equilibrium expansion, ranges from 1% to 4%, resulting in conservative solutions.

Moreover, a c^* -efficiency, equal to 96% in nominal condition, is considered in the engine model.[23] Accurate and quick estimations of the proper values for characteristic velocity c^* and specific heat ratio γ have to be performed as the mixture ratio shifts during engine operation. Thus, third-degree polynomial curves, fitting c^* and γ values for LOX/wax, are embedded in the code.[20]

In previous works at Politecnico di Torino, gas pressurized and electrical feeding systems have been studied and their performance has been compared.[13, 14, 15, 12] In the present test case, a partially regulated feed system is considered and two operational modes are employed: constant tank pressure and a subsequent blow-down phases. During the first operational mode, the pressure level in the oxidizer tank is kept constant by a helium flow from an auxiliary tank to the oxidizer tank. In nominal conditions, 3% of the total oxidizer tank volume is earmarked for the initial ullage volume V_{ull} , granting a sufficiently regular response when engine burn starts.[6] In consequence, the amount of pressurizing gas inside the oxidizer tank, before engine ignition, is equal to the initial ullage volume, i.e. $(V_g)_i = V_{ull}$. An initial pressurizing gas pressure in the auxiliary tank $p_a = 2.5 \cdot 10^7$ is employed in nominal condition. Pressure levels in the oxidizer tank are evaluated by means of Eq.(5.11) and Eq.(5.12), respectively for the constant tank pressure and the subsequent blow-down phase. The pressure drop in the blow-down phase is calculated assuming an isentropic expansion of the helium located in the oxidizer tank.

$$p_t = (p_t)_i = 2.5 \cdot 10^6 \text{ Pa} \quad (5.11)$$

$$p_t = (p_t)_i \left[\frac{(V_g)_{BD}}{V_g} \right]^{\gamma_g} = (p_t)_i \left[\frac{(V_g)_i + \frac{(m_O)_{BD}}{\rho_O}}{(V_g)_i + \frac{m_O}{\rho_O}} \right]^{\gamma_g} \quad (5.12)$$

In Eq.(5.12) m_O is the generic oxidizer mass exhausted, γ_g is helium specific heat ratio and ρ_O is LOX density. The relative durations of the two operational modes are determined by the oxidizer mass exhausted until the beginning of the blow-down phase $(m_O)_{BD}$ (i.e. by the amount of oxidizer exhausted during the previous constant pressure phase) and by the total oxidizer mass exhausted $(m_O)_f$. Thus $(m_O)_{BD}$ and $(m_O)_f$ are the fourth and fifth engine model design parameters.

Thrust coefficient C_F is evaluated, by means of Eq.(5.13), considering an isentropic expansion from chamber pressure p_c to exit pressure p_e , constant heat ratio γ equal to combustion chamber one and nozzle area ratio E . Moreover, an η_{C_F} correction factor, equal to 98% in nominal conditions, is employed to modify the vacuum thrust coefficient of the considered 1-D isentropic expansion. One can notice that the term $E \frac{p_0}{p_c}$ is directly proportional to the atmospheric static pressure p_0 , that is always small in the present test case because the upper stage flies at

sufficiently high altitude.

$$C_F = \eta_{C_F} \left\{ \sqrt{\frac{2\gamma^2}{\gamma-1} \left(\frac{2}{\gamma+1}\right)^{\frac{\gamma+1}{\gamma-1}} \left[1 - \left(\frac{p_e}{p_c}\right)^{\frac{\gamma-1}{\gamma}}\right]} + E \frac{p_e}{p_c} \right\} - E \frac{p_0}{p_c} \quad (5.13)$$

Initial propellants mass flow rate $(\dot{m}_P)_i$ at engine ignition (i.e. at $t = 0$ s) is calculated by means of Eq.(5.14), where α_i is the initial mixture ratio and $(\dot{m}_O)_i$ is the oxidizer mass flow at ignition. Once $(\dot{m}_P)_i$ is known, initial nozzle throat area $(A_{th})_i$ and initial fuel grain port area $(A_p)_i$ are computed thanks to Eq.(5.15) and Eq.(5.16), respectively. The nominal value of the initial throat-to-port area ratio is $J = 0.5$.

$$(\dot{m}_P)_i = (1 + \alpha_i)(\dot{m}_F)_i = \frac{1 + \alpha_i}{\alpha_i}(\dot{m}_O)_i \quad (5.14)$$

$$(A_{th})_i = \frac{(\dot{m}_P)_i}{(p_c)_i c_i^*} \quad (5.15)$$

$$(A_p)_i = \frac{(A_{th})_i}{J} \quad (5.16)$$

The initial nozzle area ratio E_i is the sixth (and last) design parameter required to define HRE performance. Nevertheless, during engine burn, nozzle area ratio E may vary due to erosion effects. In the present model, the author neglect erosion along the nozzle and employed Bartz's method to relate throat erosion rate \dot{s} to throat radius R_{th} and combustion chamber pressure p_c , as shown in Eq.(5.17).[10, 17]

$$\dot{s} = \dot{s}_{ref} \left(\frac{p_c}{p_{c,ref}}\right)^{0.8} \left(\frac{R_{th,ref}}{R_{th}}\right)^{0.2} \quad (5.17)$$

Computational Fluid Dynamics (CFD) analysis on the ablation of carbon/carbon nozzle, used in LOX/wax-powered HRE, suggest a reference value for throat erosion rate $\dot{s}_{ref} = 0.1$ mm/s.[5] The integration of Eq.(5.17) allows for a proper computation of R_{th} and E during HRE burn. The presence of the eroded mass is neglected in rocket performance evaluation, thus thrust augmentation or rocket mass reduction are not taken into account in the present model.

Total initial stage mass m_i is given by the sum of payload mass m_u , engine dry mass m_{dry} , propellants mass $m_P = m_F + m_O$ and fairing mass $m_{fairing}$ (that is given, see Sec.5.3), as shown in Eq.(5.12). Grain outer radius R_g , web thickness w , grain length L_b and fuel density ρ_F allows for fuel mass determination through Eq.(5.19). Total oxidizer mass m_O is equal to $(m_O)_f$ that is an engine design parameter.

$$m_i = m_u + m_{dry} + m_P + m_{fairing} = m_u + m_{dry} + m_F + m_O + m_{fairing} \quad (5.18)$$

$$m_F = \rho_F L_b A_b = \rho_F L_b \pi (R_g^2 - R_i^2) = \rho_F L_b \pi (2R_g w - w^2) \quad (5.19)$$

Engine dry mass is in turn equal to the sum of engine components masses and propellant sliver mass: combustion chamber mass m_{cc} , oxidizer tank mass m_t , nozzle mass m_{nz} , engine case mass m_{case} , auxiliary tank mass m_a , pressurizing gas mass m_g and propellant sliver mass m_{sl} . The masses of the feeding system parts, such as valves and plumbings, are here neglected. Moreover, for circular port grain design in nominal condition, propellant sliver is not present at the end of the engine burn, thus $m_{sl} = 0$. Equation(5.20) summarizes significant contributions to engine dry mass.

$$m_{dry} = m_{cc} + m_t + m_{nz} + m_{case} + m_a + m_g \quad (5.20)$$

Engine components masses are computed using a suitable set of assumptions and proper approximations. Combustion chamber consists of a thin wall hollow cylinder and it is insulated by a 6 mm liner (the density of the liner is considered equal to ρ_F). Outer diameter of Vega's third stage fixes cylindrical oxidizer tank diameter to 1.9 m. Pressurizing Helium is contained in a spherical auxiliary tank. Helium mass and auxiliary tank volume are known once engine design is fixed. A 1.25 safety factor is assumed in wall thickness computation for combustion chamber, oxidizer tank and auxiliary tank to withstand internal pressures during HRE burn. Moreover, a 1-mm-thick cylindrical casing, that encapsulates the whole engine, is considered. Aluminum, with a density equal to ρ_{Al} , is employed for combustion chamber, oxidizer tank, auxiliary tank and engine casing. An ablative layer (with density equal to ρ_{abl}) protects a 45 deg convergent and 20 deg divergent nozzle.[3] Nozzle structural mass is neglected in the mass budget because it is far smaller than ablative layer mass.

In the end, engine design is determined by six parameters: grain outer radius R_g , web thickness w , grain length L_b , oxidizer mass exhausted until the beginning of blow-down phase $(m_O)_{BD}$, total oxidizer mass exhausted $(m_O)_f$ and initial nozzle area ratio E_i . Once engine design is determined (i.e. payload is given), an indirect trajectory optimization is performed aiming at the maximization of the orbit insertion altitude. Trajectory optimization approach will be discussed in Section 5.3.

On the other hand, seventeen input parameters play a role in the engine model: reference throat erosion rate \dot{s}_{ref} , reference chamber pressure $p_{c,ref}$, reference throat radius $R_{th,ref}$, regression rate coefficient a , regression rate exponent n , aluminum density ρ_{Al} , ablative density ρ_{abl} , fuel density ρ_F , oxidizer density ρ_O , pressurizing gas temperature T_g , liner thickness s_{lin} , combustion chamber wall thickness s_{cc} , initial throat area-to-port area ratio J , initial tank pressure $(p_t)_i$, ullage volume V_{ull} , thrust coefficient correction η_{CF} and c^* -efficiency η_{c^*} . In Section 5.4 the model response to this set of input parameters will be discussed.

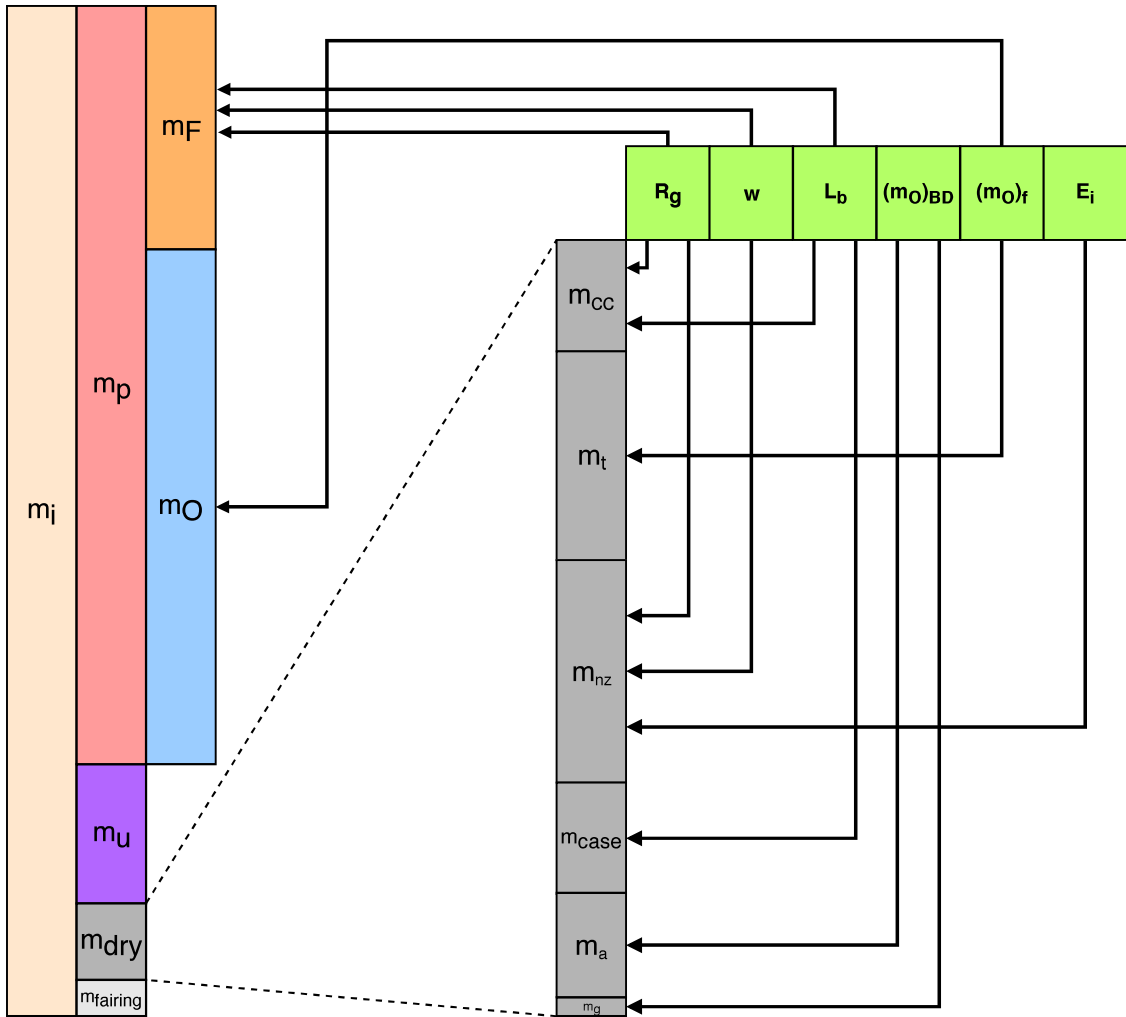


Figure 5.3: Mass budget scheme. Arrows represent the functional relationships between design parameters (green boxes) and masses. m_i and $m_{fairing}$ are assigned (see Sec.5.3). The scheme is approximately scaled to the mass budget of robust solutions presented in Sec.5.5.

5.3 Ascent Trajectory

Ascent trajectory is optimized by means of an indirect procedure, which is based on the Optimal Control Theory (OCT). The procedure has been widely used in the Politecnico di Torino since the early 90's for space trajectory and mission optimization.[9, 13] The spacecraft is considered as a point mass and its state equations are written in a vectorial form in Eq.(5.21) providing the time derivative of position \mathbf{r} , velocity \mathbf{v} and mass M . The position components are radius, latitude and longitude whereas velocity components are in the radial, eastward and northward directions.

Earth mass M_{\oplus} and the gravitational constant G_N defines the inverse-square gravity field as shown in Eq.(5.22). Equation(5.23) reports the aerodynamic drag as a function of the relative velocity $\mathbf{v}_{rel} = \mathbf{v} - \boldsymbol{\omega} \times \mathbf{r}$, where $\boldsymbol{\omega}$ is Earth’s angular velocity. An interpolation of the standard atmosphere gives the atmospheric density ρ_{atm} as a function of the rocket altitude during the ascent trajectory.

$$\frac{d\mathbf{r}}{dt} = \mathbf{v} \quad \frac{d\mathbf{v}}{dt} = \mathbf{g} + \frac{\mathbf{F} - \mathbf{D}}{m} \quad \frac{dM}{dt} = -\frac{|\mathbf{F}|}{c^*C_F} \quad (5.21)$$

$$\mathbf{g} = -\frac{G_N M_{\oplus}}{\|\mathbf{r}^3\|} \mathbf{r} \quad (5.22)$$

$$D = \frac{1}{2} \rho_{atm} C_D S v_{rel}^2 \quad (5.23)$$

A non-dimensional form is employed to rewrite the equation of motion, enhancing the accuracy of the numerical integration. Five arcs, in which the control law is homogeneous, model the trajectory: first burn at constant-pressure with fairing (1), first burn at constant-pressure without fairing (2), first burn blow-down (3), coasting (4) and second burn (5). The performance of the first and second stage of the Vega launcher are given, consistent with a launch from Kourou, in the French Guiana. Exhausted masses and HRE ignition condition are known in nominal conditions: altitude $h = 86.88$ km, latitude $\Phi = 9.11$ deg, radial velocity component $u_r = 0.142$ km/s, velocity in the eastward direction $v_e = 0.230$ km/s, velocity in the northward direction $w_n = 4.146$ km/s, hybrid stage overall initial mass 14,522 kg and payload fairing mass 535 kg.

An adjoint variable is introduced for each equation of the set presented in (5.21). The Euler-Lagrange equations for the adjoint variables, the algebraic equations for the control variables and the boundary condition for optimality are provided by the OCT. A Newton’s method-based procedure is employed to solve the multi-point Boundary Value Problem (BVP) generated by the application of the OCT. First, a set of tentative values is selected for the problems unknowns and then varied to satisfy the boundary conditions.

In the present optimization work, the unknowns parameters are the time length of each arc and the initial values of five adjoint variables. The longitude-related adjoint variable is null and the mass-related one is fixed at one: the problem is homogeneous in the adjoint variables, thus they can be arbitrarily scaled. Additional problem unknowns are R_f and $(m_O)_{tot}$, i.e. the fuel grain inner radius and the overall oxidizer exhausted mass at the end of the engine burn. Dynamic pressure, heat flux and acceleration are explicitly unconstrained during the optimization. However, without explicit constraints, optimized trajectories are characterized by a deeper penetration into the atmosphere during the coasting arc. This behavior could result in extreme thermal loads, since the fairing is supposed to be jettisoned during HRE first burn. Thus, a horizontal velocity is forced, at the end of the first

burn, by an additional constraint. Analogously, an additional unknown is introduced in the optimization problem, due to the free discontinuity of the horizontal velocity at the end of the first burn. The resulting constrained-trajectories are able to grant reduced thermal loads but, typically, at the cost of a small payload penalty (roughly 10 kg).

In the end, in the indirect trajectory optimization, two additional input parameters are present: initial velocity \mathbf{v}_i and radius \mathbf{r}_i . In the following Section 5.4 the role of model input parameters, in the coupled optimization of propulsion system and trajectory, will be discussed.

5.4 Robust-based Optimization

5.4.1 Sensitivity Analysis and Parameters Screening

In Sec.5.2 hybrid rocket engine design has been detailed, whereas in the previous Sec.5.3 the main features of the indirect trajectory optimization have been summarized. In the present case, the design parameters result to be six, all involved in the design of the propulsion system. On the other hand, the input parameters of the model are nineteen: seventeen concerning engine design and two related to trajectory optimization. Thus, design parameters vector \mathbf{b} (i.e. the group of parameters that can be freely set by the designer) and the input parameter vector \mathbf{X} (i.e. the other parameters that have a role in the considered engine/trajectory model) are reported in (5.24) and (5.25).

$$\mathbf{b} = [R_g, w, L_b, (m_O)_{BD}, (m_O)_f, E_i] \quad (5.24)$$

$$\mathbf{X} = [\dot{s}_{ref}, p_{c,ref}, R_{th,ref}, a, n, \rho_{Al}, \rho_{abl}, \rho_F, \rho_O, T_g, s_{lin}, s_{cc}, J, p_{t,i}, \mathbf{v}_i, \mathbf{r}_i, V_{ull}, \eta_{CF}, \eta_{c^*}] \quad (5.25)$$

Vectors \mathbf{b} and \mathbf{X} are the input for the sensitivity analysis described in the fourth Chapter of this thesis (Sec.4.1). Lower and upper boundary vectors, \mathbf{b}_L and \mathbf{b}_U , for the design parameters are reported in Tab.5.2 whereas Tab.5.3 summarizes nominal and off-nominal values for input parameters. One can notice that \mathbf{v}_i and \mathbf{r}_i have been replaced by their normalized forms in Tab.5.3 to easily define off-nominal values: $\mathbf{v}_{i,ref}$ is the velocity vector at third stage ignition in nominal condition (detailed in Sec.5.3) and r_{\oplus} is Earth equatorial radius (i.e. Earth semi-major axis). The choice of the boundaries for \mathbf{b} defines problem design space and has been driven by application-related requirements (e.g. the maximum value for $2R_g$ is limited by the outer diameter of the third stage of the current Vega launcher) and previous know-how about the use of evolutionary algorithm (i.e. reduce parameters ranges to speed-up algorithm convergence and, at the same time, grant that optimal solutions will be on the edges of or inside the defined design space).

Table 5.2: Boundaries of the elements of \mathbf{b} .

	R_g	w	L_b	$(m_O)_f$	$(m_O)_{BD}$	E_i
	m	m	m	kg	kg	-
\mathbf{b}_L	0.55	0.25	4.3	6971	3195	15
\mathbf{b}_U	0.60	0.35	4.5	7697	3631	20

 Table 5.3: Nominal and off nominal values of the elements of \mathbf{X} .

Input parameter		Low	Nom	High	
1	\dot{s}_{ref}	m/s	$0.85 \cdot 10^{-4}$	$1 \cdot 10^{-4}$	$1.15 \cdot 10^{-4}$
2	$p_{c,ref}$	bar	9.7	10	10.3
3	$R_{th,ref}$	m	0.198	0.200	0.202
4	a	$m^{2n+1}s^{n-1}kg^{-n}$	$9.0 \cdot 10^{-5}$	$9.1 \cdot 10^{-5}$	$9.2 \cdot 10^{-5}$
5	n	-	0.68	0.69	0.70
6	ρ_{Al}	kg/m ³	2758	2800	2842
7	ρ_{abl}	kg/m ³	1724	1750	1776
8	ρ_F	kg/m ³	926	940	954
9	ρ_O	kg/m ³	1123	1140	1157
10	T_g	K	278	298	318
11	s_{lin}	m	$5.60 \cdot 10^{-3}$	$6.0 \cdot 10^{-3}$	$6.40 \cdot 10^{-3}$
12	s_{cc}	m	$4.67 \cdot 10^{-4}$	$5.00 \cdot 10^{-4}$	$5.33 \cdot 10^{-4}$
13	J	-	0.495	0.500	0.505
14	$p_{t,i}$	bar	24.25	25.00	25.75
15	$\frac{\ \mathbf{v}_i\ }{\ \mathbf{v}_{i,ref}\ }$	%	97	100	103
16	$\frac{\ \mathbf{r}_i\ }{\ \mathbf{r}_\oplus\ }$	-	1.0133	1.0136	1.0139
17	V_{ull}	%	2.85	3.00	3.15
18	η_{CF}	-	0.975	0.980	0.985
19	η_{c^*}	-	0.955	0.960	0.965

On the other hand, off-nominal values for \mathbf{X} are based on existing literature and technical considerations.[10, 18, 26, 27]

The merit function employed in the sensitivity analysis is defined in Eq.(5.26), where m_u is the stage payload, h^* the target orbit altitude (i.e. 700 km) and h the attained orbit. Φ is a linear combination of payload and altitude violation, with respect to the target one, because both a large payload mass and the ability to reach a given orbit are crucial for the mission. An ϵ -constraint approach is employed with $\epsilon = h^* = 700$ km and $k_h = 20$ kg/km.[25]

$$\Phi = m_u - k_h \max(0, h^* - h) \quad (5.26)$$

The ranges defined by $\mathbf{b}_U - \mathbf{b}_L$ are divided in one hundred finite steps for each design parameters, resulting in a 100^6 -points discretization grid. A minimum admissible altitude $h_{min} = 500$ km (i.e. a maximum altitude violation equal to 200 km) is defined. In this way, starting points that are not meaningful in the present application (i.e. leading to low insertion altitude or rocket crashes) are discarded in the sensitivity analysis. One hundred starting points (i.e. $N_{I,SA} = 100$) s.t. $h \geq h_{min}$ are randomly gathered from the discretization grid and used for the sensitivity analysis of the engine/trajectory model. Table 5.4 presents a recap of SA setup and computational cost in terms of merit function evaluations.

Table 5.4: SA settings and computational cost.

number of steps for design parameters	100
number of input parameters	19
number of starting points	100
number of repetitions	10
number of function evaluations	$100 \cdot (19 + 1) \cdot 10 = 20000$

The Morris method, detailed in Sec.4.1, is used for the sensitivity analysis. Ten repetition (i.e. the number of Morris trajectories starting from a single design point) are taken into account in the SA. Portions of Morris trajectories resulting in unfeasible solutions are neglected in the evaluation of the elementary effects. Morris indices μ_j^* and σ_j , calculated for each input parameters $j = 1, \dots, 19$, are reported in Tab.5.5.

The magnitude of μ_j^* (namely the mean of the absolute values of the j -th elementary effects) expresses the response of the merit function Φ to a variation of the j -th input parameter, whereas σ_j (namely the standard deviation, with respect to the mean value, of the j -th elementary effects) measures non-linear effects related to such variation. Morris method divides input parameters into two groups:

- Parameters with negligible or no effect on model output (i.e. $\mu_j^* \approx 0$ and $\sigma_j \approx 0$): s_{cc} , $\frac{\|\mathbf{v}_i\|}{\|\mathbf{v}_{i,ref}\|}$, $\frac{\|\mathbf{r}_i\|}{\|\mathbf{r}_{\oplus}\|}$, η_{CF} and η_{c^*} . These parameters variations can be neglected in the robust-based optimization because their effects on model output are feeble: these input parameters are constants. Their values are fixed and equal to the nominal ones reported in Tab.5.3: $s_{cc} = 0.5$ mm, $\frac{\|\mathbf{v}_i\|}{\|\mathbf{v}_{i,ref}\|} = 1$, $\frac{\|\mathbf{r}_i\|}{\|\mathbf{r}_{\oplus}\|} = 1.0136$ (i.e. third stage ignition occurs at $h = 86.88$ km), $\eta_{CF} = 0.98$ and $\eta_{c^*} = 0.96$.
- Parameters with non-linear effect on model output (i.e. both μ_j^* and σ_j are not negligible): \dot{s}_{ref} , $p_{c,ref}$, $R_{th,ref}$, a , n , ρ_{Al} , ρ_F , ρ_O , T_g , s_{lin} , J , $p_{t,i}$ and V_{ull} . The effect of these parameters on model output is strong (μ_j^* values are significant) and unpredictable (σ_j values are large). Their fluctuations

Table 5.5: Sensitivity analysis outputs: μ_j^* and σ_j .

	Input parameter	μ_j^*	σ_j
1	\dot{s}_{ref}	52.71	99.07
2	$p_{c,ref}$	42.30	79.43
3	$R_{th,ref}$	11.14	20.41
4	a	11267.57	20119.48
5	n	28938.43	43635.39
6	ρ_{Al}	699.06	699.01
7	ρ_{abl}	375.11	376.62
8	ρ_F	9054.35	12355.32
9	ρ_O	463.84	463.88
10	T_g	25.31	25.34
11	s_{lin}	95.59	95.54
12	s_{cc}	0.00	0.00
13	J	3868.66	6609.87
14	$p_{t,i}$	4006.43	6401.29
15	$\frac{\ \mathbf{v}_i\ }{\ \mathbf{v}_{i,ref}\ }$	0.00	0.01
16	$\frac{\ \mathbf{r}_i\ }{\ \mathbf{r}_{\oplus}\ }$	0.29	1.10
17	V_{ull}	8.11	8.11
18	η_{C_F}	0.01	0.02
19	η_{c^*}	0.01	0.02

must be taken into account in each merit function evaluation performed in the robust-based optimization: these input parameters are uncertain.

One can notice that Morris indices, related to nozzle throat erosion (i.e. the effects of fluctuation in \dot{s}_{ref} , $p_{c,ref}$ and $R_{th,ref}$), are small, albeit not negligible. In order to reduce the number of uncertain parameters (and consequently the computational cost of the optimization) but preserve the uncertainties in nozzle throat erosion phenomenon, the author defines a synthetic uncertain parameter K_{ero} , reported in Eq.(5.27). The rate of throat erosion \dot{s} , according to Eq.(5.17), can be written as a function of K_{ero} as shown in Eq.(5.28). Off-nominal values of K_{ero} are the highest and the lowest possible ones due to \dot{s}_{ref} , $p_{c,ref}$ and $R_{th,ref}$ variation, according to Eq.(5.27).

$$K_{ero} = \dot{s}_{ref} \cdot R_{th,ref}^{0.2} / p_{c,ref}^{0.8} \quad (5.27)$$

$$\dot{s} = K_{ero} \frac{p_c^{0.8}}{R_{th}^{0.2}} \quad (5.28)$$

Moreover, looking at Tab.5.5, one can observe that some parameters, classified as uncertain by Morris method, exhibits a peculiar feature: $\mu_j^* \approx \sigma_j \neq 0$. These

parameters are ρ_{Al} , ρ_{abl} , ρ_O , T_g , s_{lin} and V_{ull} . It is noteworthy that μ_j^* is defined as the mean of the absolute values of the j -th elementary effects, whereas σ_j is the standard deviation with respect to their mean value, that is calculated without modulus operator. Thus, the condition $\mu_j^* \approx \sigma_j \neq 0$ means that the j -th parameter has an effect on model outputs that can be positive or negative (i.e. $\mu_j^* \neq 0$), different in magnitude from a design point to an other (i.e. $\sigma_j \neq 0$) but null on average when arithmetic mean is used. For example, ρ_{Al} determines payload mass being involved in engine dry mass computation. When off-nominal values are taken into account the resulting payload mass, and thus the resulting merit function, increases or decreases of the same amount, due to heavier or lighter propulsion system, because off-nominal values of input parameters are symmetrical around nominal ones. A change in the design parameters, for example a longer fuel grain, results in a heavier engine casing and merit function increase and decrease due to ρ_{Al} variations are again equal, but their magnitude is different from the previous design point, because engine geometry is changed.

Thus the effect of ρ_{Al} on model output is not linear (depends on the design point) but it is predictable. Moreover, in robust-based optimization, average performance are considered and the mean effect of these parameters variation is null (or negligible). The author choses to keep out ρ_{Al} , ρ_{abl} , ρ_O , T_g , s_{lin} and V_{ull} from the group of uncertain parameters involved in the robust-based optimization to further improve computational speed. Their off-nominal behavior will be checked "a posteriori" only for the optimized design points found out. In the end, the constant vector \mathbf{K} , the uncertain parameter vector \mathbf{p} and the "a posteriori" uncertain parameter vector \mathbf{p}_p are defined as:

$$\mathbf{K} = [s_{cc}, \mathbf{v}_i, \mathbf{r}_i, \eta_{CF}, \eta_{c^*}] \quad (5.29)$$

$$\mathbf{p} = [K_{ero}, a, n, \rho_F, p_{t,i}, J] \quad (5.30)$$

$$\mathbf{p}_p = [\rho_{Al}, \rho_{abl}, \rho_O, T_g, s_{lin}, V_{ull}] \quad (5.31)$$

5.4.2 Design of Experiments

After vectors \mathbf{b} and \mathbf{p} have been defined, the robust-based optimization problem can be formally cast in (5.32), where \mathbf{z}^p expresses the noise (i.e. the uncertainties) that affects the elements of \mathbf{p} and $g(\mathbf{b}, \mathbf{p} + \mathbf{z}^p) \leq 0$ the set of inequality constraints of the optimization problem.

$$\begin{aligned} &\text{find} && \mathbf{b} \in \mathbb{R}^n \\ &\text{to maximize} && \Phi_{avg}(\mathbf{b}, \mathbf{p}) \\ &\text{subject to} && g_j(\mathbf{b}, \mathbf{p} + \mathbf{z}^p) \leq 0, j = 1, \dots, r \\ &\text{and to} && \mathbf{b}_L \leq \mathbf{b} \leq \mathbf{b}_U \end{aligned} \quad (5.32)$$

In the same way as previously done in the SA, three levels are assigned to each uncertain parameter of \mathbf{p} : lower than nominal, nominal and higher than nominal. For each design point defined by vector \mathbf{b} , several combinations of the uncertain parameters of \mathbf{p} are considered in the computation of an average merit function Φ_{avg} , according to a proper DOE technique. One can notice that both \mathbf{p} and \mathbf{p}_p contain six parameters, thus the same design of experiment technique can be employed in the robust-based optimization and in the subsequent "a posteriori" performance verification. Attained orbit altitude h_i and payload $m_{u,i}$ are determined for each i -th combination prescribed by the DOE technique and average performance are obtained by means of Eq.(5.33). P_i is the probability function of the i -th uncertain parameters combination calculated as reported in Eq.(5.34), where $p_j = 0.5$ if the j -th level is equal to 2 (i.e. the nominal value is taken into account for the j -th element of \mathbf{p}), $p_j = 0.25$ if the j -th level is equal to 1 or 3 (i.e. off-nominal values are considered) and $p_{tot} = \sum_{ij} p_j$ for $j = 1, \dots, 6$ (i.e. $\sum_i P_i = 1$).

$$\Phi_{avg} = \sum_i P_i \Phi_i \quad (5.33)$$

$$P_i = \frac{\sum_j p_j}{p_{tot}} \quad (5.34)$$

The i -th contribution Φ_i to the optimization merit function Φ_{avg} is computed as a linear combination of $m_{u,i}$ and h_i analogously to what done in the SA (see Eq.(5.26):

$$\Phi_i = m_{u,i} - k_h \max(0, h^* - h_i) \quad (5.35)$$

In Eq.(5.35) $k_h = 20$ kg/km to nullify the average altitude violation and $h^* = 700$ km, chosen to grant the highest performance in terms of robustness. Average violation Δ_{avg} and payload mass $m_{u,avg}$ can be computed by means of Eq.(5.36) and (5.37).

$$\Delta_{avg} = \sum_i P_i \Delta_i \quad (5.36)$$

$$m_{u,avg} = \sum_i P_i m_{u,i} \quad (5.37)$$

The proper sets of uncertain parameters combinations are prescribed by DOE techniques. Details about DOE theory has been given in Sec.4.2. As aforementioned, uncertain parameters combinations are coded in three levels and six uncertain parameters are present. The combinations of uncertain parameters are encoded, thanks to levels discretization, in experimental arrays. In the present case, the author employs only Fractional Factorial Design (FFD) to reduce the computational cost of the robust-based optimization. Three different FFD are employed and here listed by means of the corresponding experimental arrays:

1. the first, and smallest, array used is here called F_{12} . In this array only one parameter at a time presents an off-nominal value. The number of experimental tests is equal to twice the number of uncertain parameters. The idea behind F_{12} is to evaluate, through the comparison with the other arrays, the actual impact of multi-parameter fluctuations and to determine whether the additional experimental runs required are worthy or not. Table 5.6 shows the levels combinations prescribed by F_{12} ;
2. the second experimental array is called L_{18} and it is borrowed directly from Taguchi's theory about robust design. L_{18} is the smallest orthogonal array suitable to deal with six parameters discretized in three levels.[24] Table 5.7 presents Taguchi's L_{18} array. One can notice that the first row of L_{18} represents an off-nominal condition in which all the uncertain parameters assume the lowest value. This experimental run is neglected by the other FFD and, as will be showed in the results section, it is particularly demanding in terms of launcher performance degradation;
3. the third, and last, experimental array used is based on Box-Behnken's works and it is here called B_{48} array.[16] This array is the biggest one considered in the present work, and prescribes the execution of 48 experimental runs. The comparison between B_{48} and Taguchi's L_{18} , that is definitely smaller (i.e. the computation will be considerably faster), aims at finding out whether the additional experimental runs, required by Box-Behnken's method, are effective or not.

One additional parameters combination is added to these arrays in which all levels are equal to 2, i.e. all nominal values are considered in the merit function evaluation. This combination can be regarded as the center point of the uncertainties distribution and it is useful to compute in detail the reference launcher performance, given the design parameter set (i.e. given the vector \mathbf{b}) throughout the optimization. For this reason the actual number of experimental runs performed is 13, 19 and 49 when F_{12} , L_{18} and B_{48} arrays are respectively used.

In the robust-based optimization, a particle swarm optimization (PSO) algorithm leads the selection of tentative values for \mathbf{b} . PSO belongs to the class of evolutionary algorithms and mimics the motion typical of flocks of bird or school of fish. Details about PSO features can be found in Sec. 4.3. The setup of the PSO, used in the present application, is presented in Tab.5.9 and it is based on a previous work of the author on the same topic.[11] The number of generation $N_G = 1000$ has been chosen to ensure convergence of the optimization algorithm to the global optimal solutions. Table 5.10 compares the computational costs, in terms of Φ_i evaluation, for optimization runs employing F_{12} , L_{18} and B_{48} arrays. For the sake of clarity, also the computational cost of the SA is reported. One can

Table 5.6: F_{12} array.

1	2	2	2	2	2
3	2	2	2	2	2
2	1	2	2	2	2
2	3	2	2	2	2
2	2	1	2	2	2
2	2	3	2	2	2
2	2	2	1	2	2
2	2	2	3	2	2
2	2	2	2	1	2
2	2	2	2	3	2
2	2	2	2	2	1
2	2	2	2	2	3

Table 5.7: Taguchi's L_{18} array.

1	1	1	1	1	1
1	2	2	2	2	2
1	3	3	3	3	3
2	1	1	2	3	3
2	2	2	3	1	1
2	3	3	1	2	2
3	1	2	3	2	3
3	2	3	1	3	1
3	3	1	2	1	2
1	1	3	2	2	1
1	2	1	3	3	2
1	3	2	1	1	3
2	1	2	1	3	2
2	2	3	2	1	3
2	3	1	3	2	1
3	1	3	3	1	2
3	2	1	1	2	3
3	3	2	2	3	1

notice that SA cost is at least one order of magnitude smaller than optimization runs ones.

As aforementioned, the number of uncertain parameters of \mathbf{p} are equal to the number of the elements of \mathbf{p}_p . Thus, after the robust-based optimization, also the scattering of the optimized robust solutions, due to the uncertainties of \mathbf{p}_p , could be evaluated taking advantage of F_{12} , L_{18} and B_{48} arrays. The scattering of the optimized solutions is determined employing a single evaluation of the merit function Φ_{avg} for the optimal value of \mathbf{b} , using all nominal values for the uncertain parameters of \mathbf{p} , whereas the elements of \mathbf{p}_p are varied in accordance with the DOE array.

5.5 Numerical Results

Optimization runs are performed on a 20-cores parallel computing machine and 100 hours, 35 hours and 25 hours are required when B_{48} , L_{18} and F_{12} arrays are respectively employed. Optimized design parameters are presented in Tab. 5.11 for robust solutions. Deterministic optimal design is also added to solutions comparison as DET. $m_{u,avg}$ and Δ_{avg} are also reported and calculated by means of Eq.(5.37) and (5.36). One can see that all the robust solutions exhibit an average violation null or close to zero thanks to the chosen value of k_h in the merit function

Table 5.8: Box–Behnken’s array.

1	1	2	1	2	2	1	2	2	1	1	2
1	1	2	3	2	2	1	2	2	1	3	2
1	3	2	1	2	2	1	2	2	3	1	2
1	3	2	3	2	2	1	2	2	3	3	2
3	1	2	1	2	2	3	2	2	1	1	2
3	3	2	1	2	2	3	2	2	1	3	2
3	1	2	3	2	2	3	2	2	3	1	2
3	3	2	3	2	2	3	2	2	3	3	2
2	1	1	2	1	2	2	1	2	2	1	1
2	1	3	2	1	2	2	1	2	2	1	3
2	1	3	2	3	2	2	1	2	2	3	1
2	1	1	2	3	2	2	1	2	2	3	3
2	3	3	2	3	2	2	3	2	2	1	1
2	3	3	2	1	2	2	3	2	2	1	3
2	3	1	2	3	2	2	3	2	2	3	1
2	3	1	2	1	2	2	3	2	2	3	3
2	2	1	1	2	1	1	2	1	2	2	1
2	2	1	1	2	3	1	2	1	2	2	3
2	2	1	3	2	1	1	2	3	2	2	3
2	2	1	3	2	3	3	2	1	2	2	1
2	2	3	1	2	1	3	2	1	2	2	3
2	2	3	1	2	3	3	2	3	2	2	1
2	2	3	3	2	1	3	2	3	2	2	1
2	2	3	3	2	3	3	2	3	2	2	3

formulation (see Eq.(5.35)). For this reason Φ_{avg} and $m_{u,avg}$ have roughly the same magnitude.

Looking at the values of grain length L_b and web thickness w in Tab. 5.11, all robust solutions have a longer and thicker fuel grain but almost constant grain outer radius R_g with respect to DET solution, resulting in an approximately 200 kg increase in fuel mass m_F , as shown in Tab. 5.12. On the other hand, total oxidizer mass m_O , that is the design parameters reported as $(m_O)_f$ in Tab. 5.11, presents small differences between robust and deterministic solutions: L_{18} and B_{48} optimized solutions are characterized by a ≈ 50 kg increase in oxidizer mass with respect to DET solution, whereas F_{12} shows an even smaller difference (less than 0.1%).

Engine dry mass m_{dry} of L_{18} solution is significantly greater than DET and other robust solutions ones. Looking at Tab.5.12 one can observe that the main differences in robust solutions mass budgets concern nozzle mass m_{nz} , pressurizing gas mass m_g and auxiliary tank mass m_a . Structural nozzle mass is given by

Table 5.9: PSO settings.

Number of generations, N_G	1000
Number of particles, N_I	20
Dimension of particles	6
Ranges of particles	$\mathbf{b}_U - \mathbf{b}_L$
PSO method	1-trelea type 1
Cognitive acceleration, $C1$	2.0
Social acceleration, $C2$	2.0
Check population method	Saturation
End velocity weight	0.4
Linear varying factor	0.2
Maximum velocity, v_{max}	$0.25(\mathbf{b}_U - \mathbf{b}_L)$
Mass mutation parameter	98%

Table 5.10: Computational cost comparison.

DOE technique	Number of Φ_i evaluations
F_{12} array	$13 \cdot 20 \cdot 1000 = 2.6 \cdot 10^5$
L_{18} array	$19 \cdot 20 \cdot 1000 = 3.8 \cdot 10^5$
B_{48} array	$49 \cdot 20 \cdot 1000 = 9.8 \cdot 10^5$
SA	$100 \cdot (19 + 1) \cdot 10 = 2 \cdot 10^4$

expansion area ratio E_i and initial throat area $(A_t)_i$, which in turn is a function of initial port area $(A_p)_i$ and initial throat-to-port area ratio $J = 0.5$ in nominal condition. L_{18} solution has a longer and heavier nozzle due to higher E_i , despite its initial port and throat areas are slightly smaller than F_{12} and B_{48} ones due to a thicker fuel grain. The amount of pressurizing gas (i.e. m_g magnitude), required to grant sufficiently high thrust levels during operation, is determined by $(m_O)_{BD}$ and $p_{t,i}$. The latter is fixed and equal to 25 bar in nominal conditions, whereas the first is remarkably higher for L_{18} solution with respect to deterministic and other robust solutions ones, resulting in greater m_g . The same goes for m_a since it is a function of $(m_O)_{BD}$ too. For the sake of completeness, Table 5.13 presents normalized mass ratios for deterministic and robust solutions, that could be useful to compare the present case with other launcher architectures.

In the end, payload mass differences between robust solutions and deterministic

Table 5.11: DET, F_{12} , L_{18} and B_{48} results.

	R_g	w	L_b	$(m_O)_{BD}$	$(m_O)_f$	E_i	$m_{u,avg}$	Δ_{avg}	Φ_{avg}
	m	m	m	kg	kg	-	kg	km	kg
DET	0.585	0.276	4.430	3269	7350	15.00	2281	172	-1135
F_{12}	0.589	0.292	4.466	3279	7343	16.11	2102	0.0	2101
L_{18}	0.588	0.297	4.473	3609	7397	17.23	1977	0.0	1977
B_{48}	0.592	0.292	4.463	3254	7396	15.73	2001	1.3	2001

Table 5.12: Mass budget comparison (in nominal conditions).

	m_u	m_P	m_{dry}	m_O	m_F	m_{cc}	m_t	m_{nz}	m_{case}	m_g	m_a
	kg	kg	kg	kg	kg	kg	kg	kg	kg	kg	kg
DET	2281	10578	1127	7350	3228	160	298	327	164	24	153
F_{12}	2102	10754	1131	7343	3411	163	297	327	165	24	154
L_{18}	1977	10848	1161	7397	3451	163	299	337	167	27	169
B_{48}	2026	10830	1131	7396	3434	164	299	326	165	24	153

Table 5.13: Mass budget comparison: normalized ratios (in nominal conditions).

	$\frac{m_u}{m_i}$	$\frac{m_P}{m_i}$	$\frac{m_P}{m_P+m_{dry}}$
	-	-	-
DET	0.157	0.728	0.904
F_{12}	0.145	0.741	0.905
L_{18}	0.136	0.747	0.903
B_{48}	0.140	0.746	0.905

one are due to an increase in total propellant mass m_P , that is required to fulfill the mission even when uncertain parameters assume off-nominal values. Results show that the additional fuel mass is obtained increasing grain length and web thickness, whereas grain outer radius remains almost equal to deterministic solution. This optimization strategy seems to be caused by the functional relationship that links grain outer radius, web thickness and grain length to engine dry mass. Looking at Fig.5.3 presented in Sec.5.2, one can observe that an increase in R_g would lead to heavier combustion chamber and nozzle, an increase in L_b to a heavier combustion chamber and engine casing, whereas an increase in w to a lighter nozzle (see Eq.(5.1) and (5.16) in Sec.5.2). Thus, optimization algorithm tends to converge to robust solutions that use the beneficial effect of a larger w to maintain an almost constant engine dry mass, reducing nozzle mass, and at the same time obtain the required larger fuel mass. The alternative strategy to increase m_F (i.e. increase also or

only R_g) would lead to both a heavier combustion chamber and a heavier nozzle, resulting in greater dry mass and thus smaller payload mass.

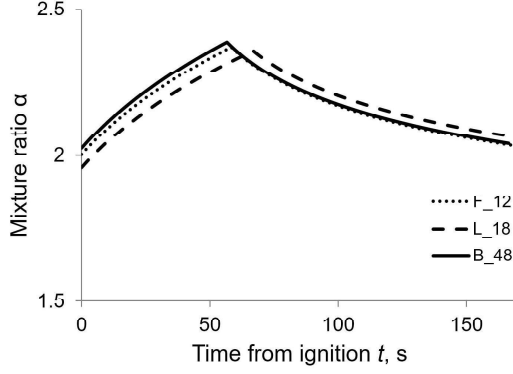


Figure 5.4: Mixture ratio α vs. time.

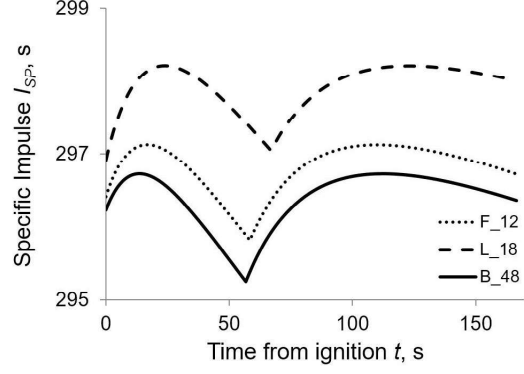


Figure 5.5: Specific impulse I_{SP} vs. time.

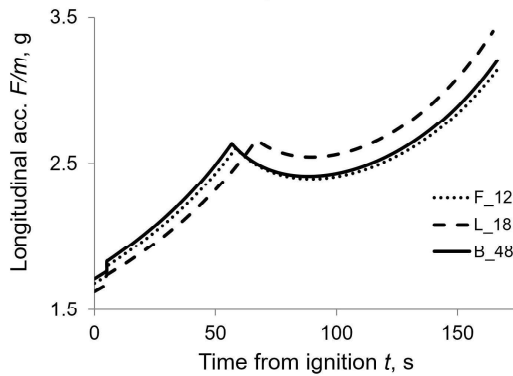


Figure 5.6: Longitudinal acceleration vs. time: first burn.

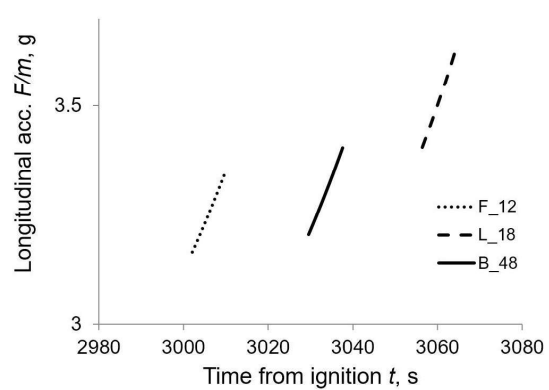
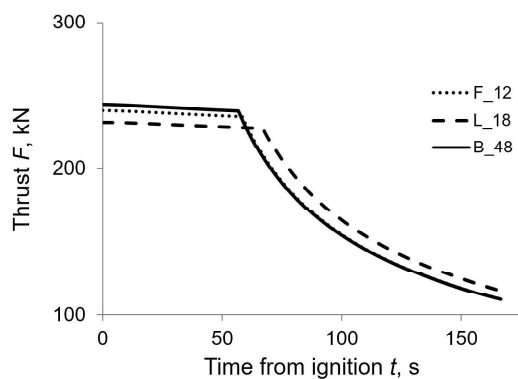
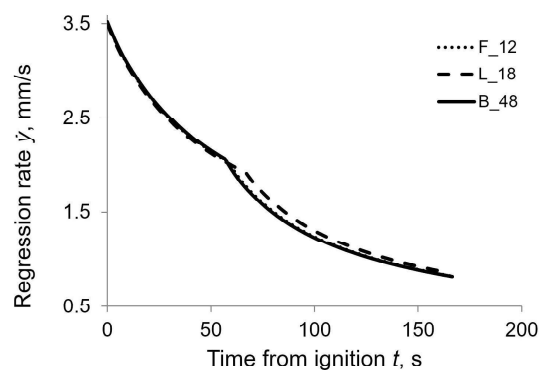


Figure 5.7: Longitudinal acceleration vs. time: second burn.

Figures 5.4-5.9 show main performance index and other quantities of interest for the optimized robust solutions. Plots of the second burn are here omitted (except longitudinal acceleration one) because they are not very significant due to its short duration. One can notice that L_{18} solution exhibits a slightly different behavior with respect to F_{12} and B_{48} ones: lower mixture ratio α , higher specific impulse I_{SP} , smaller thrust F during a longer constant pressure phase and greater thrust during a shorter blowdown phase. Looking at Fig.5.6 and 5.8, the thrust plot is smooth, whereas longitudinal acceleration presents a small gap approximately around 10s after engine ignition. This gap is caused by a stage mass discontinuity

Figure 5.8: Thrust F vs. time.Figure 5.9: Fuel grain regression rate \dot{y} vs. time.

due to the fairing jettisoning that occurs at the turn of trajectory phases (1) and (2) as presented in Sec.5.3. Fig.5.7 shows that the longitudinal acceleration of L_{18} at HRE burnout exceed 3.5g, whereas other robust solutions does not, because thrust level during second burn is actually greater against an almost equal stage final mass. However, all robust solutions have a maximum acceleration within the third stage maximal acceleration requirement of the current VLV.[1]

Table 5.14: Results of the cross evaluation of the optimal solutions.

Solution	Method of evaluation		
	F_{12} kg	L_{18} kg	B_{48} kg
F_{12}	2101.6	181.6	-3.7
L_{18}	-	1977.4	1977.5
B_{48}	-	1334.2	2000.9

A deeper insight into actual solution robustness and effectiveness of the employed DOE techniques can be obtained by means of a cross-evaluation of the optimization merit function. F_{12} optimal design is tested using L_{18} and B_{48} arrays, that requires 6 and 36 additional uncertain combination in the average merit function evaluation. Results are presented in the first row of Tab.5.14. F_{12} design shows remarkable performance drops when the merit function is evaluated through bigger DOE arrays. This behavior proves that F_{12} optimized solution does not grant an acceptable robustness when more than one uncertain parameters have off-nominal values, confirming the supposed strong effect on model outputs of uncertainties interactions that F_{12} array neglects. The second row of Tab.5.14 reports

the average merit function for the optimal design of Taguchi's L_{18} array evaluated also by means of B_{48} array. In this case, merit functions results to be really close to each other, highlighting the robustness of Taguchi's solution even when calculated using a bigger DOE array (B_{48} array requires 20 additional uncertain parameters combinations with respect to L_{18}). In the third row of Tab.5.14, B_{48} optimal design is evaluated using also L_{18} array, resulting in a significantly reduced $\Phi_{avg} = 1334.18$ kg. This behavior is caused by an uncertain parameter combination corresponding to "all parameters lower than nominal", that is considered by L_{18} array and neglected by B_{48} one. This particular uncertainties combination leads to a launcher crash on Earth's surface when B_{48} optimal design is used. Hence, L_{18} solution seems to be characterized by a greater robustness than B_{48} one. On the other hand, B_{48} solution outperforms L_{18} one when optimal payload mass is merely considered, since $m_{u,avg} = 2001$ kg for B_{48} , that is a 23 kg improvement with respect to Taguchi's optimal solution. In the end, when a fast and thoroughly robust solution is required, L_{18} array appear to be the better choice, albeit the optimized solution could be too conservative. Instead, the use of B_{48} array can grant higher payload mass along with a fair robustness level, but the computational cost of the optimization results to be more than doubled with respect to Taguchi's DOE array.

The last step of the robust-based optimization is the evaluation of the scattering of the optimized solutions due to the elements of the vector \mathbf{p}_p , that are ρ_{Al} , ρ_{abl} , ρ_O , T_g , s_{lin} , V_{ull} . As aforementioned, since the number of elements of \mathbf{p}_p are equal to the number of uncertain parameters considered in the robust-based optimization, the same DOE arrays are used in the scattering evaluation. The elements of \mathbf{p} are now regarded as constants and their nominal values are taken into account (see Tab. 5.3). On the other hand, the elements of \mathbf{p}_p are varied in accordance with the levels combinations of F_{12} , L_{18} and B_{48} arrays. The computational effort of the scattering evaluation is quite negligible, with respect to optimization one, because a single average merit function evaluation is performed by means of each DOE array (i.e. a total of three additional merit function evaluations have to be performed). Table 5.15 presents Φ_{avg} values of F_{12} optimal design point when F_{12} , L_{18} and B_{48} arrays are employed to deal with \mathbf{p}_p variation. Analogously, the results obtained considering L_{18} and B_{48} optimal design points are presented in Tab. 5.16 and 5.17. σ_Φ indicates the weighted standard deviation of the average merit function values due to \mathbf{p}_p uncertainties. Weights here used are the same employed in Φ_{avg} and defined in Eq.(5.34). Nominal merit function value, corresponding to all nominal values for both \mathbf{p} and \mathbf{p}_p elements, is reported as NOM in Tab. 5.15-5.17.

In all experimental runs performed in the scattering evaluation, the insertion altitude h_i is always greater than mission target one (i.e. $h_i \geq h^* = 700$ km), thus $\Phi_{avg} = m_{u,avg}$. All h_i values, obtained varying \mathbf{p}_p elements, are equal to corresponding nominal ones, that are $h = 951.13$ km, $h = 1129.37$ km and $h = 1043.12$ km when F_{12} , L_{18} and B_{48} optimal design points are respectively considered. Thus \mathbf{p}_p variations results to be unable to cause altitude violation. Φ_{avg} values

Table 5.15: Scattering of F_{12} robust solution.

	Φ_{avg} kg	σ_{Φ} kg
NOM	2101.6	0.0
F_{12}	2101.6	6.0
L_{18}	2101.5	11.9
B_{48}	2101.5	10.4

Table 5.16: Scattering of L_{18} robust solution.

	Φ_{avg} kg	σ_{Φ} kg
NOM	1977.5	0.0
F_{12}	1977.4	6.2
L_{18}	1977.3	12.2
B_{48}	1977.3	10.7

Table 5.17: Scattering of B_{48} robust solution.

	Φ_{avg} kg	σ_{Φ} kg
NOM	2026.5	0.0
F_{12}	2026.5	6.0
L_{18}	2026.4	11.9
B_{48}	2026.4	10.5

are close to nominal ones for all optimal design points, since σ_{Φ} is always small. Moreover, Φ_i values due to \mathbf{p}_p variations, are larger than the corresponding optimal solutions ones in each i -th experimental run performed in scattering evaluation (i.e. actual $m_{u,i}$ are all larger than $m_{u,avg}$).

In the end, results suggest that fluctuation in ρ_{Al} , ρ_{abl} , ρ_O , T_g , s_{lin} , V_{ull} values are not able to threaten mission goals fulfillment, having really small impacts on model outputs around optimized design points. Hence, the choice to neglect \mathbf{p}_p uncertainties in the first part of the optimization procedure allows to speed up the whole robust-based process, granting at the same time the achievement of the required robustness in the design.

5.6 Conclusions

In first sections of this chapter, the author has outlined the main features of the current design of the Vega launcher (5.1), described the hybrid rocket engine model and direct optimization approach (5.2), summarized the indirect trajectory optimization method (5.3), presented the sensitivity analysis and parameters screening procedure (5.4.1) and depicted the design of experiment techniques required by the robust-based procedure (5.4.2).

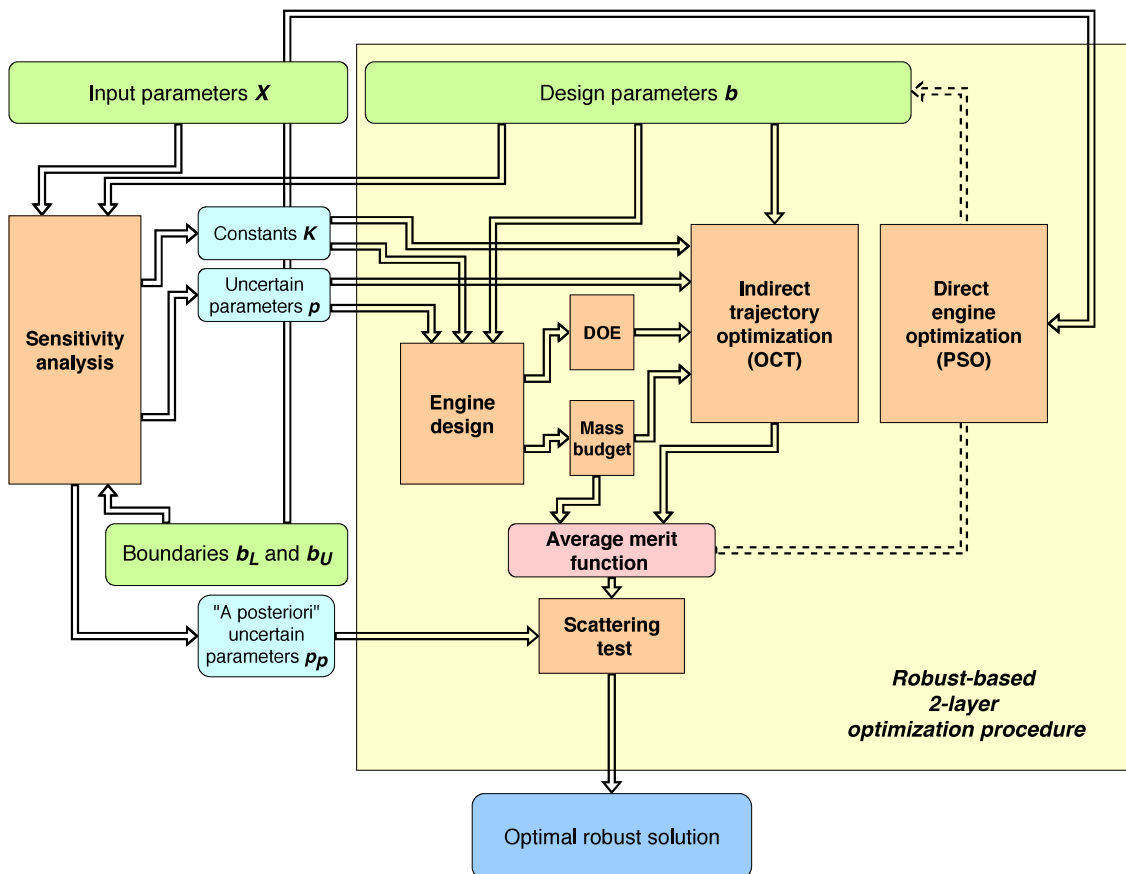


Figure 5.10: Scheme of the employed robust-based optimization procedure. Green boxes are the input of the optimization problem, light blue boxes contain SA outputs, orange boxes present the main sub-models and tools used and the blue box reports optimization outputs. The dotted link on the right represents the feedback due to PSO algorithm which adjusts the design parameters aiming at the maximization of the merit function.

Figure 6.9 graphically illustrates the developed robust-based optimization procedure, pointing out the inputs and the outputs of the whole numerical model and highlighting functional links and relationships between sub-models. Clearly, the

robust-based optimization of a HRE is intrinsically and deeply multi-disciplinary, not only concerning engine and trajectory optimization, that are linked by HRE unique architecture, but also because uncertainties have to be considered at every level in the design process (model, sub-models and components).

The number of uncertain parameters plays a major role in the computational time required by the optimization because even few additional parameters cause an exponential growth in the number of experimental runs performed accordingly to the chosen DOE technique. Luckily, a proper SA and screening of the input parameters proved to allow for an affordable robust-based optimization process. In the previous Sec. 5.5 numerical results showed that a sufficiently high robustness level can be achieved when Taguchi's or Box-Behnken's methods are employed to manage uncertainties. In the present case, the cost to grant robustness in the design resulted to be a reasonably small payload reduction (12 – 13%), with respect to deterministic optimal design point.

The robust solutions tend to have large web thickness w and grain length L_b , obtaining the additional amount of fuel required to manage the effects of uncertainties during HRE burn. At the same time, the resulting engine dry mass increase is limited and the average altitude violation is zero, granting 100% target orbit reaching and satisfactory performance in terms of payload mass.

References

- [1] Arianespace. *VEGA, User's Manual, Issue 4 - Revision 0*. [Online; accessed 2-July-2019]. 2014. URL: http://www.arianespace.com/wp-content/uploads/2015/09/Vega-Users-Manual_Issue-04_April-2014.pdf.
- [2] AVIO. *M10 MOTOR*. [Online; accessed 17-September-2019]. 2017. URL: <http://www.avio.com/en/vega/vega-e/vega-e-mira-motor/>.
- [3] DH Barker et al. "A simplified method of predicting char formation in ablating rocket exit cones(Char formation in solid rocket nozzle exit cones made from reinforced plastic predicted from corrosion standpoint)". In: *CHEMICAL ENGINEERING PROGRESS, SYMPOSIUM SERIES*. Vol. 61. 59. 1965, pp. 108–114.
- [4] Marcel Barrere et al. *Rocket propulsion*. Tech. rep. LTAS, 1960.
- [5] Daniele Bianchi and Francesco Nasuti. "Numerical analysis of nozzle material thermochemical erosion in hybrid rocket engines". In: *Journal of Propulsion and Power* 29.3 (2013), pp. 547–558.
- [6] Charles D Brown. *Spacecraft propulsion*. American Institute of Aeronautics and Astronautics, 1996.

- [7] Brian Cantwell, Arif Karabeyoglu, and David Altman. “Recent advances in hybrid propulsion”. In: *International Journal of Energetic Materials and Chemical Propulsion* 9.4 (2010).
- [8] Lorenzo Casalino, Guido Colasurdo, and Dario Pastrone. “Integrated design of hybrid rocket upper stage and launcher trajectory”. In: *45th AIAA/ASME/SAE/ASEE Joint Propulsion Conference & Exhibit*. 2009, p. 4843.
- [9] Lorenzo Casalino, Guido Colasurdo, and Dario Pastrone. “Optimal low-thrust escape trajectories using gravity assist”. In: *Journal of Guidance, Control, and Dynamics* 22.5 (1999), pp. 637–642.
- [10] Lorenzo Casalino, Francesca Letizia, and Dario Pastrone. “Optimization of hybrid upper-stage motor with coupled evolutionary/indirect procedure”. In: *Journal of Propulsion and Power* 30.5 (2014), pp. 1390–1398.
- [11] Lorenzo Casalino, Filippo Masseni, and Dario Pastrone. “Robust Design Approaches for Hybrid Rocket Upper Stage”. In: *Journal of Aerospace Engineering* 32.6 (2019), p. 04019087.
- [12] Lorenzo Casalino, Filippo Masseni, and Dario Pastrone. “Viability of an Electrically Driven Pump-Fed Hybrid Rocket for Small Launcher Upper Stages”. In: *Aerospace* 6.3 (2019), p. 36.
- [13] Lorenzo Casalino and Dario Pastrone. “Optimal design and control of hybrid rockets for access to space”. In: *41st AIAA/ASME/SAE/ASEE Joint Propulsion Conference & Exhibit*. 2005, p. 3547.
- [14] Lorenzo Casalino and Dario Pastrone. “Optimal design of hybrid rocket motors for launchers upper stages”. In: *Journal of Propulsion and Power* 26.3 (2010), pp. 421–427.
- [15] Lorenzo Casalino and Dario Pastrone. “Optimization of a hybrid rocket upper stage with electric pump feed system”. In: *46th AIAA/ASME/SAE/ASEE Joint Propulsion Conference & Exhibit*. 2010, p. 6954.
- [16] David J Edwards and Robert W Mee. “Fractional Box–Behnken Designs for One-Step Response Surface Methodology”. In: *Journal of Quality Technology* 43.4 (2011), pp. 288–306.
- [17] RA Ellis. “Solid Rocket Motor Nozzles-NASA Space Vehicle Design Criteria (Chemical Propulsion)”. In: *NASA SP-8115* (1975).
- [18] MA Karabeyoglu, D Altman, and Brian J Cantwell. “Combustion of liquefying hybrid propellants: Part 1, general theory”. In: *Journal of Propulsion and Power* 18.3 (2002), pp. 610–620.
- [19] Gerald A Marxman. “Combustion in the turbulent boundary layer on a vaporizing surface”. In: *Symposium (International) on Combustion*. Vol. 10. 1. Elsevier. 1965, pp. 1337–1349.

- [20] Bonnie J McBride, Martin A Reno, and Sanford Gordon. “CET93 and CETPC: An interim updated version of the NASA Lewis Computer program for calculating complex chemical equilibria with applications”. In: (1994).
- [21] Dario Pastrone. “Approaches to low fuel regression rate in hybrid rocket engines”. In: *International Journal of Aerospace Engineering* 2012 (2012).
- [22] Dario Pastrone and Lorenzo Casalino. “Optimal Robust Design of Hybrid Rocket Engines”. In: *Space Engineering*. Springer, 2016, pp. 269–285.
- [23] George P Sutton and Oscar Biblarz. *Rocket propulsion elements*. John Wiley & Sons, 2016.
- [24] Genichi Taguchi. *Robust engineering*. Vol. 224.
- [25] YV HAIMES YV, Leon S Lasdon, and DA DA WISMER. “On a bicriterion formation of the problems of integrated system identification and system optimization”. In: *IEEE Transactions on Systems, Man and Cybernetics* 3 (1971), pp. 296–297.
- [26] Hao Zhu et al. “Uncertainty analysis and design optimization of hybrid rocket motor powered vehicle for suborbital flight”. In: *Chinese Journal of Aeronautics* 28.3 (2015), pp. 676–686.
- [27] Hao Zhu et al. “Uncertainty analysis and probabilistic design optimization of hybrid rocket motors for manned lunar landing”. In: *Science China Technological Sciences* 58.7 (2015), pp. 1234–1241.

Chapter 6

Real World Application: Electrical Turbo Pump Upper Stage

In the previous Chapter 5, the author presented the robust design and optimization of a hybrid powered upper stage able to replace the upper stages of the current Vega launcher. A simple Gas-Pressurized Feed System (GPFS) has been considered in such application because of its low cost and reliability. However, gas-pressurized systems are characterized by some drawbacks and thus an innovative turbo-pump feed system will be taken into consideration in this Chapter.

In HREs, large thrust level during operation requires large regression rate values, that can be achieved by having a high oxidizer mass flow in the combustion chamber. Oxidizer flow in turn is determined by the pressure drop between oxidizer tank and combustion chamber head-end pressures. Thus, high oxidizer and auxiliary tanks pressures are mandatory to grant nice thrust level, when a gas-pressurized feed system is employed, making the tanks structural masses remarkably high. Looking at Tab. 5.12 (see Chapter 5 on page 71) one can notice that tanks structural masses $m_t + m_a$ represent approximately one-third of the total engine dry mass and that oxidizer mass constitutes half of the total stage mass for the optimized robust solutions. Hence, the use of a turbo-pump feed system could greatly reduce the engine dry mass thanks to lighter oxidizer tank, the absence of auxiliary vessels for the pressurizing gas and the elimination of the gas itself.

The power source of the turbo-pump feed system is classically a turbine fed by a working fluid. Most common LREs architectures use hot gases coming from a separated gas generator (gas generator cycle), energized engine coolant (expander cycle), a pre-burned propellants mixture (staged combustion cycle) or hot gases directly from the main combustion chamber (tap-off cycle).[13] Since the '90s, Electrical Pump Feed Systems (EPFSs) have been also considered for small bi-propellant LREs, where an electric motor replaces the turbine and batteries are employed

as power source.[6, 10] More recently, the development of batteries and electric motors technologies makes EPFSs even more intriguing and increases their competitiveness from a purely performance-based point of view.[1, 12, 9, 3] An EPFS bi-propellant liquid engine has been also taken into consideration to be used in a Mars Ascent Vehicle (MAV) in 2016.[14] Alongside electric powered ones, also conventional propulsion systems have been considered. Nevertheless, EPFS resulted able to outperform conventional GPFSs, albeit lower in technology readiness level. In 2018, the successful launch of the Rocket Lab’s Electron launch vehicle proved the feasibility of an EPFS-based small satellite launcher.[15] Electron is a two-stage launcher, powered by the Rutherford engine, a LOX/RP1 LRE developed by Rocket Lab’s itself that uses an innovative EPFS. In 2018, Kwak et al. proposed the use of an EPFS LOX/kerosene engine in the Korean Space Launch Vehicle-II (KSLV-II), demonstrating the feasibility of the electric-powered system. KSLV-II reference mission is the insertion of a 1500 kg payload into a 700 km orbit.[7]

Concerning direct HREs operation, the generation of a proper working fluid, to be used in the turbine to power the turbo-pump, is more challenging than in LREs because only the oxidizer is in liquid state. A gas generator cycle can be employed, but auxiliary liquid fuel have to be boarded. Liquid HP can produce hot gases through catalytic decomposition, whereas an expander cycle is not feasible for LOX due to ineffective heating. On the other hand, a tap-off cycle could be used, but its complexity, cost and low reliability make it ill-suited for the use in a HRE. For these reasons, the electrically driven solution is much more intriguing in HREs than in LREs and will be detailed by the author in the following Sections.

6.1 Mathematical Model

In this Chapter the author proposed an alternative configuration, employing a different oxidizer feed system, for the same application presented previously in Chapter 5. Thus, the case study is exactly the same (see Section 5.1). Moreover, the vast majority of hybrid rocket engine model, ascent trajectory and optimization procedure are similar too (see Sections 5.2, 5.3 and 5.4 respectively). Differences are present in uncertainty model, design of the experiments method, merit function formulation and, obviously, in engine operational mode, due to the different feed system employed. In this Chapter, the author will present only the discrepancies in the mathematical model, since details about unchanged aspects of the procedure have been already reported in Chapter 5.

6.1.1 Feed System

During HRE operation, the oxidizer flow rate is a function of hydraulic resistance Z , pressure provided by the feed system employed p_{fs} and chamber head-end

pressure p_1 , as reported in Eq.(6.1). In Eq.(5.6) on page 55 $p_{fs} = p_t$ due to the oxidizer pressurization system, whereas here p_{fs} is equal to the pump discharge pressure p_d , since an EPFS is considered in place of a GPFS.

$$\dot{m}_O = \sqrt{(p_{fs} - p_1)/Z} \quad (6.1)$$

In an EPFS, oxidizer is fed to the combustion chamber by a pump, which is driven by an electric motor. The required energy is supplied to the motor by a battery pack during engine burn. Electrical components masses (i.e. motor, pump, auxiliary systems and batteries) are computed by means of typical power density (power to mass ratio) values that can be found in the existing literature. Therefore, motor and pump mass can be written by means of Eq.(6.2), where $P_{e,max}$ is the maximum electrical power required. Concerning power density value δ_{ep} , both current technology and advanced designs have been considered, assuming respectively $(\delta_{ep})_{ct} = 1.25 \text{ kW/kg}$ and $(\delta_{ep})_{ad} = 3.92 \text{ kW/kg}$. [1, 11, 7]

$$m_{ep} = \frac{P_{e,max}}{\delta_{ep}} \quad (6.2)$$

$$P_e = \frac{\dot{m}_O(p_d - p_t)}{\rho_O \eta_{ep}} \quad (6.3)$$

The electrical power required by the motor to drive the pump can be evaluated thanks to Eq.(6.3), where $p_t = 1 \text{ bar} = \text{constant}$ is the oxidizer tank pressure. The amount of pressurizing gas required to keep p_t constant is small and can be neglected. η_{ep} is the conversion overall efficiency of the electrical energy, stored in the battery pack, into the flow head rise. The author assumes two efficiency values: $(\eta_{ep})_{ct} = 0.64$ and $(\eta_{ep})_{ad} = 0.53$. The reader can notice that $(\eta_{ep})_{ad} < (\eta_{ep})_{ct}$, but motor and pump mass $m_{ep} \propto (\delta_{ep} \cdot \eta_{ep})^{-1}$ which is actually smaller when an advanced design is considered.

Batteries have to fulfill two requirements: provide the maximum electrical power $P_{e,max}$ and the total electrical energy $E_{e,tot}$ needed by the EPFS during the whole engine burn time. Here, the discharge time of the pump is equal to HRE burning time t_{burn} . Hence, the total electrical energy can be calculated by means of Eq.(6.4). Then, the mass of the required battery pack can be obtained employing typical values of power density δ_{bp} and energy density δ_{be} (energy to mass ratio). Moreover, the author assumed a safety factor of 1.2 in battery mass evaluation, as reported in Eq.(6.5).

$$E_{e,tot} = \int_0^{t_{burn}} P_e dt \quad (6.4)$$

$$m_b = 1.2 \max \left(\frac{P_{e,max}}{\delta_{bp}}, \frac{E_{e,tot}}{\delta_{be}} \right) \quad (6.5)$$

The author chooses to take into consideration Lithium batteries in the present application, because of their small size and light weight. Two couples of densities have been considered: $(\delta_{bp})_{ct} = 3.0 \text{ kW/kg}$ and $(\delta_{be})_{ct} = 90 \text{ Wh/kg}$, based on Ragone plots,[8] and $(\delta_{bp})_{ad} = 6.95 \text{ kW/kg}$ and $(\delta_{be})_{ad} = 198.5 \text{ Wh/kg}$, based on the most recent literature concerning Lithium-Polymer batteries state of the art.[7] Equation (6.4) can be easily integrated assuming constant power operation of the pump (i.e. $P_e = P_{e,tot} = \text{constant}$), resulting in Eq.(6.6), which gives the total energy $E_{e,tot}$ required by the EPFS.

$$E_{e,tot} = P_{e,max} t_{burn} \quad (6.6)$$

On the other hand, the pump constant power level $P_e = P_{e,max}$ is fixed by the value of the initial discharge pressure of the pump $(p_d)_i$ (see Eq.(6.3)). Thus, $(p_d)_i$ substitutes $(m_O)_{BD}$ in the design parameters vector \mathbf{b} , when a EPFS is employed in place of a GPFS, as reported in Eq.(6.7).

$$\mathbf{b} = [R_g, w, L_b, (m_O)_f, (p_d)_i, E_i] \quad (6.7)$$

The reader can notice that the evaluation of power-constrained battery pack mass can be done before the trajectory optimization takes place, because it is only function of $(p_d)_i$ and the selected power density. Energy-constrained mass, instead, has to be calculated "a posteriori", because depends on the actual engine burn time t_{burn} (i.e. on the optimized trajectory). Therefore, a characteristic burning time t_{burn}^* can be defined (see Eq.(6.8)), representing the mission duration for which both constraints are simultaneously fulfilled.

$$t_{burn}^* = \frac{\delta_{be}}{\delta_{bp}} \quad (6.8)$$

If $t_{burn} \leq t_{burn}^*$, energy-constrained mass is smaller than power-constrained one (the mission is short, energy is not an issue). Thus, the actual ascent trajectory does not affect batteries mass. On the other hand, if $t_{burn} \geq t_{burn}^*$, power-constrained mass is smaller than energy-constrained one (the mission is long, energy is an issue). In this case, an "a posteriori" check of the battery pack mass is required to take into account the additional energy needed by a longer mission (i.e. actual launcher payload is reduced due to the additional batteries boarded). For the sake of clarity, Tab.6.1 reports all the electric properties values here employed.

6.1.2 Mass Budget and Ascent Trajectory

The modification of the feed system requires a slightly different formulation of engine dry mass, with respect to Eq.(5.20) on page 58, to keep into account electric motor, pump and batteries masses. Moreover, engine dry mass, and thus the actual launcher payload, has to be adjusted after trajectory optimization keeping

Table 6.1: Electric properties.

	δ_{bp} kW/kg	δ_{be} Wh/kg	δ_{ep} kW/kg	η_{ep} -	t_{burn}^* s
current technology	3.00	90.00	1.25	0.68	108
advanced design	6.95	198.50	3.92	0.53	103

into account the mass of the additional batteries required if $t_{burn} \geq t_{burn}^*$. Therefore, "a priori" engine dry mass is given by Eq.(6.9), where $(m_b)_{prior}$ is power constrained (see Eq.(6.10)). The "a priori" payload mass can be computed by means of Eq.(6.11).

$$(m_{dry})_{prior} = m_{cc} + m_t + m_{nz} + m_{case} + m_g + (m_b)_{prior} + m_{ep} \quad (6.9)$$

$$(m_b)_{prior} = 1.2 \frac{P_{e,max}}{\delta_{bp}} \quad (6.10)$$

$$(m_u)_{prior} = m_i - ((m_{dry})_{prior} + m_p + m_{fairing}) \quad (6.11)$$

Once the ascent trajectory has been optimized, total HRE burn time t_{burn} is known. If the latter is greater than the characteristic burning time t_{burn}^* , batteries mass has to be increased to the energy constrained value reported in Eq.(6.12). Then, actual engine dry mass and payload mass are given by Eq.(6.13) and (6.14).

$$m_b = 1.2 \frac{E_{e,tot}}{\delta_{be}} = 1.2 \frac{P_{e,max} t_{burn}}{\delta_{be}} = (m_b)_{prior} + 1.2 \frac{P_{e,max}}{\delta_{be}} (t_{burn} - t_{burn}^*) \quad (6.12)$$

$$m_{dry} = (m_{dry})_{prior} + 1.2 \frac{P_{e,max}}{\delta_{be}} (t_{burn} - t_{burn}^*) \quad (6.13)$$

$$m_u = (m_u)_{prior} - 1.2 \frac{P_{e,max}}{\delta_{be}} (t_{burn} - t_{burn}^*) \quad (6.14)$$

Ascent trajectory optimization procedure is the same that has been presented in Sec.5.3 on page 59. The only difference concerns arcs splitting, due to the presence of a single operational mode for the feed system (i.e. constant power) in place of two (i.e. constant pressure and blow-down). Thus, only four arcs are needed to model the trajectory: first burn with fairing (1), first burn without fairing (2), coasting (3) and second burn (4).

6.2 Robust-based Optimization

Engine design is determined by six parameters when both GPFS and EPFS are employed. However design parameters vectors are slightly different as mentioned before (see Eq.(6.7)). Upper and lower boundaries are the same for the parameters that are in common between GPFS and EPFS, allowing for a better performance comparison. Table 6.2 reports boundaries vectors \mathbf{b}_L and \mathbf{b}_U .

Table 6.2: Boundaries of the elements of \mathbf{b} .

	R_g	w	L_b	$(m_O)_f$	$(p_d)_i$	E_i
	m	m	m	kg	bar	-
b_L	0.55	0.25	4.3	6971	10	15
b_U	0.60	0.35	4.5	7697	50	20

In a previous work, the use of an EPFS has been considered, but HRE design and optimization has been performed only from a deterministic point of view.[5] Here, uncertainties in the classical regression rate correlation has been taken into account. Thus uncertain parameters vector \mathbf{p} can be written as:

$$\mathbf{p} = [a, n] \quad (6.15)$$

whose levels are the same presented in Tab. 5.3 on page 62 that have already been used in Chapter 5. Here, a sensitivity analysis and screening of uncertain parameters have not been performed to maintain the problem as simple as possible in this early design stage. However, the management of regression rate uncertainties is well known to be the most challenging issue to the actual employment of hybrid based propulsion system.

Table 6.3: L_9 orthogonal array.

1	1
1	2
1	3
2	1
2	2
2	3
3	1
3	2
3	3

Therefore, merit function formulation is simpler than the one presented on page 66 in the previous Chapter 5. Each possible combination of levels for a and n is

considered, i.e. a 3-level L_9 orthogonal array is used in the DOE (see Tab.6.3). The average altitude constraint violation is given by Eq.(6.16) where a binomial distribution is assumed ($p_1 = p_3 = 0.25$ and $p_2 = 0.5$). The average altitude is then $h_{avg} = h^* - \Delta_{avg}$ and the optimization merit function can be written by means of Eq.(6.17). The author selects $k_h = 20$ kg/km and $\epsilon = h^* = 700$ km as done in Chapter 5 in the merit function formulation.

$$\Delta_{avg} = \sum_{ij} p_i p_j \max_{ij}(0, h^* - h_{ij}) \quad (6.16)$$

$$\Phi_{avg} = \mu - k_h \max(0, \epsilon - h_{avg}) \quad (6.17)$$

6.3 Numerical Results

Optimized robust design parameters and resulting performance are presented by means of Tab.6.4 and Tab.6.5. Current technology and advanced design have been considered in battery mass evaluation. The first row of both tables has been added by the author, for the sake of comparison, and reports optimal design parameters values and HRE performance using a GPFS and the same robust approach. Further details can be found in [4].

Looking at Tab.6.5, one can notice that all solutions have a null average altitude violation, resulting in $m_u = \Phi_{avg}$ and granted robustness. Both EPFS solutions present smaller grain outer radius R_g , greater web thickness w and a longer grain, with respect to GPFS solution. Hence, fuel grains result slender and thicker, whereas the initial port area $(A_p)_i$ and the initial throat area $(A_t)_i$ are smaller ($J = 0.5 = \text{constant}$) when an EPFS is used.

Table 6.4: Robust optimal design parameters.

	R_g	w	L_b	$(m_O)_f$	E_i	$(m_O)_{BD}$	$(p_d)_i$
	m	m	m	kg	-	kg	bar
GPFS	0.591	0.294	4.360	7403	17.32	3195	-
EPFS _{ct}	0.579	0.303	4.438	7408	17.44	-	27.7
EPFS _{ad}	0.563	0.334	4.368	7381	18.14	-	39.8

Concerning mass budget, Tab.6.6 highlights that total propellants masses are really close between GPFS and EPFS solutions. On the other hand, engine dry mass is remarkably smaller when electrical turbo pump systems are employed, regardless which power and energy densities are taken into account. Looking at Tab.6.7 one can notice that the main sources of dry mass saving are a far lighter oxidizer tank and nozzle. Oxidizer tank is lighter because of the absence of the high pressure

Table 6.5: Robust optimal design performance.

	m_u kg	Δ_{avg} km	Φ_{avg} kg	t_{burn} s
GPFS	2069.8	0.0	2069.8	177
EPFS _{ct}	2321.7	0.0	2321.7	157
EPFS _{ad}	2467.7	0.0	2467.7	158

pressurization required by GPFS, whereas nozzle mass is smaller because of the smaller initial throat area, despite a higher expansion ratio.

Due to the consistent reduction in engine dry mass, EPFS solutions have a remarkably greater payload mass, with respect to GPFS one: an improvement of roughly 230 kg (that is 11% of GPFS payload mass) is achieved employing current technology for electrical system, whereas payload mass grows of roughly 400 kg (that is $\approx 1/5$ of GPFS payload mass) when advanced design properties are considered. In Tab.6.8 normalized ratios are reported to compare EPFS solutions with other launcher architectures.

Table 6.6: Mass budget comparison: payload, propellants and total engine dry masses.

	m_u kg	m_P kg	m_{dry} kg	m_O kg	m_F kg
GPFS	2070	10768	1149	7404	3364
EPFS _{ct}	2322	10800	865	7408	3392
EPFS _{ad}	2468	10796	724	7381	3415

Table 6.7: Mass budget comparison: engine components and electrical systems masses.

	m_{cc} kg	m_t kg	m_{nz} kg	m_{case} kg	m_g kg	m_a kg	m_b kg	m_{ep} kg
GPFS	160.2	299.4	351.1	165.6	23.6	149.8	-	-
EPFS _{ct}	147.4	12.0	309.7	163.7	0.032	-	98.0	134.4
EPFS _{ad}	162.3	12.0	239.7	158.4	0.031	-	77.3	74.4

Since the second burn of the HRE has a very short duration, its influence on the rocket performance is limited. For this reason the following Figures 6.1-6.7 will show only rocket performance relative to the first burn, for the sake of simplicity.

Table 6.8: Mass budget comparison: normalized ratios.

	$\frac{m_u}{m_i}$	$\frac{m_P}{m_i}$	$\frac{m_P}{m_P+m_{dry}}$
	-	-	-
GPFS	0.143	0.741	0.904
EPFS _{ct}	0.160	0.744	0.926
EPFS _{ad}	0.170	0.743	0.937

Looking at Fig. 6.1 and 6.2 one can notice that pump discharge pressure and oxidizer mass flow present limited variations during operation ($\approx 5\%$) because of the constant power operation of the pump. Therefore the set of assumptions about electrical efficiency and power density for electric motor and pump are valid.

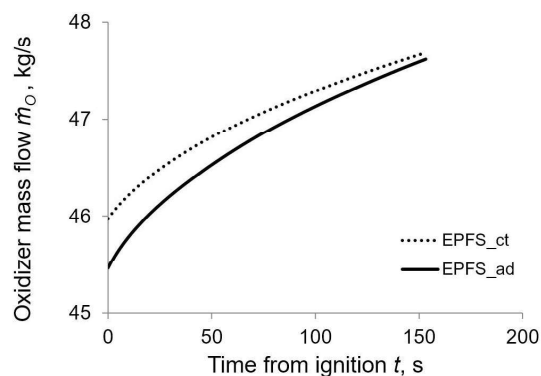
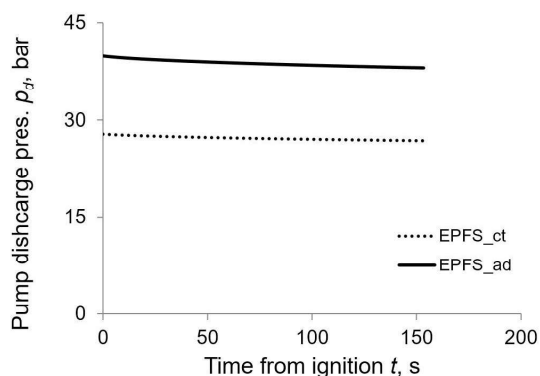


Figure 6.1: Pump discharge pressure p_d vs. time. Figure 6.2: Oxidizer mass flow \dot{m}_O vs. time.

Mixture ratio (see Fig.6.3) and fuel regression rate (see Fig.6.6) tend to be greater at the end of engine burn when EPFS is employed in place of GPFS. GPFS solution exhibits a greater thrust in the first half of the engine burn than EPFS solutions (see Fig.6.5) to avoid unacceptably low thrust during the subsequent blow down phase. On the other hand, the use of a turbo-pump system grants an almost constant thrust for all the burn duration, allowing for a lower initial thrust. EPFS_{ct} and EPFS_{ad} have similar thrust history but are the result of different optimization strategies. Current technology solution is characterized by a lower discharge pressure p_d (i.e. lower chamber pressure) and a larger nozzle (i.e. large throat area) than advanced design solution ones, because the lower value of δ_{ep} penalizes high-pressure designs. The better electrical properties of EPFS_{ad} solution, instead, allows for higher pressures and remarkable saving in electrical systems and nozzle masses.

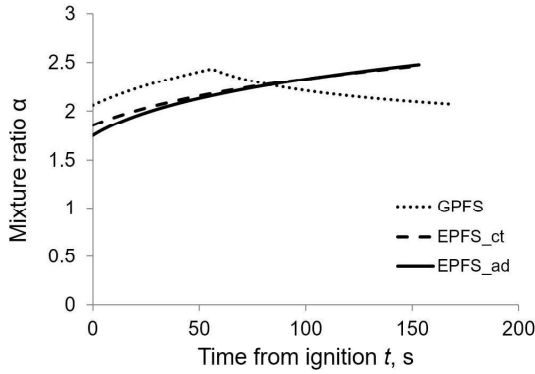


Figure 6.3: Mixture ratio α vs. time.

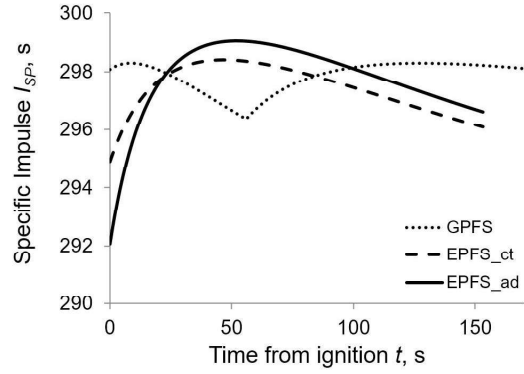


Figure 6.4: Specific impulse I_{SP} vs. time.

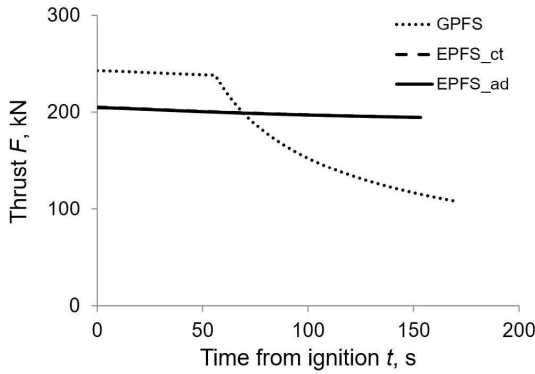


Figure 6.5: Thrust F vs. time.

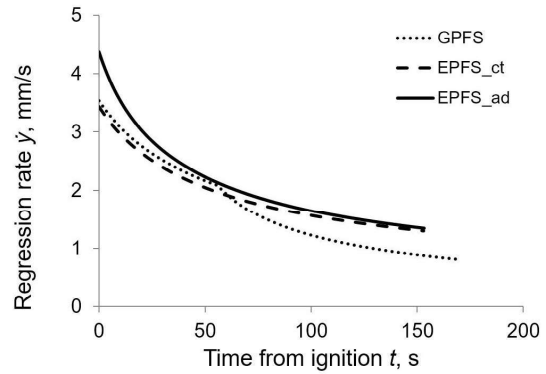


Figure 6.6: Fuel grain regression rate \dot{y} vs. time.

Figure 6.4 displays specific impulse I_{SP} histories for optimized robust solutions, highlighting different trends when GPFS or EPFS are used. In the end, Fig. 6.7 and Fig. 6.8 presents longitudinal acceleration histories for the first and second engine burn. One can notice that the maximum accelerations are obtained at the end of the second burn for all the solutions, but both EPFS solutions exhibits a final acceleration approximately equal to 6g, that, albeit being almost twice the GPFS one, falls within the third stage maximal acceleration requirement of the current VLV (i.e. 7g).[2]

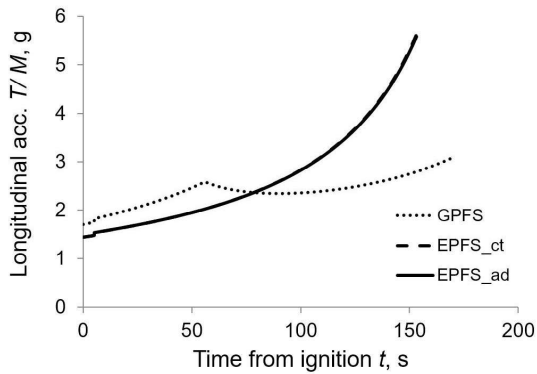


Figure 6.7: Longitudinal acceleration vs. time: first burn.

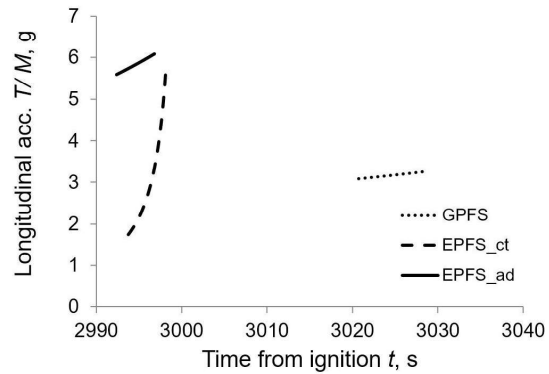


Figure 6.8: Longitudinal acceleration vs. time: second burn.

6.4 Conclusions

In this Chapter, the performance of two different feed systems, namely a gas pressurized feed system and an electrical pump feed system, have been compared when employed in a HRE upper stage. In Sec. 6.1 and 6.2 the author described the differences in the problem statements and robust optimization approaches between the present application and the one previously presented in Chapter 5.

Numerical results, reported in Sec. 6.3, pointed out that electrical pump systems are able to grant the required robustness, despite the uncertainty in the regression rate during operation, and, at the same, time outperform conventional gas-pressurized systems in HRE applications.

References

- [1] Terry M Abel and Thomas A Velez. *Electrical drive system for rocket engine propellant pumps*. US Patent 6,457,306. Oct. 2002.
- [2] Arianespace. *VEGA, User’s Manual, Issue 4 - Revision 0*. [Online; accessed 2-July-2019]. 2014. URL: http://www.arianespace.com/wp-content/uploads/2015/09/Vega-Users-Manual_Issue-04_April-2014.pdf.
- [3] PRE Bahn. *Rocket Engine System*. US Patent 9677503 B2. 2017.
- [4] Lorenzo Casalino, Filippo Masseni, and Dario Pastrone. “Robust Design Approaches for Hybrid Rocket Upper Stage”. In: *Journal of Aerospace Engineering* 32.6 (2019), p. 04019087.

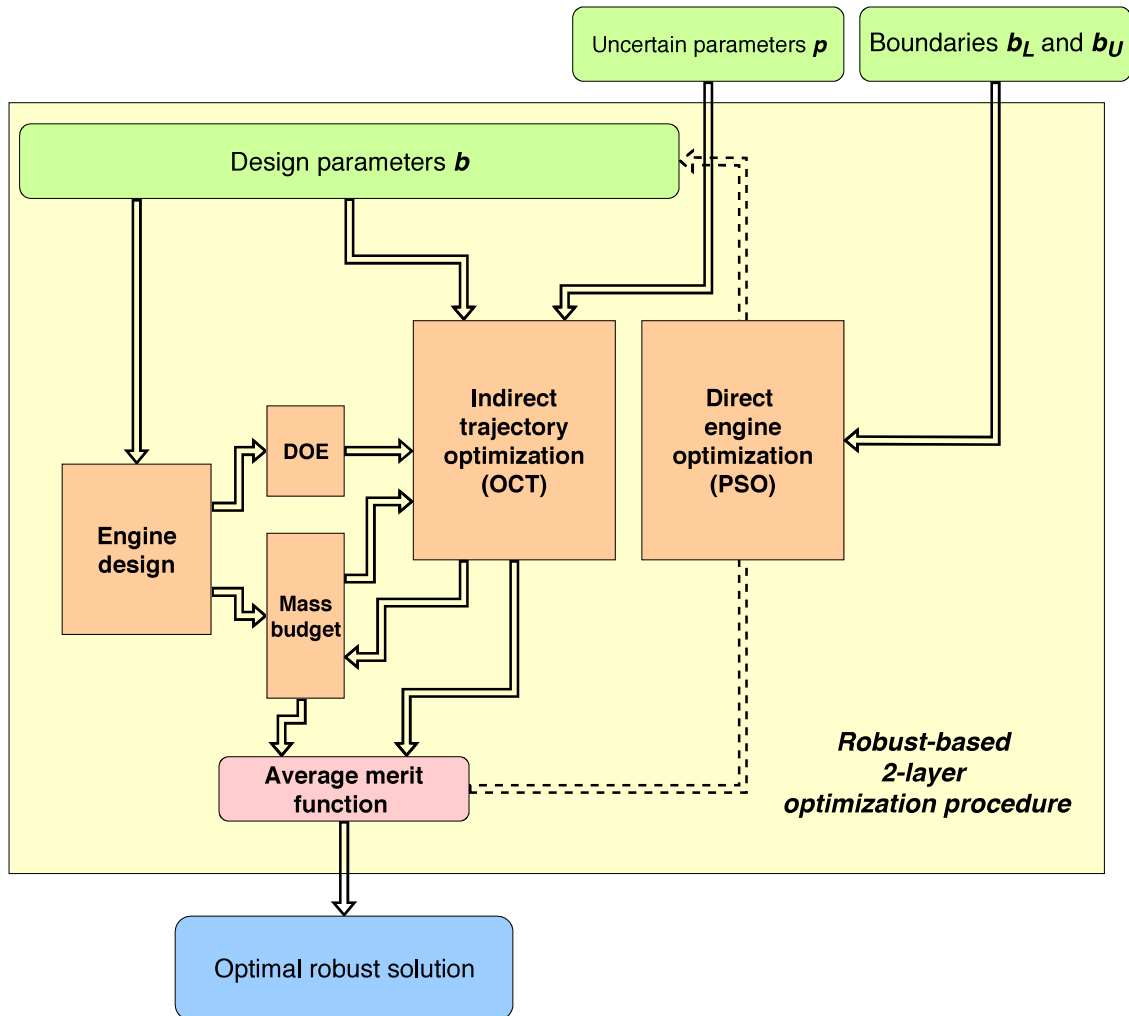


Figure 6.9: Scheme of the employed robust-based optimization procedure. Green boxes are the input of the optimization problem, orange boxes present the main sub-models and tools used and the blue box reports optimization outputs. The dotted link on the right represents the feedback due to PSO algorithm which adjusts the design parameters aiming at the maximization of the merit function. A backward link connects mass budget and trajectory optimization boxes, underlining that the actual battery mass, and thus the payload mass, have to be verified "a posteriori".

- [5] Lorenzo Casalino and Dario Pastrone. "Optimization of a hybrid rocket upper stage with electric pump feed system". In: *46th AIAA/ASME/SAE/ASEE Joint Propulsion Conference & Exhibit*. 2010, p. 6954.
- [6] Göran Johnsson and Mikael Bigert. "Development of small centrifugal pumps for an electric propellant pump system". In: *Acta Astronautica* 21.6-7 (1990), pp. 429–438.

REFERENCES

- [7] Hyun-Duck Kwak, Sejin Kwon, and Chang-Ho Choi. “Performance assessment of electrically driven pump-fed LOX/kerosene cycle rocket engine: Comparison with gas generator cycle”. In: *Aerospace Science and Technology* 77 (2018), pp. 67–82.
- [8] Woodbank Communications Ltd. *Battery and Energy Technologies*. [Online; accessed 1-July-2010]. 2005. URL: <https://www.mpoweruk.com/performance.htm>.
- [9] PA Pavlov Rachov, H Tacca, and D Lentini. “Electric Feed Systems for Liquid-Propellant Rockets”. In: *Journal of Propulsion and Power* 29.5 (2013), pp. 1171–1180.
- [10] Steven J Schneider. “Low thrust chemical rocket technology”. In: (1992).
- [11] AJ Sobin and WR Bissell. *Turbopump systems for liquid rocket engines*. National Aeronautics and Space Administration, 1974.
- [12] N Solda’ and D Lentini. “Opportunities for a liquid rocket feed system based on electric pumps”. In: *Journal of propulsion and power* 24.6 (2008), pp. 1340–1346.
- [13] George P Sutton and Oscar Biblarz. *Rocket propulsion elements*. John Wiley & Sons, 2016.
- [14] D Vaughan et al. “Technology development of an electrically driven pump fed storable liquid bi-propellant for a Mars ascent vehicle”. In: *Proceedings of the 68th International Astronautical Congress, Adelaide, Australia*. 2017, pp. 25–29.
- [15] G Waxenegger-Wilfing, RHS Hahn, and J Deeken. “Studies on Electric Pump-Fed Liquid Rocket Engines for Micro-Launchers”. In: *Proceedings of the Space Propulsion Conference, Seville, Spain*. 2018, pp. 14–18.

Chapter 7

Conclusions

In Chapter 5 and 6 the author presented two numerical applications of the developed robust-based design and optimization procedure for hybrid rocket engines. A hybrid powered upper stage, suitable as a replacement of the third and fourth stages of the current Vega launcher, has been considered in both cases.

In Chapter 5 a gas pressurized feed system has been taken into account in the hybrid rocket engine design and a complete uncertainty analysis has been performed prior to optimization. First a sensitivity analysis has been carried out by means of the Morris Method, which allowed for the identification of the most significant source of uncertainty. Six parameters had major effects: nozzle throat erosion coefficient, fuel regression rate correlation coefficient and exponent, fuel density, initial oxidizer tank pressure and initial throat to port area ratio. The effect of the uncertainty due to these parameters was so strong that their variations had to be taken into account in each merit function evaluation. A mission specific robust-based formulation has been used, in order to grant robustness in the optimized design found out and the actual attainment of mission goals, despite the presence of such uncertainties. In addition, the outputs of the sensitivity analysis showed that a second group of model parameters had minor, but not negligible, effects on model outputs. In the proposed robust-based procedure, performance variation due to this group of parameters has been checked "a posteriori", since the computational cost associated to additional uncertain parameters within the optimization procedure would have been remarkably high. Several design of experiments techniques, namely a fractional factorial design, Taguchi's L_{18} orthogonal array and Box Behnken design have been employed to properly characterize the effects of both groups of uncertain parameters on system performance.

In Chapter 6 the same hybrid rocket engine application has been considered, but an electrical turbo pump feed system has been employed in place of a gas pressurized one, aiming at testing the viability of such feed system for hybrid powered upper stages. In order to reduce the performance variability due to uncertainty, in this first attempt employing electrical systems, a simpler robust model has been used.

Only regression rate correlation coefficient and exponent have been regarded as uncertain, since they resulted to be the most critical ones both in the literature about hybrids and in the sensitivity analysis performed in the previous Chapter.

In either case the optimization focused on the maximization of the payload mass inserted in an assigned orbit (i.e. 700 km circular polar orbit). A linear combination of payload mass and attained orbit altitude has been employed as merit function. A particle swarm optimization algorithm has been used to guide the procedure adjusting design parameters values, whereas an indirect method optimized the ascent trajectory for each given engine design. In order to properly evaluate the noise due to uncertain parameters, several merit function evaluations have been performed varying uncertain parameters, as prescribed by the selected design of experiments technique, while keeping fixed the design parameters. In this way, an average performance has been calculated for each engine design and the robust-based procedure resulted able to minimize the effect of uncertainty achieving designs able to fulfill mission requirements (i.e. ensure target altitude reaching) despite the presence of uncertainty.

Table 7.1: General mass budget comparison for robust solutions. VLV stands for the current Vega launcher performance.

	m_u kg	$\frac{m_u}{m_i}$ -	$\frac{m_P}{m_i}$ -	$\frac{m_P}{m_P+m_{dry}}$ -
VLV	1430	0.094	0.731	0.840
F_{12}	2102	0.145	0.741	0.905
L_{18}	1977	0.136	0.747	0.903
B_{48}	2001	0.140	0.746	0.905
GPFS	2070	0.143	0.741	0.904
EPFS _{ct}	2322	0.160	0.744	0.926
EPFS _{ad}	2468	0.170	0.743	0.937

The numerical results presented in Chapter 5 showed that the cost of robustness was a payload reduction smaller than 15% with respect to the deterministic optimal design. Robust solutions had larger web thickness and grain length than deterministic one. This optimization strategy aimed at obtaining the surplus of fuel mass, required to withstand the effects of uncertainties during hybrid rocket engine burn, and, at the same time, maintain the increase in engine dry mass as small as possible. In any case, the performance, in terms of delivered payload mass, of the robust solutions employing a gas pressurized feed system resulted better by almost one-third than the actual Vega launcher one.

The hybrid powered upper stage exhibited even better performance considering an electrical pump feed system, as presented in Chapter 6. Optimized solutions were

able to grant robustness in the design and a relevant payload mass gain, between one-tenth and one-fifth depending on the properties taken into account for electrical systems, with respect to the robust optimal solution obtained employing the same uncertainty model and a gas pressurized feed system. Moreover, the robust optimal solution employing electrical feed system outperformed by far actual Vega launcher performance. In this case the payload gain resulted to be of roughly one tonne, which is almost 70% of the total current Vega launcher payload mass.

In the end, the results presented in this Doctoral Thesis proved that hybrid rocket engines are a viable option for upper stages, when a robust-based optimization procedure, able to accurately manage the intrinsic uncertainty in the design, is available. Moreover, innovative solutions, such as electrical turbo pump feed system, resulted able to further increase the appeal of hybrid propulsion system with respect to heritage propulsion architectures granting relevant performance boosts. Future developments of the work here presented should include the use of the developed optimization procedure to different applications, such as small satellite launchers and space engines, and a more refined modeling of electrical systems. Moreover, additional enhancement of the uncertainty characterization and management methods here employed should be researched, aiming at an affordable computational cost even when a large number of uncertain parameters have to be taken into account within the optimization procedure.

Nomenclature

Acronyms

AMROC	AMerican ROcket Company
ANOM	ANalysis Of Means
ANOVA	ANalysis Of VAriance
AVUM	Attitude Vernier Upper Module
BVP	Boundary Value Problem
CFD	Computational Fluid Dynamics
DOE	Design Of Experiments
EAs	Evolutionary Algorithms
EE	Elementary Effects
EPFS	Electric Pump Feed System
EPFSs	Electric Pump Feed Systems
ESA	European Space Agency
FFD	Fractional Factorial Design
FLOX	Fluorine Liquid OXYgen
GE	General Electric company
GIRD	group for the study of reactive motion, Russian: Группа Изучения Реактивного Движения (Группа Изучения Реактивного Движения)
GPFS	Gas Pressurized Feed System
GPFSs	Gas Pressurized Feed Systems
HAST	High Altitude Super-sonic Target
HP	Hydrogen Peroxide
HRE	Hybrid Rocket Engine
HREs	Hybrid Rocket Engines

HTPB	Hydroxyl-Terminated PolyButadiene
LEX	Lithergol EXperimental
LOX	Liquid OXYgen
LRE	Liquid Rocket Engine
LREs	Liquid Rocket Engines
MAV	Mars Ascent Vehicle
NASA	National Aeronautics and Space Administration
NTO	Nitrogen TetrOxide
OAT	Once at A Time
OCT	Optimal Control Theory
PB	PolyButadiene
PDF	Probability Density Function
PE	Poly Ethylene
PMMA	PolyMethylMethacrylate
PSO	Particle Swarm Optimization
RCDB	Randomized Complete Block Design
RDM	Robust Design Method
RFNA	Red Fuming Nitric Acid
RP1	Rocket Propellant-1
SA	Sensitivity Analysis
S/N	Signal to Noise ratio
SRM	Solid Rocket Motor
SRMs	Solid Rocket Motors
SSO	Sun Synchronous Orbit
SS	Sum of Squares
s.t.	Such That
UDMH	Unsymmetrical DiMethylHydrazine
USAF	United States Air Force
VLV	Vega Launch Vehicle
XDF	eXperimental Douglas Fir
Z23	Zephiro 23

Z9 Zephiro 9

Greek Symbols

α	Mixture ratio
Δ	Altitude violation, [m]
Δ_0	Engineering tolerance
δ_{be}	Batteries energy density, [Wh/kg]
δ_{bp}	Batteries power density, [kW/kg]
δ_{ep}	Electric motor and pump power density, [kW/kg]
ΔH_{fw}	Main stream thermal energy per unit mass, [J/kg]
$\Delta H_{v,eff}$	Latent heat of sublimation per unit mass, [J/kg]
ϵ	Multi-objective constraint, [km]
η	Efficiency
η_i	Signal to Noise ratio
η_{ep}	Electric motor and pump efficiency
γ	Specific heat ratio
μ	Mean value
μ_j^*	Mean of the absolute values
ω	Earth's angular velocity, [s ⁻¹]
Φ	Merit function, [kg]
ϕ	Latitude, [deg]
π	Pi, Archimedes' constant
ρ	Density, [kg/m ³]
σ	Standard deviation
σ^2	Variance

Roman Symbols

a	Regression rate correlation coefficient, [m ²ⁿ⁺¹ s ⁿ⁻¹ kg ⁻ⁿ]
A_0	Failure cost
A_b	Burning surface area, [m ²]
A_p	Port area, [m ²]
A_{th}	Nozzle throat area, [m ²]
\mathbf{b}	Design parameters vector

B_{48}	Box-Behnken's array
\mathbf{b}_L	Lower bound vector
\mathbf{b}_U	Upper bound vector
B	ΔH_{fw} to $\Delta H_{v,eff}$ ratio
C	Learning factor
c^*	Characteristic velocity, [m/s]
C_F	Thrust coefficient
\mathbf{D}	Drag vector, [N]
D	Rocket outer diameter, [m]
DET	Deterministic design
E	Nozzle area-ratio
E_e	Electric energy, [Wh]
e_j	Vector of the canonical base
$E_j^{(i)}$	Elementary effect of the j -th input parameter at the i -th repetition
\mathbf{F}	Thrust vector, [N]
F	Generic model output
F_{12}	F_{12} fractional factorial array
\mathbf{g}	Gravity acceleration, [m/s ²]
G	Mass flux, [kg/(m ² s)]
$g_j(\mathbf{b})$	j -th inequality constraint
G_N	Gravitational constant, [Nm ² /kg ²]
h	Altitude, [km]
h^*	Target altitude, [km]
I_{SP}	SPecific Impulse, [s]
J	Initial throat area to port area ratio
k	Number of factors
k_h	Linear combination constant, [kg/km]
K_{ero}	Nozzle throat erosion constant, [m ^{1.2} s ⁻¹ bar ^{-0.8}]
L	Number of levels
$L(y)$	Quality loss function
L_{18}	Taguchi's L_{18} orthogonal array

L_9	L_9 orthogonal array
L_b	Fuel grain length, [m]
L_n	Orthogonal array
\mathbf{M}	Signal factors vector
M	Rocket mass, [kg]
m	Mass, [kg]
M_{\oplus}	Earth mass, [kg]
m_u	Payload mass, [kg]
N	Number of model evaluation
N	Number
n	Regression rate correlation exponent
N_{inp}	Number of input parameters
NOM	Nominal
\mathbf{p}	Uncertain parameters vector
P	Burning perimeter, [m]
P_e	Electric Power, [kW]
P_i	Probability function
\mathbf{p}_p	"A posteriori" uncertain parameters vector
p	Pressure, [bar]
q	Heat flux, [J/(m ² s)]
Q	Average quality loss
\mathbf{r}	Position vector, [m]
r	Number of repetition
RAND	Random number
R_g	Grain outer radius, [m]
R_i	Grain initial inner radius, [m]
R_{th}	Throat radius, [m]
s	Eroded distance, thickness, [m]
T	Temperature, [K]
t	time, [s]
u_r	Velocity component in the radial direction, [km/s]

\mathbf{v}	Velocity vector, [m/s]
V	Volume, [m ³]
v	Particle velocity
v_e	Velocity component in the eastward direction, [km/s]
v_{max}	Particle maximum velocity
w	Web thickness, [m]
v_n	Velocity component in the northward direction, [km/s]
\mathbf{X}	Input parameters vector
\mathbf{x}	Noise factors vector
X	Particle position
x	Axial position, [m]
y	Burning distance, [m]
\mathbf{z}	Control factors vector
Z	Hydraulic resistance, [1/(kg m)]
\mathbf{z}^p	Noise vector of \mathbf{p}

Superscripts

\cdot	Time derivative
*	Characteristic value

Subscripts

0	Ambient
1	Combustion chamber at head-end
%	Percentage
a	Auxiliary gas tank
abl	Ablative layer
ad	Advanced design
Al	Aluminum
avg	Average
b	Batteries
BD	Beginning of blow-down phase
$best$	Best
$burn$	Burn

Nomenclature

<i>c</i>	Combustion chamber at nozzle entrance
<i>c*</i>	Characteristic velocity
<i>case</i>	Engine case
<i>cc</i>	Combustion chamber wall
<i>C_F</i>	Thrust coefficient
<i>ct</i>	Current technology
<i>d</i>	Discharge
<i>dry</i>	Engine dry
<i>e</i>	Nozzle exit
<i>ep</i>	Electric motor and pump
<i>F</i>	Fuel
<i>f</i>	Final
<i>fairing</i>	Fairing
<i>FE</i>	Merit function evaluations
<i>F</i>	Fuel
<i>fs</i>	Feed system
<i>G</i>	Generations
<i>g</i>	Pressurizing gas
<i>I</i>	Individuals
<i>i</i>	Initial
<i>in</i>	Inner
<i>le</i>	Lateral end
<i>lin</i>	Liner
<i>max</i>	Maximum
<i>ME</i>	Model evaluation
<i>min</i>	Minimum
<i>nz</i>	Nozzle
<i>O</i>	Oxidizer
<i>opt</i>	optimal
<i>out</i>	Outer
<i>P</i>	Propellants

<i>p</i>	Grain port
<i>prior</i>	"a priori"
<i>Prt</i>	Particle
<i>ref</i>	Reference
<i>rel</i>	Relative
<i>S</i>	Swarm
<i>SA</i>	Sensitivity Analysis
<i>sl</i>	Propellant sliver
<i>t</i>	Oxidizer tank
<i>tot</i>	Total
<i>u</i>	Payload
<i>ull</i>	Ullage

Other Symbols

⊕	Standard astronomical symbol for planet Earth
±	Factorial design-involved parameters